The Lovisa Stratiform Zn-Pb Deposit, Bergslagen, Sweden: Structure, Stratigraphy, and Ore Genesis

N. F. Jansson,[1,†] S. Sädbom,[2] R. L. Allen,[1,3,*] K. Billström,[4] and P. G. Spry[5]

[1] *Division of Geosciences and Environmental Engineering, Luleå University of Technology, 971 87 Luleå, Sweden*

[2] *Lovisagruvan AB, Håkansboda 1, 711 77 Stråssa, Sweden*

[3] *Boliden Mineral, Exploration Department, 776 98 Garpenberg, Sweden*

[4] *Department of Geosciences, Swedish Museum of Natural History, Box 50 007, 104 05 Stockholm, Sweden*

[5] *Department of Geological and Atmospheric Sciences, Iowa State University, 253 Science I, 2237 Osborn Drive, Ames, Iowa 50011-3212*

Abstract

Medium- to high-grade metamorphosed, 1.9 Ga, stratiform, syngenetic Zn-Pb ± Ag sulfide deposits constitute an economically important type of ore deposit in the Bergslagen lithotectonic unit of the Fennoscandian Shield. The Lovisa Zn-Pb deposit occurs in a metamorphosed succession of rhyolitic ash-siltstone, rhyolitic mass flow deposits, limestone, and Fe formation, deposited at a stage of waning volcanism in Bergslagen.

Accessory graphite, absence of Ce anomalies in shale-normalized rare earth element (REE) data, and absence of hematite in Mn-rich Fe formations stratigraphically below the Lovisa Zn-Pb deposit indicate a suboxic-anoxic depositional environment. The uppermost Mn-rich Fe formation contains disseminated, inferred syngenetic Pb-Ag mineralization with mainly negative $\delta^{34}S$ values in sphalerite and galena (–6.1 to –1.9‰). Deposition of this Fe formation terminated during a pulse of explosive felsic volcanism. The Lovisa Zn-Pb deposit is interpreted to have formed in an alkali-rich brine pool developed immediately after this volcanic event, based on lithogeochemical and stratigraphic evidence. The first stage of mineralization deposited stratiform sphalerite mineralization with mainly positive $\delta^{34}S$ values (–0.9 to 4.7‰). This was succeeded by deposition of more sphalerite-galena stratiform mineralization with $\delta^{34}S$ values close to 0‰ (–2.1 to 1.5‰). The more galena-rich mineralization partitioned strain and was partly remobilized during later ductile deformation.

The stratigraphic context, sulfide mineralogy, S isotopes, and alteration geochemistry suggest that the metalliferous fluids and the depositional environment were H_2S deficient (S poor or SO_4^{2-} dominant). The source of S is interpreted to have been a mixture of H_2S derived from bacterial and thermochemical seawater sulfate reduction and S derived from leaching of volcanic rocks, with the latter becoming more important over time.

Lovisa formed in a setting where basin subsidence was periodically punctuated by the deposition of thick, syneruptive felsic volcaniclastic mass flow deposits. Coeval volcanism was likely important for driving hydrothermal activity and supplying a reservoir of metals and S. However, the high rate of deposition of volcaniclastic sediment in Bergslagen also precluded the establishment of long-lived, deep, and anoxic environments favorable for accumulation of organic matter and H_2S. This stratigraphic pattern is common in Bergslagen and may explain why large stratiform Zn-Pb deposits are uncommon in the region and restricted to the uppermost part of the metavolcanic succession, directly stratigraphically beneath postvolcanic pelitic rocks.

Introduction

The Lovisa mine exploits one of the most important styles of base metal sulfide mineralization in the Bergslagen mining district of southern Sweden, consisting of stratiform Zn-Pb ± Ag sulfides interbedded with fine-grained, metamorphosed, volcaniclastic rocks. With a strike extent of at least 1,100 m and a minimum depth of 425 m (Carlon, 1987), the known tonnage of Lovisa (past production and current reserves) is 1.15 million metric tonnes (Mt) grading 9.4 wt % Zn, 5.3 wt % Pb, and 10 to 20 ppm Ag. No description of the deposit exists in the scientific literature, with only unpublished exploration reports produced prior to the onset of mining (e.g., Carlon, 1987).

Lovisa has features in common with the 65-Mt Zinkgruvan deposit, which is the largest stratiform Zn-Pb-Ag deposit in the Bergslagen district. Similarities include the stratiform

nature of the ore, a high sphalerite + galena to Fe sulfide ratio, the occurrence of stratiform Zn-Pb ore in a fine-grained succession above a thick metalimestone unit, and the local occurrence of stratabound, dolomite-hosted Cu-Co mineralization nearby. Differences include the smaller size, lower Ag content, and the occurrence of the ore in a succession that also hosts stratiform Fe oxide deposits.

Zinkgruvan has variably been classified as a Broken Hill-type deposit (e.g., Beeson, 1990; Walters, 1996), sedimentary-exhalative (SEDEX) deposit (Hellingwerf, 1996), volcanogenic massive sulfide (VMS) deposit (Billström, 1991), and a VMS-SEDEX hybrid (Hedström et al., 1989). Recently, Jansson et al. (2017) argued that the deposit formed upon exhalation of oxidized saline brines at a near-neutral pH into a reduced ($H_2S > SO_4^{2-}$) water column above a thick succession of dominantly felsic volcanic rocks. The inferred fluid chemistry differs from typical VMS models, Selwyn-type SEDEX models, and most fluid models for Broken Hill but has similarities to MacArthur-type SEDEX models (cf. Cooke et al.,

†Corresponding author: e-mail, niljan@ltu.se
*Present address: Volcanic Resources AB, Nås 230, 776 92 Hedemora, Sweden.

2000). A continental back-arc setting with a high proportion of felsic metavolcanic rocks deposited in a shallow marine setting in the footwall and the siting of the deposit at just below the transition from rift-phase to sag-phase sediments are, however, features more similar to Broken Hill (Allen et al., 1996; Walters 1996).

In this study, we address the controls on ore formation at Lovisa based on new data from underground workings and recent exploration drilling, remapping of surface outcrops, whole-rock lithogeochemistry, and mineral chemical and isotope analysis (Pb and S). The focus is on constraining the depositional environment, timing and controls on ore formation, and the postore modifications resulting from the tectonic and metamorphic overprint. Due to the high proportion of stratiform Fe oxide deposits in the succession, their characteristics and possible genetic relationships to the stratiform Zn-Pb mineralization are evaluated.

Regional Geology

The Bergslagen mining district is located in the Bergslagen lithotectonic unit of the Fennoscandian Shield (Stephens and Andersson, 2015). The Bergslagen lithotectonic unit is dominated by plutonic rocks emplaced at various stages during the ca. 1.9 to 1.8 Svecokarelian orogeny (Stephens et al., 2009). These intrusive rocks record variable degrees of tectonic and metamorphic overprint during two phases of

ductile deformation and mainly amphibolite facies metamorphism at ca. 1.87 to 1.85 (D_1 and M_1) and ca. 1.84 to 1.79 Ga (D_2 and M_2; Fig. 1; Stephens and Andersson, 2015; Johansson and Stephens, 2017). The early plutonic rocks intruded a thick succession of supracrustal rocks, deposited at different stages during the evolution of a back-arc basin developed on continental crust (Allen et al., 1996). The supracrustal rocks commonly form inliers bound by plutonic rocks and shear zones (Fig. 1).

The lowermost preserved part of the stratigraphy consists of metasedimentary rocks that record a shallowing upward transition from turbidites to locally cross-bedded quartzite. This is overlain by a thick succession of dominantly felsic metavolcanic rocks that, based on original depositional facies, can be subdivided into a lower succession dominated by pyroclastic flow deposits, coherent lavas, and subvolcanic intrusions and an upper, more stratified succession in which originally silt- to sand-grain-size volcanic ash deposits (ash-siltstone and ash-sandstone of Allen et al., 1996) are interbedded with volcaniclastic mass flow deposits, limestone (now marble), banded iron formations (BIFs), and rare stratiform sulfide mineralization (Allen et al., 1996). Most Fe oxide and base metal sulfide deposits occur in this upper part of the succession, which, in addition to stratiform syngenetic deposits, also hosts base metals sulfide and Fe oxide deposits that replaced limestone (Allen et al., 1996;
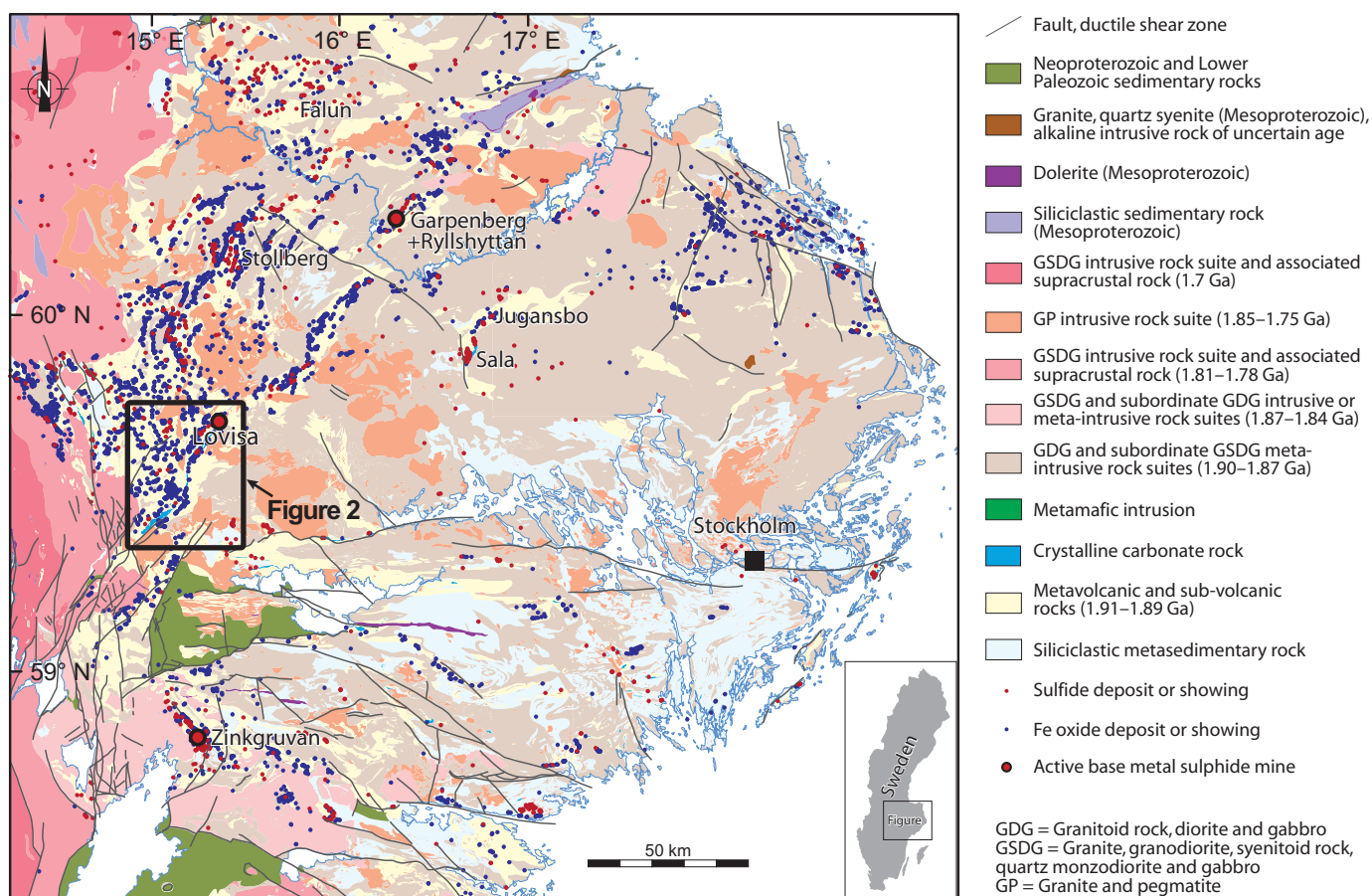

Fig. 1. Geologic map of Bergslagen, modified after Stephens et al. (2009). Inset shows location in Sweden. Box outline shows the location of Figure 2. Inset shows location of map.

Jansson, 2011). The metavolcanic succession is overlain by fine-grained metasedimentary rocks.

The Lovisa deposit is located in the northernmost part of the NE-trending Guldsmedshyttan syncline (Fig. 2). This syncline hosts many mineral deposits over a strike extent of ca. 45 km including BIF, Fe oxide deposits in marble and skarn[1], and base metal sulfide deposits (Geijer and Magnusson, 1944; Carlon and Bleeker, 1988; Hellingwerf et al., 1988).

The syncline was interpreted as an F[1] fold by Lundström (1983), who showed that it is isoclinal and doubly plunging with a steeply E dipping axial surface and an overturned eastern limb. Carlon and Bleeker (1988) demonstrated that the syncline was refolded around W- to NW-trending axial surfaces, resulting in a hook-like fold interference pattern northeast of Lovisa (Fig. 3; Bleeker, 1984; Carlon and Bleeker, 1988). The hinge of the F[1] syncline has been traced southward to the area east of Striberg, whereas farther south the fold is truncated by NE-trending shears and fault zones (Stephens, 1998). Beunk and Kuipers (2012) suggested that the area is transgressed by a large system of approximately NE trending, sinistral shear zones that run parallel to the marble unit along its entire length (Fig. 2) and extends farther northeast toward Garpenberg (Fig. 1). This shear system was termed the "west Bergslagen boundary zone." No detailed pressure-temperature estimates exist for metamorphism in the Guldsmedshyttan syncline, but regional metamorphism was estimated to have reached amphibolite facies based on the presence of sillimanite, garnet, and cordierite (Lundström, 1983; Stephens et al., 2009).

The lowermost part of the stratigraphy on the northwest limb of the regional syncline consists of a package of feldspar- and quartzphyric, massive, felsic metavolcanic rocks overlain by rhyolitic, quartzphyric, medium-grained metavolcanic rocks (Carlon and Bleeker, 1988), termed the Storsjön Formation by Lundström (1983) (Fig. 4). Lundström (1983) and Stephens et al. (2009) interpreted most of these rocks as subvolcanic intrusions. This metavolcanic succession is overlain by the Usken Formation, beginning with a regionally extensive unit of hematite + quartz-rich BIFs from which Fe ore has been mined at many locations including Blanka, Stripa, Stråssa, and Striberg (Fig. 3). Mining mainly occurred in structurally thickened zones, wherein the Fe content has been upgraded by alteration involving conversion of hematite to magnetite and dissolution of quartz (Geijer and Magnusson, 1944). The footwall metavolcanic rocks to the Stråssa deposit contain porphyroblasts of magnetite, biotite, cordierite, and sillimanite (Carlon and Bleeker, 1988).

In the upper part of the stratigraphy, the syncline hosts one of the most laterally extensive marble units in Bergslagen, with a strike extent of ca. 45 km and a thickness of 50 to 250 m (Fig. 2). The marble is mainly dolomitic in the Lovisa area (Fig. 3) but regionally ranges from calcitic to dolomitic (Carlon and Bleeker, 1988). Allen et al. (2003) demonstrated that at least the stratigraphic lower few hundred meters of the marble in the Älvlången area has a stromatolitic origin

---

[1] The term "skarn" in this paper is used in a fashion similar to that used by Törnebohm (1875), i.e., purely descriptive for stratabound and stratiform calc-silicate rocks dominated by garnet, clinoamphibole, and/or clinopyroxene. No spatial or genetic link to igneous intrusions is implied by the term.

(Fig. 2). For clarity, herein we refer to the marble unit as the "Håkansboda limestone."

The succession between the BIF and the Håkansboda limestone is made of massive, aphyric to quartzphyric, rhyolitic metavolcanic rocks (Carlon and Bleeker, 1988). The transition upward to the Håkansboda limestone is gradational, marked by the appearance of rhyolitic ash-siltstone with interbedded calc-silicate rocks of calcic clinopyroxene and garnet-biotite-hornblende with local magnetite and pyrrhotite, followed by the appearance of thin beds of dolomitic and calcitic marble (Carlon and Bleeker, 1988). Such stratiform, bedded calc-silicate rocks ("skarn beds") have elsewhere in Bergslagen been shown to include reaction skarns, formed by regional metamorphism of hybrid rock types containing a variable proportion of interbedded carbonate, variably altered volcaniclastic material, and locally Fe oxides (e.g., Hedström et al., 1989; Jansson and Allen, 2011; Jansson et al., 2013).

The Håkansboda limestone is massive in the lower part but grades upward (Fig. 3) into a succession dominated by rhyolitic ash-siltstone with lesser interbeds of marble, calc-silicate rock (clinopyroxene-amphibole), magnetite-bearing Fe formation, and coarse-grained volcaniclastic rock (Lundström, 1983; Carlon and Bleeker, 1988). The Lovisa Zn-Pb deposit is situated in this part of the stratigraphy in an area hosting several magnetite Fe formations that contain minor galena and Ag minerals. A similar type of Pb-Ag deposit was mined at Guldsmedshyttan, southwest of Lovisa (Fig. 3; Tegengren, 1924).

The Usken Formation is overlain by the Mårdshyttan Formation, which consists of metamorphosed, originally mainly fine grained, sedimentary rocks that are correlated regionally in Bergslagen with the postvolcanic metasedimentary rocks that overlie the volcanic succession. Due to the depth of erosion, these rocks are not present in the Lovisa area but occur in a basinal culmination of the Guldsmedshyttan syncline south of Lovisa (Fig. 2).

Detailed correlation between individual beds of marble, bedded calc-silicate rock, and Fe formation of the Usken Formation across fold hinges and faults in the Lovisa area has not been successful to date, and various models for the local structure were proposed during mineral exploration in the area (Fig 3; Bleeker, 1984; Engvall and Persson, 1985; Carlon, 1987). A revised model for the structure and stratigraphic correlations is presented in this paper.

Methods

Only assay data and geologic logs remain from earlier exploration campaigns in the Lovisa area. This, along with scarcity of outcrops south of the mine, hindered evaluation of the southern part of the deposit. Our study is focused on underground workings in the currently mined northern part of the deposit. Underground mapping of three mine levels, surface mapping, and logging of new exploration drill holes formed the basis for producing new geologic maps, geologic cross sections, and a 3-D model of the deposit generated in the Leapfrog Geo computer software. Legacy reports provide a detailed lithological subdivision based on core logging of premining exploration drill holes, the most detailed account being a synthesis provided by Carlon (1987).

Whole-rock lithogeochemistry samples were collected from the underground workings, drill core, and surface outcrops.
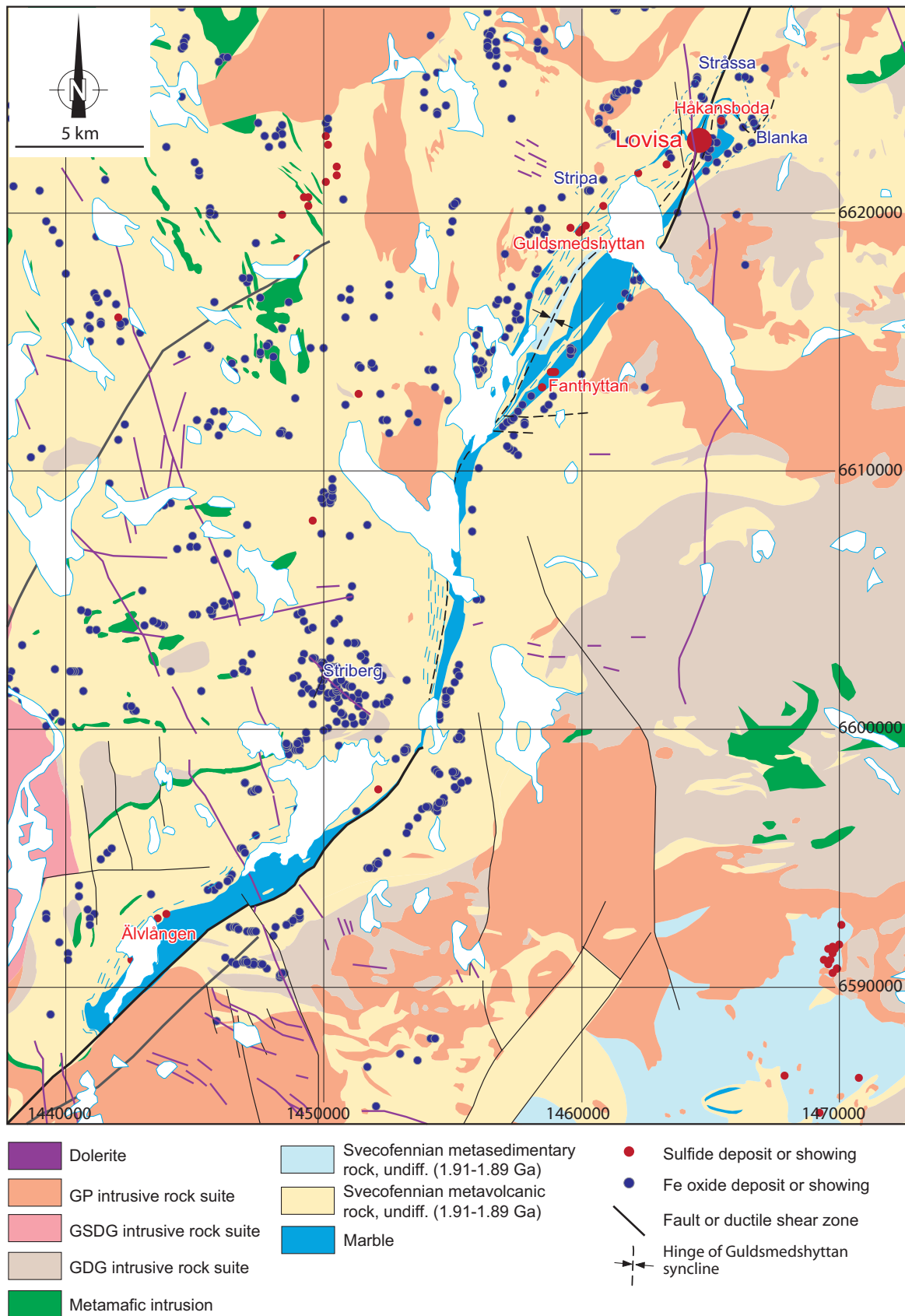
Fig. 2. Geologic map of the Guldsmedshyttan syncline (box outline in Fig. 1). Modified after Stephens et al., 2009. Grid is Swedish national grid RT90. Abbreviations as in Figure 1.

Fig. 3. Geologic map of the northernmost part of the Guldsmedshyttan syncline, based on data from the current investigation and legacy data from Bleeker (1984), Carlon (1987), and Carlon and Bleeker (1988). Grid is Swedish national grid RT90. Note that all supracrustal rocks are metamorphosed but are here named according to the interpreted premetamorphic precursor. Abbreviations as in Figure 1. FW = footwall, HW = hanging wall.

Fig. 4. Stratigraphic column of the northern Guldsmedshyttan area, showing the position of the Lovisa Zn-Pb deposit in relation to stratigraphic units defined by Lundström (1983). The stratigraphy in the Usken Formation is revised according to results from the current study, whereas the Storsjön and Mårdshyttan Formations are drawn schematically based on Lundström (1983) and Carlon and Bleeker (1988). The color legend is consistent with Figures 3, 5, and 6. Abbreviations: Fsp = feldspar, Hem = hematite, Mag = magnetite, Qz = quartz.

Drill holes 1501, 1502, and 1507 were systematically sampled at 5- to 10-m intervals. Cleaned samples lacking veins or weathered surfaces were sent to ALS Chemex in Öjebyn, Sweden, for sample preparation. The pulps were sent to Acme Laboratories, Vancouver, Canada, for analysis using their LF202 routine. Major oxides and Ba were determined by inductively coupled plasma-emission spectroscopy (ICP-ES) and refractory trace elements by ICP-mass spectrometry (ICP-MS), both following lithium borate fusion and nitric acid digestion. Zinc and Pb contents >1 wt % were determined by single element ICP-ES following aqua regia digestion. Total S and carbon were determined by the Leco method. Boron was determined by ICP-ES following NaOH fusion at ALS Vancouver, Canada. Analytical quality was monitored with certified reference materials disguised as unknowns. Returned values for all elements differed by less than 5% from the corresponding certified reference values.

Continuous sections through the ore-bearing interval were sampled by Lovisagruvan AB, Stråssa, Sweden, and analyzed for major and trace elements by MS Analytical, Langley, Canada. Sample pulps were fused by borate flux in a high-temperature controlled muffle furnace, and the resulting beads were dissolved in 4% nitric acid. Major oxides were determined by ICP-ES, and refractory trace elements (Ba, La, Lu, Cr, Cs, Ga, Hf, Nb, Rb, Sn, Sr, Ta, Th, U, V, W, Y, and Zr) were determined by ICP-MS. Other trace elements were determined by ICP-ES following aqua regia digestion. Total S and carbon were determined by a Leco carbon and S analyzer. Sulfide-rich samples were quantified by ICP-ES following aqua regia (Ag) or four-acid digestion (Pb, Zn). Where Zn and Pb contents exceeded the upper detection limits of the acid digestions (>10 wt %), these elements were quantified using wet titration techniques. Analytical quality was monitored with method blanks, duplicates, and certified and/or verified in-house reference materials. The uncertainties for the different methods (in % of the reported values) are (1) 5% for titration, (2) ±7.5% for borate fusion and sulfide-rich four-acid, (3) ±10% for total C and S, and (4) ±15% for aqua regia.

Electronic microprobe analyses on polished thin sections were performed using a Jeol JXA-8530F HyperProbe electron probe microanalyser at Uppsala University, Sweden. Standard operating used conditions were 15-kV accelerating voltage and 15-nA beam current. International reference materials were used for calibration and standardization. Analytical precision based on measurements on Smithsonian Institute mineral standards have shown that uncertainties are ≤1.5% standard devisation (s.d.) for oxides at concentrations of >10 wt %, ≤2.2% s.d. for oxides at concentrations of 5 to 10 wt %, and ≤10% s.d. for oxides at lower concentrations (Barker et al., 2015).

The S isotope composition of handpicked mineral separates was determined at the University of Salamanca, Spain, using a conventional method described by Robinson and Kusakabe (1975). Calibration to the Cañon Diablo Troilite (CDT) standard was performed by analysis of a suite of international reference materials (IAEA-S-1, IAEA-S-4, NBS-123, and NBS-127) and internal laboratory standards in conjunction with analysis of the unknowns. The $\delta^{34}S$ values are reported relative to the CDT standard.

Chemical preparation for the Pb isotope analyses involved dissolution of handpicked galena, followed by electrodeposition of lead on a Pt electrode. A Nu Plasma II multicollector ICP-MS instrument in the Vegacenter facility at the Natural History Museum in Stockholm, Sweden, was used to measure the isotopic ratios. For these analyses, Pb was stripped off from the Pt electrode and then diluted in 0.5 N HNO_3 to an estimated concentration of 30 to 50 ppb Pb, with Tl added to allow for an internal correction of mass bias. Measured intensities were corrected for background and Hg interference on mass 204, and the Pb isotope ratios of the unknowns were normalized to $^{203}Tl/^{205}Tl = 0.418918$. The obtained numbers for the standard are within error of those given by Todt et al. (1993), and the external reproducibility is estimated to be between 0.04 ($^{206}Pb/^{204}Pb$) and 0.08% ($^{208}Pb/^{204}Pb$).

Local Geology

Structural geology

The Lovisa mine is located on the eastern limb of a moderately SSW plunging anticline, here termed the "Lovisa anticline" (Figs. 3, 5). The anticline is part of a parasitic fold with Z symmetry on the western limb of the Guldsmedshyttan syncline (Fig. 3) and is correlated with the first-generation folds (F_1) of Carlon and Bleeker (1988). F_1 is associated with the most conspicuous NNE-trending tectonic fabric in the mine, making up a steeply E dipping spaced foliation, which is commonly accentuated by later spaced fractures. Mesoscale F_1 fold hinges in the mine generally plunge ca. 30° to 40° toward the south-southwest.

Cross folding related to the subsequent F_2 phase of folding is subordinate in the mine but is locally evidenced by NNW- to W-striking disharmonic folds with a poorly developed foliation and undulating fold axes that refold the more NNE-trending fabrics. A strong stretching lineation plunging ca. 60° toward the south is defined by stretched quartz phenocrysts and fragments in metavolcanic rocks and may correlate with the regional L_2 lineation (cf. Stephens et al., 2009).

Several steeply SE to ESE dipping shear zones with associated chlorite-coated fractures caused stacking of the stratigraphy, including the massive sulfide ore bodies. The most important in the mine is here termed the "central shear" (Figs. 5, 6). Mineralization displays attenuation, local folding as well as local brecciation, and gouge proximal to these zones. Hinges of folds in ore plunge ca. 30° south-southwest and indicate reverse displacement with a dextral component, despite locally yielding apparent sinistral offsets on plan view (e.g., Fig. 5).

These shear zones and associated folds are subparallel to the axial surface and hinge of the Lovisa antiform, although they display local crosscutting relationships with F_1 and F_2 structures. The shear zones offset rare, thin, gently dipping

pegmatite veins that record no ductile deformation except where adjacent to the shear zones.

The structures described above are crosscut by several subvertical brittle faults trending northwest to north-northeast. These commonly have negligible, mainly dextral displacements seldom exceeding 1 m (Fig. 5). However, a prominent NNW-trending fault, termed the "Lovisa fault," forms a southwest limit to the mine at present, although an offset portion of the ore has been found south of it (Carlon, 1987; Fig. 5). This fault corresponds with an apparent dextral displacement on plan view, although the true displacement vector is unknown.

A prominent NNE-trending fault east of Lovisa was inferred during exploration drilling (Engvall and Persson, 1985) and verified during recent exploration drilling from the mine (Figs. 3, 6). The fault contains both younger clay gouge and older mylonite. In drill hole 1507, the fault is intruded by a dolerite dike with wide chilled margins. Based on its orientation, the dike can be correlated with the Sveconorwegian dolerite dike suite, which was emplaced at around 0.98 to 0.95 Ga (cf. Söderlund et al., 2005). The dike was unaffected by mylonitization but was altered to clay gouge on the eastern contact. Displacement along the fault is at least 500 m based on stratigraphic correlation of the Håkansboda limestone and an overlying magnetite occurrence (Fig. 6).

Stratigraphy

The current study focuses on the stratigraphic interval between the upper part of the Håkansboda limestone and the Mårdshyttan Formation (Figs. 4, 6). All rocks in the area, excluding dolerite dikes and pegmatites, were subjected to regional metamorphism. Descriptive premetamorphic rock names are used for brevity and to emphasize stratigraphic features, except for calc-silicate rocks (skarns) and strongly altered rocks where precursors are uncertain. These are named according to their current metamorphic mineralogy. Whole-rock lithogeochemical data for the volcaniclastic units are provided in Table 1, and data on representative samples of Fe formations are provided in Table 2.

Stratigraphic footwall: Ductile deformation and lack of drill holes intersecting the lower contact of the Håkansboda limestone prevent determination of true stratigraphic thickness for this unit, although it is estimated to be at least 200 m thick. The marble is dolomitic, most commonly massive, and hosts centimeter-sized, dark-green crystals of dark-green calcic clinoamphibole (Fig. 7A). Subordinate interbeds of rhyolitic ash-siltstone occur locally. Biotite-tremolite schists commonly formed at the dolomite-siltstone interfaces and, where the interbeds are thin, completely replaced them.

The stratigraphic upper 20 m of the Håkansboda limestone consists of a zone of interbedded pink-red rhyolitic siltstone, calcitic limestone, and bedded calc-silicate rock (epidote-actinolite ± quartz). These rocks grade upward into an interval of massive magnetite with a gangue of dolomite, calcite, actinolite, serpentine, and chlorite (Fig. 6). Minor pyrite, pyrrhotite, and chalcopyrite are locally present and are completely mantled by magnetite. Actinolite crystals of variable molar Mg/Mg + Fe (0.76–0.88) form complex intergrowths with serpentine, commonly occurring as rounded aggregates rimmed by magnetite in a carbonate matrix. These intergrowths most likely reflect retrograde alteration products after former
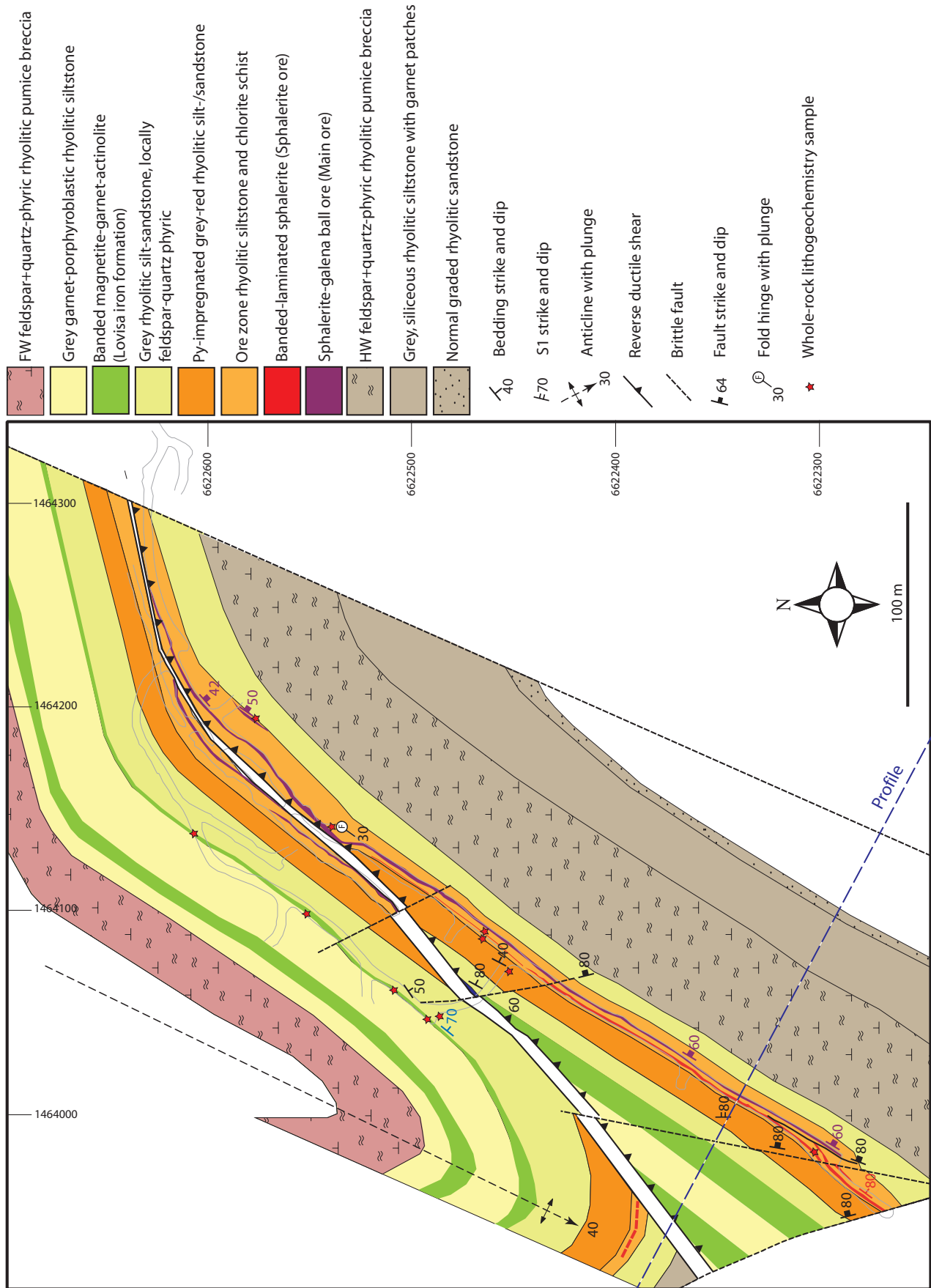
Fig. 5. Geologic map of the 135- to 145-m level of Lovisa mine, based on underground mapping (including projection from adjacent levels) and data from legacy drill cores. Grid is Swedish national grid RT90. White area is unknown. Abbreviations: FW = footwall, HW = hanging wall, Py = pyrite.

Legend:
- FW feldspar+quartz-phyric rhyolitic pumice breccia
- Grey garnet-porphyroblastic rhyolitic siltstone
- Banded magnetite-garnet-actinolite (Lovisa iron formation)
- Grey rhyolitic silt-sandstone, locally feldspar-quartz phyric
- Py-impregnated grey-red rhyolitic silt-/sandstone
- Ore zone rhyolitic siltstone and chlorite schist
- Banded-laminated sphalerite (Sphalerite ore)
- Sphalerite-galena ball ore (Main ore)
- HW feldspar+quartz-phyric rhyolitic pumice breccia
- Grey, siliceous rhyolitic siltstone with garnet patches
- Normal graded rhyolitic sandstone
- Bedding strike and dip
- S1 strike and dip
- Anticline with plunge
- Reverse ductile shear
- Brittle fault
- Fault strike and dip
- Fold hinge with plunge
- Whole-rock lithogeochemistry sample

Fig. 6. Geologic cross section of the Lovisa deposit based on drill core logging and geologic mapping. Corner coordinates for georeferencing are in Swedish national grid RT90. Abbreviations: FW = footwall, HW = hanging wall.

olivine porphyroblasts (Fig. 8A). This Mg-rich magnetite Fe formation can be correlated with the magnetite occurrence previously mined at the Lekeberg mine north of Lovisa (Fig. 3) and is herein referred to as the Lekeberg Fe formation. It can also be correlated with magnetite Fe formation directly stratigraphically above the Håkansboda limestone east of the Engvall fault (Fig. 6).

The Lekeberg Fe formation is overlain by a 20- to 50-m succession of gray, weakly stratified rhyolitic siltstone and finely feldspar + quartzphyric sandstone with subordinate bedded calc-silicate interbeds of calcic clinoamphibole ± magnetite with euhedral-subhedral garnet porphyroblasts. The feldspar + quartzphyric texture is locally concealed by millimeter-sized metamorphic porphyroblasts of pale-pink garnet and sillimanite needles (Fig. 7B).

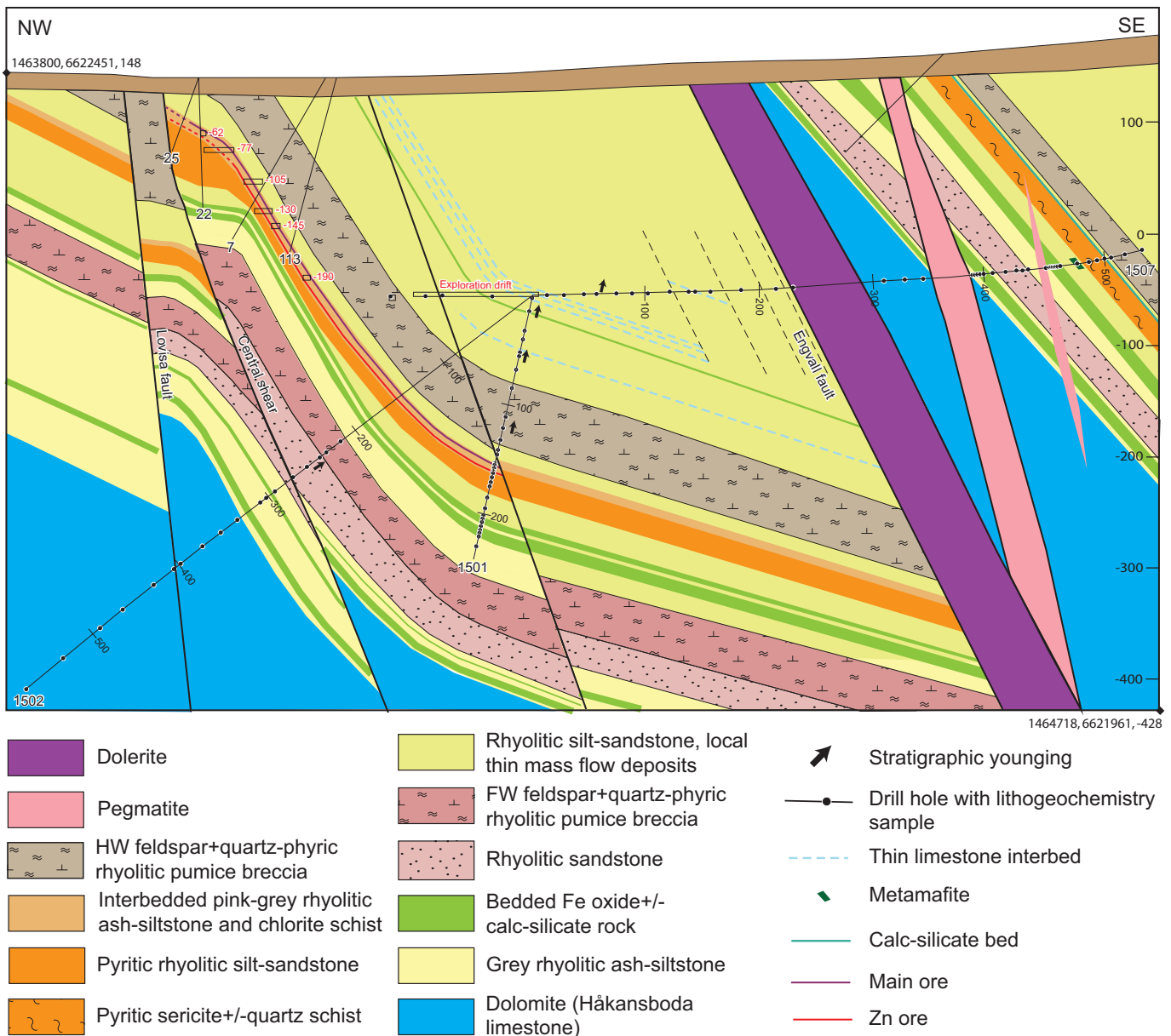The lower gray rhyolitic ash-siltstone is overlain by a 50- to 70-m-thick unit of coarse-grained volcaniclastic rock. The lower half of the unit is a massive, weakly feldspar + quartz-phyric sandstone, whereas the upper half contains abundant phyllosilicate-altered former pumice clasts (Fig. 7C). These clasts contain 5 to 10 vol % 1-mm feldspar phenocrysts and 1 to 4 vol % 1- to 3-mm quartz phenocrysts, whereas the matrix contains fewer crystals. The larger pumice clasts are aligned along a foliation that is subparallel to bedding and overprinted by S_1 (Fig. 8C). Locally, the unit is considerably more crystal rich, containing 20 to 25 vol % 2-mm white feldspar and 5 to 10 vol % 1- to 2-mm blue-gray quartz crystals in a gray fibrous groundmass with tiny pumice fragments and ca. 10 vol % biotite. Few stratigraphic younging indicators have been observed except in drill hole 1502, where thin normal

Table 1. Median,[1] Mean Absolute Deviation (MAD), and Compositional Range for Different Volcaniclastic Units at Lovisagruvan, Arranged Stratigraphically

	Unit N Setting	Method	Rhyolitic ash-siltstone 24 Hanging wall				Rhyolitic pumice breccia 7 Hanging wall				Rhyolitic ash-siltstone 7 Lower hanging wall			
			Median	MAD	Minimum	Maximum	Median	MAD	Minimum	Maximum	Median	MAD	Minimum	Maximum
SiO_2	%	ICP-ES	74.45	3.58	64.33	83.57	75.55	2.15	61.69	78.38	58.42	4.88	53.54	77.99
TiO_2	%	ICP-ES	0.11	0.03	0.07	0.19	0.13	0.03	0.08	0.21	0.30	0.09	0.19	0.79
Al_2O_3	%	ICP-ES	12.08	1.64	8.51	17.33	12.12	1.13	8.76	19.31	18.54	1.04	10.62	19.58
Fe_2O_3 total	%	ICP-ES	1.95	0.67	0.48	4.13	1.91	0.43	0.92	3.52	5.95	1.67	2.02	7.62
MnO	%	ICP-ES	0.06	0.02	0.03	0.67	0.07	0.02	0.03	0.12	0.14	0.08	0.05	0.29
MgO	%	ICP-ES	0.69	0.24	0.08	2.26	1.03	0.10	0.43	2.15	2.74	1.50	0.89	4.56
CaO	%	ICP-ES	0.94	0.40	0.29	3.25	0.72	0.15	0.29	2.43	0.40	0.08	0.25	1.50
Na_2O	%	ICP-ES	2.65	0.58	0.80	4.55	3.35	0.70	0.80	9.78	5.47	1.66	3.62	8.45
K_2O	%	ICP-ES	4.39	1.28	0.82	9.95	3.98	1.21	0.05	5.71	2.06	1.35	0.03	4.17
P_2O_5	%	ICP-ES	0.01	<0.01	<0.01	0.02	0.02	<0.01	0.01	0.03	0.02	0.01	0.01	0.18
Total C	%	Leco	0.07	0.04	<0.02	0.56	0.04	0.03	<0.02	0.47	0.03	<0.02	<0.02	0.22
S	%	Leco	<0.02	<0.02	<0.02	0.04	<0.02	<0.02	<0.02	<0.02	<0.02	<0.02	<0.02	0.08
LOI	%	ICP-ES	1.3	0.4	0.5	2.7	1.0	0.1	0.7	2.4	2.3	0.7	1.2	3.7
Total	%	ICP-ES	99.89	0.02	99.82	99.93	99.89	0.01	99.81	99.93	99.73	0.04	99.29	99.77
Zr	ppm	ICP-MS	156.6	40.8	91.4	339.6	138.5	22.3	91.4	231.1	316.8	78.4	238.4	561.9
Y	ppm	ICP-MS	32.4	6.2	22.7	66.6	31.8	5.8	24.1	58.2	50.8	8.9	41.9	133.2
Nb	ppm	ICP-MS	11.3	2.0	6.1	24.7	10.3	0.8	8.2	15.8	18.3	2.8	15.5	30.4
Co	ppm	ICP-MS	0.8	0.3	0.1	1.7	1.0	0.2	0.7	1.6	1.8	0.9	0.6	3.5
Cr_2O_3	%	ICP-ES	<0.002	<0.002	<0.002	0.006	0.002	<0.002	<0.002	0.004	<0.002	<0.002	<0.002	0.003
Ni	ppm	ICP-MS	0.5	0.1	<0.1	2.4	0.6	0.1	0.4	1.8	1.0	0.5	0.5	2.9
Ba	ppm	ICP-ES	532	110	329	735	444	122	16	566	327	47	14	374
Rb	ppm	ICP-MS	132.9	37.2	53.0	247.4	100.2	15.7	0.8	135.7	49.3	27.7	0.5	87.8
Sr	ppm	ICP-MS	18.1	6.9	7.9	42.1	10.1	2.0	4.4	14.3	8.6	2.3	5.6	13.6
Cu	ppm	ICP-MS	1.9	0.8	0.5	48.0	3.1	1.1	1.9	12.8	2.4	0.8	1.3	13.1
Pb	ppm	ICP-MS	4.2	1.7	2.2	121.1	4.7	2.1	2.6	63.3	126.4	118.7	7.7	3,906.4
Zn	ppm	ICP-MS	32	7	4	68	27	6	21	1214	748	380	195	1,128
As	ppm	ICP-MS	0.5	<0.5	<0.5	1.6	0.9	<0.5	<0.5	2.4	<0.5	<0.5	<0.5	0.7
Ag	ppm	ICP-MS	<0.1	<0.1	<0.1	0.5	0.1	<0.1	<0.1	0.5	0.2	0.2	<0.1	0.5
Au	ppb	ICP-MS	<0.5	<0.5	<0.5	2.2	<0.5	<0.5	<0.5	3.9	<0.5	<0.5	<0.5	0.7
B[2]	ppm	NaOH fusion + ICP finish	<10	<10	<10	120	<10	<10	<10	20	<10	<10	<10	<10
Be	ppm	ICP-MS	2	2	<1	10	2	2	<1	5	4	3	<1	9
Bi	ppm	ICP-MS	0.1	<0.1	<0.1	0.9	0.1	<0.1	<0.1	0.5	<0.1	<0.1	<0.1	0.5
Cd	ppm	ICP-MS	<0.1	<0.1	<0.1	0.1	<0.1	<0.1	<0.1	0.4	0.6	0.6	<0.1	4.7
Cs	ppm	ICP-MS	1.3	0.7	0.2	6.7	0.5	0.5	<0.1	1.5	0.2	0.2	<0.1	0.5
Ga	ppm	ICP-MS	13.6	6.0	6.0	29.5	12.3	2.0	6.8	21.3	22.2	6.5	11.0	30.7
Hf	ppm	ICP-MS	4.9	1.0	3.2	10.5	5.0	0.5	3.2	6.8	9.2	1.7	7.5	16.0
Hg	ppm	ICP-MS	<0.01	<0.01	<0.01	<0.01	<0.01	<0.01	<0.01	<0.01	<0.01	<0.01	<0.01	0.020
Mo	ppm	ICP-MS	1.1	0.4	0.4	8.4	1.2	0.5	0.4	2.7	0.5	0.1	0.2	3.9
Sb	ppm	ICP-MS	0.1	<0.1	<0.1	0.4	<0.1	<0.1	<0.1	0.2	0.2	0.1	<0.1	1.1
Sc	ppm	ICP-MS	5	1	2	10	4	1	3	8	8	3	5	17
Se	ppm	ICP-MS	<0.5	<0.5	<0.5	<0.5	<0.5	<0.5	<0.5	<0.5	<0.5	<0.5	<0.5	<0.5
Sn	ppm	ICP-MS	2	2	<1	6	2	1	<1	4	4	2	1	8
Ta	ppm	ICP-MS	0.9	0.2	0.5	1.9	0.8	0.1	0.6	1.1	1.4	0.3	1.1	2.3
Tl	ppm	ICP-MS	<0.1	<0.1	<0.1	0.2	<0.1	<0.1	<0.1	0.1	<0.1	<0.1	<0.1	<0.1
Th	ppm	ICP-MS	14.5	3.6	8.8	21.2	14.2	0.9	11.0	19.8	19.4	5.0	14.4	26.3
U	ppm	ICP-MS	5.6	1.3	2.7	8.3	5.0	0.7	3.2	7.2	7.8	1.9	5.4	13.1
V	ppm	ICP-MS	<8	<8	<8	<8	<8	<8	<8	<8	<8	<8	<8	17
W	ppm	ICP-MS	0.9	<0.5	<0.5	2.8	1.0	<0.5	<0.5	1.4	0.9	0.1	0.6	2.3
La	ppm	ICP-MS	41.6	6.0	27.0	70.2	39.0	5.0	18.2	56.6	59.6	20.0	19.0	121.7
Ce	ppm	ICP-MS	80.9	9.9	50.7	150.0	74.9	7.5	43.0	114.7	117.1	43.8	37.0	260.1
Pr	ppm	ICP-MS	9.21	1.42	5.77	17.22	8.20	0.83	4.66	12.98	13.64	4.91	4.83	30.10
Nd	ppm	ICP-MS	34.5	6.0	19.8	66.2	31.7	5.0	15.9	49.9	52.5	19.3	19.2	124.9
Sm	ppm	ICP-MS	6.28	0.73	4.28	13.14	5.81	0.23	4.14	9.54	9.77	3.47	4.79	24.06
Eu	ppm	ICP-MS	0.82	0.19	0.41	1.95	0.63	0.22	0.41	1.44	1.95	0.81	0.54	3.21
Gd	ppm	ICP-MS	5.80	0.89	4.08	12.88	5.33	0.32	4.08	10.07	9.57	3.72	5.85	24.07
Tb	ppm	ICP-MS	0.89	0.13	0.69	2.01	0.85	0.09	0.67	1.61	1.57	0.47	1.10	3.70
Dy	ppm	ICP-MS	5.44	0.91	4.17	12.70	5.14	0.77	4.17	10.40	9.94	2.93	7.01	22.76
Ho	ppm	ICP-MS	1.17	0.19	0.81	2.58	1.13	0.15	0.91	2.15	1.90	0.32	1.58	4.64
Er	ppm	ICP-MS	3.69	0.59	2.52	7.90	3.46	0.64	2.81	6.72	5.58	0.85	4.73	14.08
Tm	ppm	ICP-MS	0.57	0.11	0.36	1.32	0.51	0.07	0.41	1.05	0.85	0.13	0.72	2.04
Yb	ppm	ICP-MS	3.83	0.91	2.23	9.10	3.62	0.49	2.67	6.99	5.96	1.40	4.56	13.22
Lu	ppm	ICP-MS	0.60	0.12	0.36	1.40	0.55	0.06	0.44	1.03	0.87	0.16	0.71	1.99

Table 1. *(Cont.)*

	Unit N Setting		Rhyolitic ash-siltstone[2] 5 Ore zone				Pyritic rhyolitic ash-siltstone 6 Upper footwall				Massive rhyolitic silt-sandstone 8 Upper footwall			
		Method	Median	MAD	Minimum	Maximum	Median	MAD	Minimum	Maximum	Median	MAD	Minimum	Maximum
SiO_2	%	ICP-ES	71.08	5.34	58.63	76.47	76.91	6.61	59.56	87.22	74.92	3.40	69.19	82.49
TiO_2	%	ICP-ES	0.18	0.06	0.11	0.35	0.13	0.03	0.06	0.21	0.12	0.01	0.09	0.18
Al_2O_3	%	ICP-ES	11.91	1.03	10.04	18.43	11.62	2.80	6.65	19.47	11.56	1.17	9.27	16.85
Fe_2O_3 total	%	ICP-ES	4.19	1.46	1.04	5.67	2.87	0.95	0.59	4.67	2.62	1.51	1.03	5.64
MnO	%	ICP-ES	0.26	0.12	0.03	0.46	0.07	0.05	0.01	0.19	0.05	0.02	0.02	0.21
MgO	%	ICP-ES	1.98	1.09	0.51	3.49	0.78	0.56	0.18	2.88	0.89	0.24	0.29	1.21
CaO	%	ICP-ES	1.11	0.50	0.27	2.60	0.36	0.14	0.03	1.17	0.32	0.08	0.08	0.42
Na_2O	%	ICP-ES	1.88	0.50	1.08	6.99	4.64	2.50	0.36	10.17	3.77	0.79	0.54	4.83
K_2O	%	ICP-ES	4.02	1.45	2.04	7.11	1.57	0.93	0.05	3.80	2.60	1.10	1.21	3.90
P_2O_5	%	ICP-ES	0.04	0.01	0.03	0.06	<0.01	<0.01	<0.01	<0.01	<0.01	<0.01	<0.01	0.01
Total C	%	Leco	0.16	0.07	0.06	0.42	0.04	<0.02	<0.02	0.19	0.03	<0.02	<0.02	0.06
S	%	Leco	0.16	0.11	<0.02	0.71	0.08	0.03	<0.02	0.39	<0.02	<0.02	<0.02	1.81
LOI	%	ICP-ES	1.9	0.9	0.5	3.0	1.0	0.3	0.6	2.8	1.7	0.4	0.7	3.0
Total	%	ICP-ES	99.37	0.13	97.70	99.52	99.80	0.03	99.62	99.85	99.74	0.05	94.26	99.85
Zr	ppm	ICP-MS	152.9	43.9	97.2	269.7	210.7	51.7	107.8	354.4	213.3	21.9	163.1	292.6
Y	ppm	ICP-MS	36.1	11.9	21.2	60.2	52.3	14.7	31.8	82.0	50.3	7.8	31.7	61.4
Nb	ppm	ICP-MS	14.5	2.1	11.7	19.8	21.9	5.7	12.5	35.8	22.6	2.9	16.8	29.7
Co	ppm	ICP-MS	1.8	1.1	0.2	3.5	0.7	0.4	0.3	2.4	0.7	0.4	0.3	3.1
Cr_2O_3	%	ICP-ES	0.003	0.001	0.002	0.003	<0.002	<0.002	<0.002	0.005	<0.002	<0.002	<0.002	0.006
Ni	ppm	ICP-MS	2.8	1.6	0.9	6.0	0.6	0.3	0.3	1.4	0.7	0.3	0.2	1.3
Ba	ppm	ICP-ES	633	86	221	725	1,046	654	39	2,449	1,328	407	633	46,829
Rb	ppm	ICP-MS	95.9	23.5	46.6	132.5	50.7	26.6	0.1	103.2	74.4	37.0	28.9	138.4
Sr	ppm	ICP-MS	13.8	2.6	9.5	34.1	11.4	2.6	6.5	16.4	10.6	2.3	4.1	69.8
Cu	ppm	ICP-MS	9.9	4.3	2.0	20.7	7.1	5.8	0.7	29.1	14.2	6.4	0.7	208.6
Pb	ppm	ICP-MS	665.4	302.1	143.4	6,355.3	77.6	64.5	3.3	278.5	39.2	31.5	2.8	2,692.8
Zn	ppm	ICP-MS	3,855	1,28	1,975	11,500	134	78	24	305	175	130	21	916
As	ppm	ICP-MS	1.3	0.6	0.6	10.0	1.0	0.5	0.3	4.1	0.5	0.2	0.3	18.1
Ag	ppm	ICP-MS	0.7	0.2	0.3	1.6	<0.1	<0.1	<0.1	0.2	<0.1	<0.1	<0.1	5.1
Au	ppb	ICP-MS	<0.5	<0.5	<0.5	0.8	<0.5	<0.5	<0.5	<0.5	<0.5	<0.5	<0.5	1.4
B[2]	ppm	NaOH fusion + ICP finish	<10	<10	<10	<10	<10	<10	<10	<10	15	<10	<10	50
Be	ppm	ICP-MS	2	1	<1	5	4	2	<1	7	4	1	<1	7
Bi	ppm	ICP-MS	0.6	0.4	0.1	1.3	<0.1	<0.1	<0.1	0.3	<0.1	<0.1	<0.1	1.3
Cd	ppm	ICP-MS	14.2	8.8	0.8	74.6	0.3	0.2	<0.1	1.6	0.6	0.5	<0.1	7.2
Cs	ppm	ICP-MS	0.6	0.3	0.2	1.1	0.5	0.3	<0.1	0.8	0.8	0.4	0.3	5.7
Ga	ppm	ICP-MS	14.3	3.1	11.2	19.2	16.0	6.0	7.0	23.9	15.5	2.0	9.0	28.9
Hf	ppm	ICP-MS	5.1	1.2	3.6	8.2	7.1	1.6	3.3	11.3	7.1	0.9	5.4	9.4
Hg	ppm	ICP-MS	0.045	0.025	0.010	0.110	<0.01	<0.01	<0.01	<0.01	<0.01	<0.01	<0.01	0.030
Mo	ppm	ICP-MS	1.9	0.7	1.0	3.4	0.7	0.3	0.2	1.2	1.3	0.9	<0.1	7.0
Sb	ppm	ICP-MS	0.4	0.1	0.3	1.2	0.2	<0.1	<0.1	0.3	0.2	<0.1	<0.1	0.6
Sc	ppm	ICP-MS	5	2	3	15	4	1	2	5	3	0	3	5
Se	ppm	ICP-MS	<0.5	<0.5	<0.5	<0.5	<0.5	<0.5	<0.5	<0.5	<0.5	<0.5	<0.5	<0.5
Sn	ppm	ICP-MS	3	1	2	3	3	1	2	6	4	1	2	9
Ta	ppm	ICP-MS	1.3	0.1	1.1	1.5	1.7	0.4	0.9	2.4	1.7	0.3	1.2	2.1
Tl	ppm	ICP-MS	<0.1	<0.1	<0.1	0.1	<0.1	<0.1	<0.1	<0.1	<0.1	<0.1	<0.1	<0.1
Th	ppm	ICP-MS	18.3	1.5	16.8	23.8	19.4	4.2	10.8	30.9	19.1	2.3	15.1	27.1
U	ppm	ICP-MS	6.0	1.1	3.9	7.7	8.0	2.2	4.7	13.7	7.2	1.2	5.4	11.7
V	ppm	ICP-MS	10	<8	<8	16	<8	<8	<8	11	<8	<8	<8	11
W	ppm	ICP-MS	1.1	0.1	0.9	1.3	1.3	<0.5	<0.5	2.1	2.1	0.7	0.5	3.2
La	ppm	ICP-MS	46.8	2.8	41.7	82.0	56.3	6.7	43.0	121.7	55.0	13.9	31.4	75.6
Ce	ppm	ICP-MS	94.2	6.8	83.2	156.4	116.6	6.3	91.6	235.5	114.6	24.7	49.1	147.8
Pr	ppm	ICP-MS	10.73	0.74	9.42	17.20	12.92	1.15	11.01	26.15	12.92	2.59	6.22	16.15
Nd	ppm	ICP-MS	39.7	2.8	34.2	63.1	48.7	3.6	42.2	99.5	48.7	6.6	23.8	60.9
Sm	ppm	ICP-MS	7.28	0.94	5.86	10.57	9.43	0.56	8.53	16.27	9.48	1.48	4.58	11.29
Eu	ppm	ICP-MS	1.17	0.19	0.53	1.40	0.94	0.07	0.71	1.77	0.91	0.10	0.12	1.04
Gd	ppm	ICP-MS	6.22	1.11	4.88	9.23	9.23	0.61	7.38	15.71	9.71	0.42	5.53	10.15
Tb	ppm	ICP-MS	0.95	0.22	0.72	1.48	1.57	0.15	1.09	2.32	1.56	0.11	0.90	1.74
Dy	ppm	ICP-MS	5.87	1.64	4.12	9.52	9.83	1.69	5.91	14.25	9.35	1.11	5.84	10.74
Ho	ppm	ICP-MS	1.26	0.38	0.77	1.95	2.01	0.48	1.12	2.90	1.91	0.27	1.35	2.21
Er	ppm	ICP-MS	3.93	1.22	2.34	6.44	6.50	1.81	3.30	9.19	5.80	0.85	4.30	7.42
Tm	ppm	ICP-MS	0.58	0.18	0.36	0.98	0.95	0.31	0.50	1.46	0.89	0.17	0.65	1.07
Yb	ppm	ICP-MS	3.74	1.08	2.25	6.30	6.26	1.97	3.22	10.14	6.12	0.94	4.34	7.78
Lu	ppm	ICP-MS	0.59	0.19	0.33	0.97	0.96	0.30	0.51	1.70	0.95	0.16	0.68	1.20

Table 1. *(Cont.)*

	Unit N Setting Method	Rhyolitic ash-siltstone 6 Footwall				Rhyolitic pumice breccia 8 Footwall				Håkansboda limestone 9 Footwall			
		Median	MAD	Minimum	Maximum	Median	MAD	Minimum	Maximum	Median	MAD	Minimum	Maximum
SiO_2	% ICP-ES	74.32	0.84	71.65	75.35	76.78	0.70	74.48	77.88	5.12	2.19	1.87	13.10
TiO_2	% ICP-ES	0.14	0.05	0.08	0.55	0.13	0.01	0.10	0.15	<0.01	<0.01	<0.01	0.04
Al_2O_3	% ICP-ES	12.27	0.25	11.74	14.34	11.94	0.38	10.85	14.51	0.62	0.27	0.17	2.01
Fe_2O_3 total	% ICP-ES	2.93	0.40	2.30	3.99	2.89	0.91	1.93	4.13	4.08	0.89	2.64	5.82
MnO	% ICP-ES	0.22	0.08	0.09	0.31	0.11	0.04	0.04	0.17	0.40	0.04	0.30	0.72
MgO	% ICP-ES	1.61	0.13	1.43	2.04	1.20	0.23	0.73	1.48	18.12	0.64	15.49	19.01
CaO	% ICP-ES	1.48	0.66	0.49	2.85	0.69	0.26	0.36	1.35	29.08	0.63	25.75	30.45
Na_2O	% ICP-ES	0.76	0.21	0.34	1.02	2.32	0.60	1.17	3.77	0.06	0.04	<0.01	0.16
K_2O	% ICP-ES	3.87	0.81	2.97	5.93	2.20	0.37	1.25	3.08	0.10	0.08	<0.01	0.69
P_2O_5	% ICP-ES	<0.01	<0.01	<0.01	0.12	0.02	<0.01	0.01	0.02	<0.01	<0.01	<0.01	<0.01
Total C	% Leco	0.05	0.03	<0.02	0.17	0.03	<0.02	<0.02	0.09	11.97	0.48	9.76	12.89
S	% Leco	<0.02	<0.02	<0.02	0.05	<0.02	<0.02	<0.02	<0.02	<0.02	<0.02	<0.02	<0.02
LOI	% ICP-ES	1.9	0.3	1.4	2.5	1.9	0.3	0.9	2.2	42.0	1.1	35.1	44.7
Total	% ICP-ES	99.89	0.03	99.76	99.91	99.93	0.01	99.85	99.94	99.69	0.02	99.67	99.74
Zr	ppm ICP-MS	159.0	22.2	136.8	205.0	170.6	13.0	146.8	204.6	9.4	4.9	2.9	32.2
Y	ppm ICP-MS	29.0	2.1	26.5	31.5	35.7	1.0	32.5	43.8	4.9	1.7	2.9	10.9
Nb	ppm ICP-MS	10.7	0.9	9.7	14.2	11.9	1.4	9.8	20.1	0.5	0.3	<0.1	1.7
Co	ppm ICP-MS	1.5	0.7	0.5	2.9	1.3	0.2	0.8	1.7	2.7	0.3	2.4	4.1
Cr_2O_3	% ICP-ES	<0.002	<0.002	<0.002	0.001	<0.002	<0.002	<0.002	<0.002	<0.002	<0.002	<0.002	<0.002
Ni	ppm ICP-MS	0.7	0.1	0.5	2.2	0.4	0.0	0.2	0.4	<0.1	<0.1	<0.1	2.1
Ba	ppm ICP-ES	563	162	358	1,532	254	68	162	550	14	5	3	3,029
Rb	ppm ICP-MS	147.4	29.9	112.5	193.5	108.3	15.4	44.8	131.1	2.4	2.3	<0.1	20.7
Sr	ppm ICP-MS	18.5	6.6	6.1	25.6	14.3	5.3	7.9	31.4	17.4	2.0	15.0	37.9
Cu	ppm ICP-MS	6.3	5.5	0.8	19.0	1.7	0.6	0.8	3.1	0.7	0.3	0.2	1.5
Pb	ppm ICP-MS	14.7	2.1	11.2	318.1	8.8	3.3	4.9	40.4	1.2	0.6	0.6	8.5
Zn	ppm ICP-MS	21	6	11	34	35	10	22	77	2	1	1	9
As	ppm ICP-MS	1.7	1.1	0.6	13.8	0.3	0.0	0.3	0.9	<0.5	<0.5	<0.5	<0.5
Ag	ppm ICP-MS	0.2	<0.1	<0.1	5.9	<0.1	<0.1	<0.1	0.1	<0.1	<0.1	<0.1	<0.1
Au	ppb ICP-MS	<0.5	<0.5	<0.5	1.1	<0.5	<0.5	<0.5	0.7	1.6	<0.5	<0.5	2.4
B[2]	ppm NaOH fusion + ICP finish	130	105	20	340	15	10	<10	70	20	0	<10	20
Be	ppm ICP-MS	2	1	<1	4	2	1	<1	4	<1	<1	<1	2
Bi	ppm ICP-MS	0.2	0.2	<0.1	0.7	<0.1	<0.1	<0.1	0.3	<0.1	<0.1	<0.1	<0.1
Cd	ppm ICP-MS	<0.1	<0.1	<0.1	0.1	<0.1	<0.1	<0.1	0.1	<0.1	<0.1	<0.1	<0.1
Cs	ppm ICP-MS	3.8	1.4	1.6	5.2	1.4	0.4	0.6	3.8	0.2	0.2	<0.1	3.4
Ga	ppm ICP-MS	14.6	0.9	12.7	16.1	13.6	0.9	11.0	19.5	<0.5	<0.5	<0.5	1.9
Hf	ppm ICP-MS	5.1	0.3	4.6	6.1	5.5	0.2	5.1	6.7	0.3	0.1	<0.1	0.9
Hg	ppm ICP-MS	<0.01	<0.01	<0.01	0.010	<0.01	<0.01	<0.01	<0.01	<0.01	<0.01	<0.01	<0.01
Mo	ppm ICP-MS	0.8	0.2	0.2	1.0	0.7	0.5	<0.1	1.9	<0.1	<0.1	<0.1	0.3
Sb	ppm ICP-MS	0.8	0.5	0.1	2.8	<0.1	<0.1	<0.1	0.3	<0.1	<0.1	<0.1	<0.1
Sc	ppm ICP-MS	8	1	6	12	6	1	4	6	<1	<1	<1	1
Se	ppm ICP-MS	<0.5	<0.5	<0.5	<0.5	<0.5	<0.5	<0.5	<0.5	<0.5	<0.5	<0.5	0.50
Sn	ppm ICP-MS	3	0	2	3	3	1	<1	5	<1	<1	<1	<1
Ta	ppm ICP-MS	1.1	0.0	0.7	1.1	1.0	0.2	0.7	1.6	<0.1	<0.1	<0.1	<0.1
Tl	ppm ICP-MS	0.1	<0.1	<0.1	0.5	<0.1	<0.1	<0.1	<0.1	<0.1	<0.1	<0.1	<0.1
Th	ppm ICP-MS	11.9	1.2	10.5	15.4	13.1	0.4	11.9	16.4	<0.2	<0.2	<0.2	1.1
U	ppm ICP-MS	3.5	0.4	3.1	5.5	4.7	0.6	3.1	5.5	<0.1	<0.1	<0.1	<0.1
V	ppm ICP-MS	<8	<8	<8	37	<8	<8	<8	<8	<8	<8	<8	<8
W	ppm ICP-MS	2.2	0.4	1.2	3.2	1.5	0.3	0.9	2.8	<0.5	<0.5	<0.5	1.0
La	ppm ICP-MS	36.4	3.1	31.1	44.6	38.3	4.6	31.9	45.2	4.1	0.9	3.0	9.6
Ce	ppm ICP-MS	79.3	5.8	69.1	90.1	79.9	10.9	61.6	97.0	7.4	1.5	5.7	16.2
Pr	ppm ICP-MS	8.64	0.71	7.92	10.59	9.25	1.06	7.34	11.55	0.86	0.16	0.63	1.73
Nd	ppm ICP-MS	32.7	2.8	29.9	40.1	34.7	4.5	28.1	44.7	3.3	0.5	2.8	6.6
Sm	ppm ICP-MS	6.31	0.87	5.20	7.81	6.86	0.90	5.45	9.00	0.83	0.25	0.50	1.58
Eu	ppm ICP-MS	0.82	0.25	0.47	1.26	0.94	0.12	0.77	1.13	0.18	0.07	0.10	0.42
Gd	ppm ICP-MS	5.72	0.63	4.81	6.55	6.38	0.74	5.21	7.90	1.17	0.30	0.65	2.40
Tb	ppm ICP-MS	0.87	0.06	0.77	0.94	1.02	0.09	0.89	1.22	0.16	0.06	0.08	0.33
Dy	ppm ICP-MS	5.25	0.26	4.75	5.79	6.19	0.38	5.78	7.83	0.86	0.30	0.42	1.74
Ho	ppm ICP-MS	1.04	0.09	0.95	1.16	1.36	0.06	1.22	1.79	0.15	0.06	0.09	0.32
Er	ppm ICP-MS	3.21	0.19	2.96	3.58	4.22	0.27	3.78	5.39	0.43	0.09	0.24	0.70
Tm	ppm ICP-MS	0.48	0.03	0.44	0.54	0.66	0.04	0.59	0.89	0.06	0.02	0.03	0.10
Yb	ppm ICP-MS	3.31	0.11	3.11	3.58	4.41	0.35	3.88	5.81	0.33	0.10	0.18	0.67
Lu	ppm ICP-MS	0.48	0.06	0.42	0.57	0.69	0.04	0.60	0.92	0.05	0.01	0.03	0.10

Abbreviations: ICP-ES = inductively coupled plasma-emission spectroscopy, ICP-MS = inductively coupled plasma-mass spectrometry
[1] Half of the lower detection limit was used during the calculation of median and MAD when element concentrations were below detection limit
[2] Only AcmeLabs samples at <2 wt % Zn

Table 2. Composition of Fe Oxide Deposits in the Lovisa Area

Unit		Hanging-wall BIF	Lovisa IF (upper part)	Lovisa IF (lower part)	Nya Backadahl IF	Lekeberg IF
Sample		LK20150086	LK20150024	LK20160072	LK20160109	LK20150087
E (RT90)		1464194	1464046	1464177	1464627	1464569
N (RT90)		6622251	6622491	6622250	6621999	6623165
Z (RT90)		–57	18	–269	–29	156
SiO_2	%	49.98	48.45	22.08	19	15.71
TiO_2	%	0.14	0.09	0.06	0.06	0.04
Al_2O_3	%	6.94	3.47	3.03	2.39	1.79
Fe_2O_3[1]	%	14.32	37.13	51.4	62.64	60.87
MnO	%	0.49	1.43	4.85	3.38	3.38
MgO	%	1.21	2.63	5.32	7.58	10.3
CaO	%	13.72	5.32	0.88	1.37	2.14
Na_2O	%	0.41	0.2	<0.01	0.02	<0.01
K_2O	%	3.31	1.05	0.56	0.11	0.29
P_2O_5	%	0.09	0.2	<0.01	<0.01	0.06
Total C	%	2.42	0.08	0.81	1.28	2.12
Total S	%	0.04	0.09	1.52	0.62	0.52
Cr_2O_3	%	<0.002	0.003	<0.002	0.002	<0.002
LOI	%	9.3	-0.1	5.1	2.7	5.3
Sum	%	99.87	99.88	93.23	99.34	99.87
Zr	ppm	102.3	46.1	47.9	37.4	24.3
Y	ppm	22.6	14.4	23.3	35.6	15.6
Nb	ppm	7	3.2	2.8	2.3	2.5
Co	ppm	5.5	3.1	8.2	16.4	26
Ni	ppm	5.3	3.9	1.3	4.4	17.7
Ba	ppm	316	492	374	239	247
Rb	ppm	138.6	27.4	33.3	7	12.3
Sr	ppm	39.4	11.4	1.9	10.1	3.2
Cu	ppm	59.3	6.5	96	831.3	515.7
Pb	ppm	10	79.3	62,900	3,558.9	6.1
Zn	ppm	50	37	3,051	50	14
As	ppm	1.7	19	40.7	176.2	20
Ag	ppm	0.2	0.2	181	128	0.9
Au	ppb	1.9	<0.5	3	2.7	<0.5
B	ppm	30	<10	40	<10	60
Be	ppm	7	5	1	4	<1
Bi	ppm	0.9	0.1	4	10.6	22.3
Cd	ppm	<0.1	<0.1	28.3	0.8	<0.1
Cs	ppm	2.2	1.3	5.1	3	2.3
Ga	ppm	9.8	4.8	7.9	5.7	7.2
Hf	ppm	2.8	1.5	1.3	1	0.6
Hg	ppm	<0.01	<0.01	0.01	0.09	<0.01
Mo	ppm	7.8	0.8	1.6	2.2	1.9
Sb	ppm	0.4	0.9	96.8	5.3	0.9
Sc	ppm	7	3	2	2	12
Se	ppm	<0.5	<0.5	0.5	<0.5	<0.5
Sn	ppm	2	1	2	<1	2
Ta	ppm	0.5	0.2	0.2	0.2	0.1
Tl	ppm	<0.1	<0.1	0.4	0.3	0.1
Th	ppm	7.9	3.6	3.3	3.1	2.1
U	ppm	3.1	1	2.3	3.8	2
V	ppm	27	14	4	4	9
W	ppm	5.4	1	0.6	0.6	1.1
La	ppm	24	10.3	31.4	39.2	31.7
Ce	ppm	44.5	18.6	45	49.8	50.5
Pr	ppm	5.2	2.21	4.69	5.52	5.76
Nd	ppm	20.4	8.2	17.2	21.3	21.7
Sm	ppm	3.97	2.3	3.59	4.49	4.03
Eu	ppm	0.68	0.48	0.65	0.61	0.6
Gd	ppm	4.1	2.37	4.26	5.9	3.76
Tb	ppm	0.62	0.4	0.58	0.8	0.49
Dy	ppm	3.78	2.23	3.38	4.8	2.55
Ho	ppm	0.74	0.49	0.66	0.95	0.5
Er	ppm	2.13	1.33	2.11	2.55	1.44
Tm	ppm	0.33	0.21	0.29	0.29	0.2
Yb	ppm	2.13	1.28	1.82	1.83	1.3
Lu	ppm	0.32	0.21	0.27	0.26	0.2

Abbreviations: BIF = banded iron formation, IF = iron formation
[1] Total Fe shown as Fe_2O_3
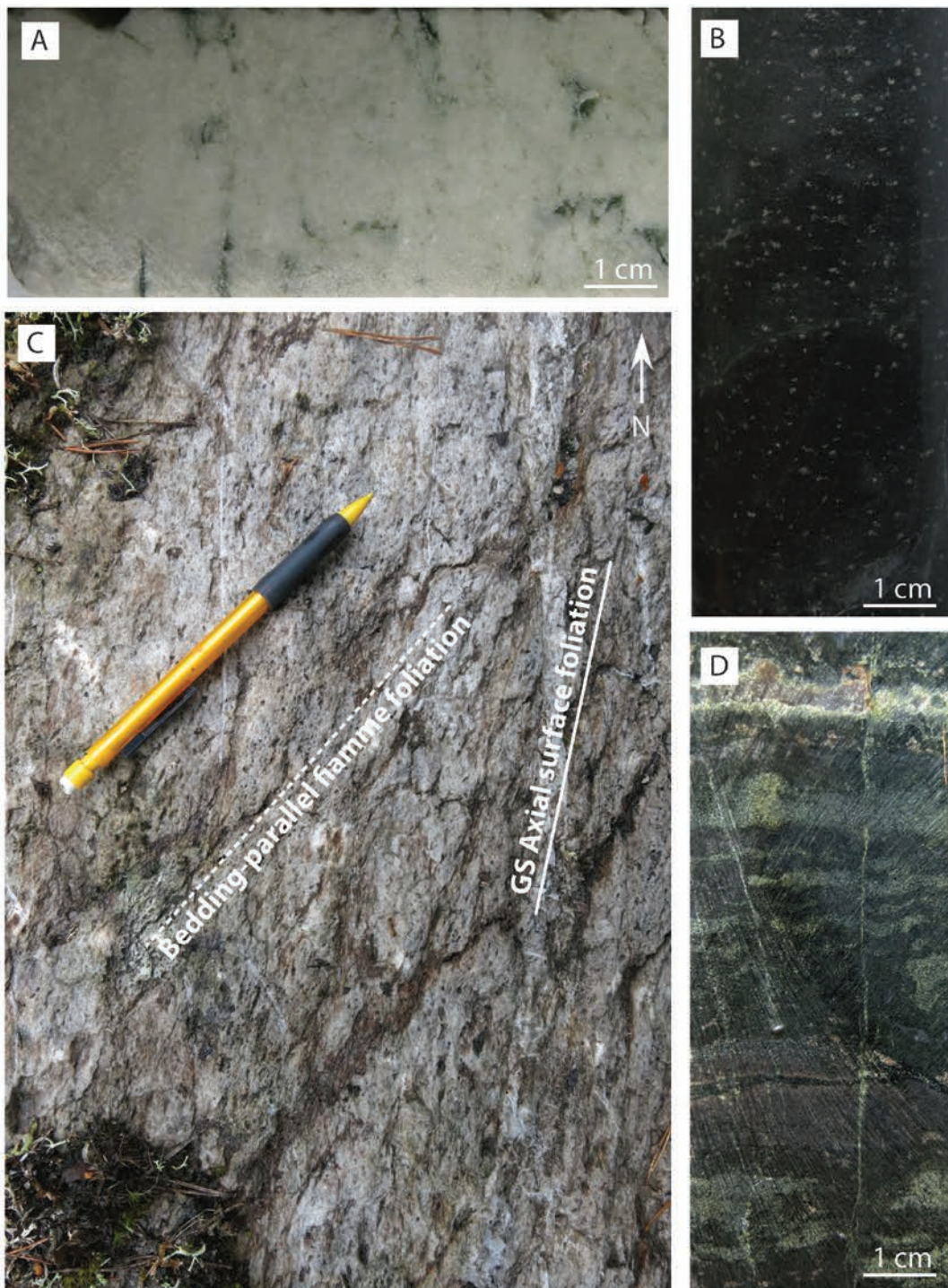
Fig. 7. Photographs of rock types in the stratigraphic footwall to the stratiform Zn-Pb ore. A: Massive dolomite marble with minor dark-green actinolite. B: Dark-gray finely feldspar + quartzphyric rhyolitic sandstone with minute porphyroblasts of sillimanite and garnet. C: Sericite-altered and compacted large pumice clasts (fiamme) in the footwall feldspar + quartzphyric rhyolitic pumice breccia. The former pumice clasts are aligned parallel to S_0 and are crenulated by S_1. D: Banded magnetite-actinolite-epidote-garnet rock from the lower Lovisa iron formation. E: Massive K-feldspar + quartzphyric rhyolite. F: Pink rhyolitic ash-siltstone with interbands of sericite-chlorite schist parallel to S_0. The sericite-chlorite schists have a subparallel foliation defined by alignment of mica, which is crenulated by a spaced S_1 foliation, which is here clearly visible in the ash-siltstone. The mica bands are rich in ca. 2- to 3-mm-round quartz phenocrysts. Pink rhyolitic ash-siltstone with streaks and blotches of clinochlore-pyrite-K-feldspar. The pink ground mass also carries tiny crystals of pyrite. G: Pink rhyolitic ash-siltstone with pyrite-porphyroblastic clinochlore patches.
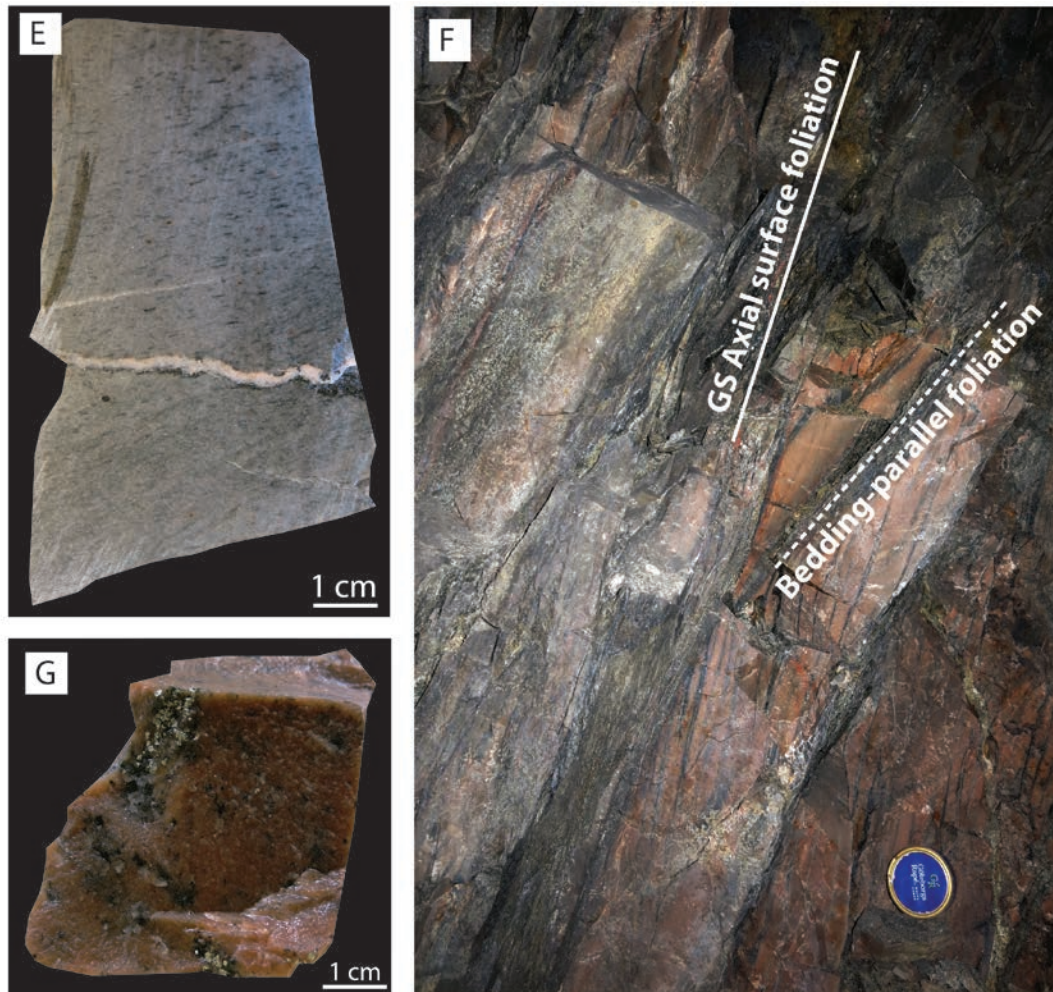
Fig. 7. *(Cont.)*

graded intervals confirm stratigraphic younging upward and to the southeast (Fig. 6).

The feldspar + quartzphyric rhyolitic pumice breccia has a sharp upper contact with an overlying 20- to 30-m-thick gray rhyolitic siltstone with minute garnet porphyroblasts (Fig. 5). The siltstone is in turn overlain by a ca. 25-m-thick succession of interbedded gray rhyolitic siltstone, bedded calc-silicate rock (garnet + amphibole), massive magnetite, and subordinate dolomite, here termed the "Lovisa Fe formation" (Fig. 7D).

The Lovisa Fe formation can be subdivided into a lower and an upper part, separated by an interbed of gray, garnet-porphyroblastic rhyolitic siltstone. A variable content of magnetite, ferrohornblende, calcic clinopyroxene, biotite, quartz and garnet, minor epidote, and microcline and trace apatite defines a banding parallel to bedding, which is less conspicuous in thin section (Fig. 8B). The biotite is rich in Ba (3.18 wt %) and Cl (1.56 wt %). Barite has not been observed. The amphibole displays alteration to micaceous meshes, but the amphibole crystal shapes are retained, indicating that the alteration was postkinematic and retrograde. Garnet occurs as up to centimeter-sized porphyroblasts ($Sps_{30-32}Alm_{37-39}Grs_{20-24}Adr_{7-9}Prp_{1-2}$) and as anhedral, skeletal crystals ($Sps_{38-42}Alm_{18-23}Grs_{22-26}Adr_{11-17}Prp_{2-3}$) arranged along grain

boundaries and forming rims around magnetite crystals (Fig. 8B). Despite slight compositional variations, there are no systematic zonation patterns in garnet; the compositional anhedral garnet reflects variations between different crystals in the same sample. Bands of massive magnetite in the lower part of the Lovisa Fe formation contain abundant disseminated galena with minor sphalerite and accessory Ag tetrahedrite, pyrite, chalcopyrite, and pyrrhotite (Fig. 8C). Overall, the Fe sulfide content in the Lovisa Fe formation is low.

East of the Engvall fault, the Nya Backadahl magnetite deposit (Fig. 3), which is interpreted as stratigraphically equivalent to the Lovisa Fe formation, is interbedded with a magnetite-free graphitic pelite with thin bands of sphalerite and galena. Electron microprobe analyses by Bleeker (1984) identified minor Ag tetrahedrite, allargentum, and dyscrasite.

The upper part of the Lovisa Fe formation is more distinctly banded and is immediately overlain by a meter-wide interval of very finely laminated gray siltstone, wherein laminae are defined by variable proportions of muscovite, quartz, microcline, plagioclase, and accessory minute tourmaline crystals. East of the Engvall fault, the equivalent interval hosts a gray-green, fine-grained calcite-altered mafic unit not present at Lovisa. It has not been possible to determine whether it is
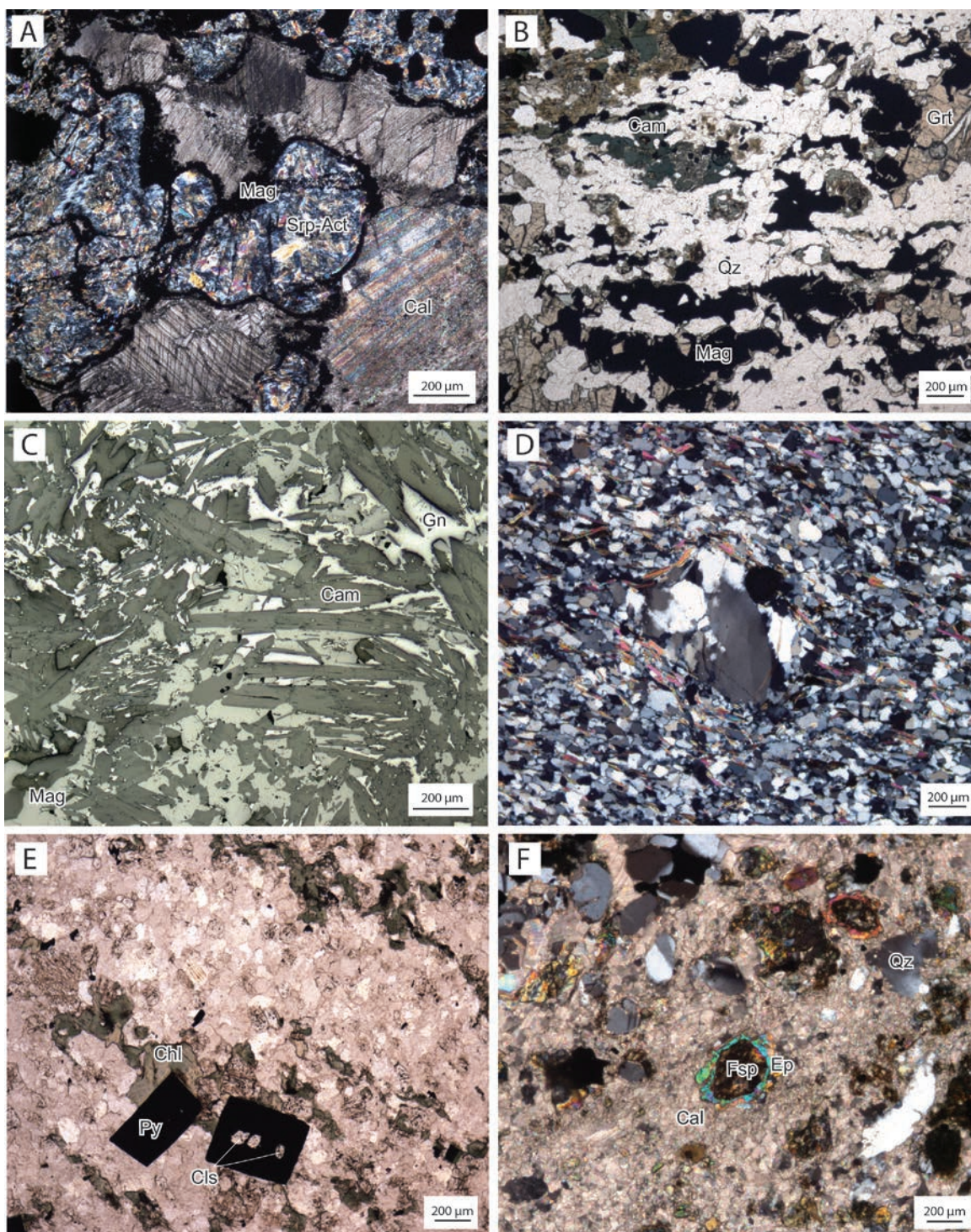
Fig. 8. Photomicrographs of A: Lekeberg iron formation, constituting magnetite (Mag) veining and rimming serpentine-actinolite intergrowths (Srp-Act) in a calcite (Cal) groundmass. The serpentine-actinolite intergrowths are interpreted as products of retrograde alteration of former olivine. Sample LK20160101. B: Lovisa Fe formation. Heavily disrupted and recrystallized magnetite (Mag) laminae in a quartzose (Qz) groundmass. Anhedral magnesiohornblende (Cam) and garnet (Grt) accompanies magnetite, with the garnet commonly forming delicate rims around magnetite lenses. Sample LK20150024. C: Lovisa Fe formation. Intergrown magnesiohornblende, magnetite, and galena (Gn). D: Recrystallized quartz phenocryst in weakly sericite-altered massive feldspar + quartzphyric rhyolite stratigraphically ca. 25 m below the Lovisa Zn-Pb deposit. Sample LK20150036. E: Clinohlore (Chl)-Pyrite (Py)-Celsian (Cls) alteration patches in pyritic rhyolitic silt-sandstone directly stratigraphically below the Lovisa Zn-Pb deposit. Sample LK20150081. F: Calcite-rich band in the interlaminated calcitic limestone (Cal), magnetite, and red rhyolitic ash-siltstone of the stratigraphic hanging wall. The band carries abundant detrital crystals of quartz (Qz) and feldspar (Fsp). Epidote (Ep) rims and partly replaces original detrital feldspar crystals. Sample LK20150086.

intrusive or extrusive, and the paucity of data in this area precludes determination of its distribution and geometry.

The laminated gray siltstone is overlain by rhyolitic sandstone, varying from nearly aphyric to containing ca. 3 to 4 vol % diffuse 1- to 2-mm feldspars and a few stretched 1- to 3-mm quartz phenocrysts (Figs. 7E, 8D). The metamorphic grain size is on average ca. 0.1 mm and the main minerals are quartz, feldspars, muscovite, and chlorite.

Lenses of sericite schist up to 0.5 m wide with abundant 2-mm quartz phenocrysts occur locally (Fig. 7F). The lenses are predominantly concordant but locally crosscutting. They may constitute either altered clasts of quenched rhyolite (peperite) or large pumice clasts (cf. Allen et al., 1996). The latter interpretation is favored, based on lack of evidence for coherent rhyolitic rocks in this part of the Guldsmedshyttan syncline.

Minute (ca. 0.5–1 mm) pyrite porphyroblasts are common in the rhyolitic sandstone unit and increase in abundance stratigraphically upward toward the Lovisa Zn-Pb deposit, where the unit gradually fines to silt size and attains a distinct pink-red color. This unit is almost exclusively composed of feldspar and quartz in addition to minor chlorite and local 1- to 3-mm magnetite porphyroblasts. The feldspar is mainly albite-oligoclase, although there are local zones with complexly growth-zoned celsian or barian microcline, which is intergrown with pyrite and clinochlore (pyknochlorite-ripidolite) in disseminations, patches, and veins (Figs. 8E, 9A, B). Celsian occurs as inclusions in pyrite (Fig. 8E). Barite has not been observed.

Stratigraphic hanging wall: The Lovisa Zn-Pb deposit is overlain by a succession of gray-pink ash-siltstone (Fig. 10A), which is dominated by plagioclase and quartz. Lithogeochemical data suggests that the precursor rock was of rhyolitic composition and that the plagioclase is largely secondary in origin. The ash-siltstone is sharply overlain by a ca. 80-m-thick, fining-upward succession of coarse-grained rhyolitic volcaniclastic rocks (Fig. 10B). Sharp and gradational transitions in grain size suggest the succession consists of several normal graded subunits. The lowermost unit displays normal grading over ca. 10 m from basal breccia with lithic clasts of rhyolitic ash-siltstone, to rhyolitic pumice breccia with 10 to 15 vol % 2-mm feldspar and 1 to 3 vol % 1- to 2-mm quartz crystals, to crystal-bearing sandstone and uppermost, indistinctly laminated rhyolitic siltstone. The overlying units contain similar matrix-supported pumice clasts but contain 2- to 4-mm quartz phenocrysts (Fig. 10B). The phenocrysts are mostly confined to former pumice clasts. Biotite is the mafic phase and is commonly variably chloritized. At the base, plagioclase is the only feldspar, but the proportion of microcline increases stratigraphically upward.

A gradational transition is observed from the coarse-grained succession into an overlying massive gray to pink rhyolitic siltstone, with rare thin interbeds of banded limestone. Approximately 150 m above the Lovisa ore horizon, a thin BIF is present, consisting of centimeter-thin bands of magnetite regularly interbedded with white calcite limestone, chlorite-rich bands, and massive, red, jasper-like rhyolitic ash-siltstone (Fig. 10C). The rhyolitic ash-siltstone is dominated by quartz and microcline, and the red coloration is likely due to the presence of submicron hematite crystals. Magnetite is mainly present in the stratigraphically lower part of this subunit but gradually diminishes stratigraphically upward, whereas the interbedding of limestone and red siltstone prevails. Minor amphibole, epidote, and garnet formed at the contacts between compositionally distinct bands and as rims around feldspar crystals in carbonate-rich matrix (Fig. 8F), but the calc-silicate content is generally low except in and around faults (Fig. 10C). The garnet is predominantly andradite rich ($Adr_{68}Grs_{19}Sps_9Alm_4$) and ranges from anhedral to subhedral. The andradite-rich garnet is discontinuously overgrown by more alumina-rich garnet ($Adr_{19}Grs_{31}Sps_{27}Alm_{21}$).

Mineralization

Zinc ± lead mineralization is confined to a 5- to 10-m-thick stratigraphic interval that contains sphalerite laminae, sphalerite-galena veins, and sphalerite-galena with a durchbewegung texture in strongly banded, gray to pink-red, cherty rhyolitic ash-siltstone with lesser interbeds of clinochlore schist (pyknochlorite-ripidolite). The term "durchbewegung texture" refers
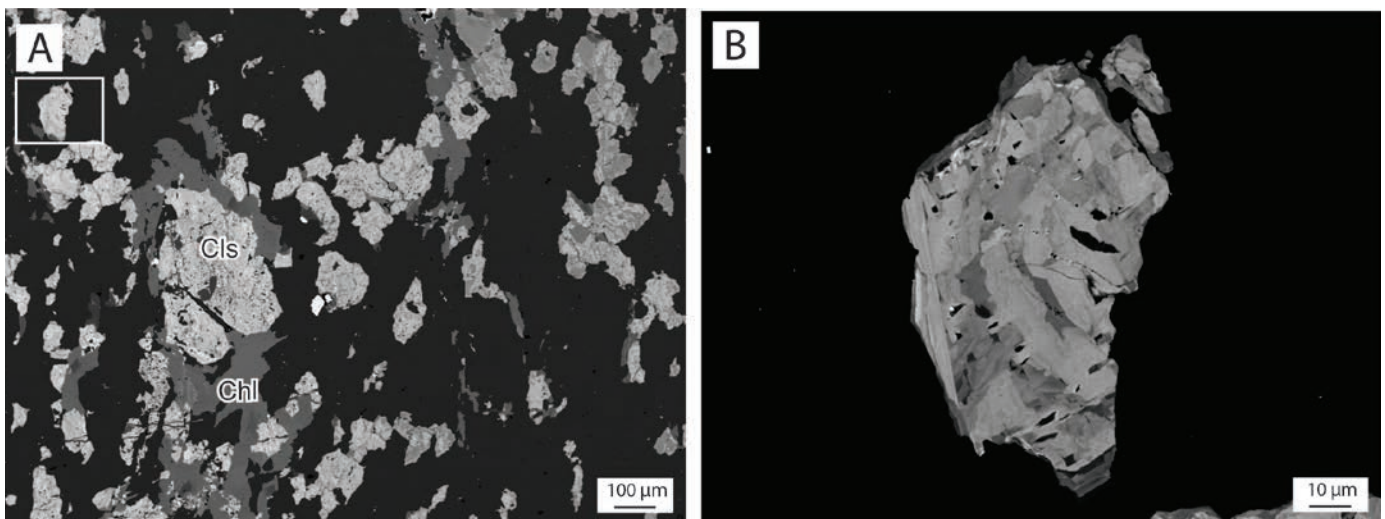

Fig. 9. Backscattered electron images: A: Clinochlore (Chl)-celsian (Cls) alteration patch in pyritic rhyolitic silt-sandstone (same sample as in Figure 8E). B: Close-up of area in box in A, revealing complex zonation patterns in celsian, defined by variable contents of Ba. Sample LK20150081. The difference in gray mainly reflects difference in the Ba content in the feldspar.

Fig. 10. Photographs of facies in the stratigraphic hanging wall of the stratiform Zn-Pb ore. A: Gray rhyolitic ash-siltstone. B: Feldspar + quartzphyric rhyolitic pumice breccia. C: F_1 folded, interlaminated calcitic limestone, magnetite, and red rhyolitic ash-siltstone. Minor amphibole and garnet occur along some bands, and epidote occurs within a crosscutting fault. Hammer for scale is 63 cm long.

to highly ductile deformed, very fine grained massive sulfide mineralization with subrounded to rounded clasts of vein quartz and host rock (Marshall and Gilligan, 1987).

Mining specifically targets two, 0.1- to 1-m-thick, bedding-concordant zones of massive to semimassive sulfide. The lower "sphalerite ore" consists of bedding-parallel layers of sphalerite-dominant sulfide interbedded with rhyolitic ash-siltstone and chlorite schist (Fig. 11A), whereas the upper "main ore" is a tabular body of massive galena-sphalerite accompanied by peripheral laminated sphalerite + galena crosscut by sphalerite + galena veins. Pyrrhotite is rare in both ore types. The calc-silicate content in this stratigraphic interval is very low. The main ore is present throughout the mine whereas the sphalerite ore only occurs in the southern

part. The sphalerite is commonly yellow to beige in color and Carlon (1987) reported Fe contents are relatively low, varying from 1.6 to 2.2 wt % and averaging 2.0 wt %.

Rhyolitic interbeds in the sphalerite ore are commonly boudinaged and define Z-symmetric folds (when viewed downward). The folds are locally disharmonic as the contacts may be planar and lack folding in the same exposure, suggesting that they result from layer-parallel shearing (Fig. 11A). A thin zone of strongly pyrite impregnated chlorite schist interbedded with pink rhyolitic siltstone is locally present at the lower contact of the sphalerite ore (Fig. 11B). Pyrite porphyroblasts locally form S_0-parallel trains. The sphalerite ore has been traced to the hinge and western limb of the Lovisa anticline, where it is discontinuous and less endowed in base metals (Fig. 5). It

gradually thins out and disappears at the north end of the mine.

The gangue minerals in the sphalerite ore are mainly K-feldspar, clinochlore (pyknochlorite-ripidolite), quartz, muscovite, with minor clinozoisite, magnesiohornblende, calcite, millimeter-sized garnet porphyroblasts ($Alm_{36-41}Sps_{28-33}Grs_{21-29}Prp_{3-4}Adr_{0-2}$), and accessory tourmaline and allanite (Fig. 11C). The compositional range in garnet reflects a core-to-rim zonation, involving decreasing spessartine and almandine and increasing grossular. Although Carlon (1987) reported diopside in the ore zone, no pyroxene was found in the ore zone during the current study. Minor porphyroblastic overgrowths of pyrite and arsenopyrite on sphalerite produce a poikiloblastic texture and were seemingly unaffected by a tectonic foliation defined mainly by micas. Stratification is defined by interbedded rhyolitic ash-siltstone and yellow to beige sphalerite, millimeter-scale variability in sphalerite abundance, and locally by trains of pyrite porphyroblasts.

The main ore is commonly characterized by 1- to 10-mm-round fragments of wall rock and dark-gray vein quartz in a fine-grained, gray, sphalerite-galena matrix, i.e., a durchbewegung texture (Fig. 11D, E). Gangue minerals include K-feldspar, chlorite, accessory graphite, and rare tourmaline. The main ore is generally subparallel to S_0 and its strike similarly curves from northeast to a north-northeast direction when traced from north to south in the mine (Fig. 5). The main ore dips 60° to 70° toward the east-southeast but flattens out at depth (Figs. 6, 9D, F). A peripheral zone of laminated, yellow sphalerite occurs adjacent to the ore with a durchbewegung texture (Fig. 11F). The laminated sphalerite facies locally displays complex sheath folds (0.5–1 m wide) that are truncated by ore with durchbewegung texture. Veins of coarsely crystalline sphalerite and galena peripheral to the ore with durchbewegung texture locally crosscut the laminated facies.

The composition of the two ore layers, based on representative ore grade samples, is provided in Table 3. All varieties of Lovisa ore are characterized by a dominance of Zn over Pb yet vary in terms of their Zn/Pb ratio (Fig. 12). The sphalerite ore contains minor Cu and Pb (Zn/Pb averages 43), reflecting a low content of chalcopyrite and galena. It is compositionally much more homogeneous than the main ore. The ore with durchbewegung texture has heterogeneous Zn and Pb contents and exhibits significantly lower Zn/Pb (around 3.8) than the sphalerite ore. The laminated main ore facies is similarly highly variable in composition, but it is always more Pb rich than the sphalerite ore (Fig. 12). The various ore facies in the main ore are also generally more Ag rich, even though Ag/Pb is higher in the sphalerite ore. Data are insufficient to model the metal zonation in the two main massive sulfide beds in detail. However, if the Lovisa Zn-Pb ore zone is considered in bulk, the gradational disappearance of the sphalerite ore from the southern to the northern part of the mine means that there is a general decrease in the sphalerite content from south to north. All types of ore in the Lovisa Zn-Pb deposit have distinctly higher Zn/Pb than the Pb-Ag mineralization in the lower Lovisa Fe formation and the correlative Nya Backadahl Fe formation (Fig. 12), and they lack magnetite.

Hydrothermal alteration

The stratigraphic footwall between the Håkansboda limestone and the pyrite-porphyroblastic pink-red rhyolitic siltstone-sandstone is commonly weakly sericite-chlorite altered and locally silicified (Fig. 13A). Minor porphyroblasts of garnet, amphibole, and sillimanite are common in this part of the stratigraphy and are similar in appearance to metamorphic porphyroblasts formed by regional metamorphism of hydrothermally altered volcanic rocks in many other parts of Bergslagen (e.g., Jansson et al., 2013; Kampmann et al., 2017)

Most samples display anomalously high K_2O/Na_2O compared with the igneous spectrum of Hughes (1973) (Fig. 13B). Plotting the chlorite-carbonate-pyrite index (CCPI; $100[MgO + FeO]/[MgO + FeO + Na_2O + K_2O]$) against the Ishikawa alteration index (AI; $100[K_2O + MgO]/[K_2O + MgO + Na_2O + CaO]$) can be used to visualize trends in hydrothermally altered volcanic rocks (Large et al., 2001). This shows that relative to other parts of the Lovisa stratigraphy, the deeper footwall rocks are slightly more chloritized. Furthermore, these rocks are the only ones that display a clear association between silicification and an increase in AI and CCPI (Fig. 13A, C).

Increasing albite and whole-rock Na_2O and decreasing K_2O/Na_2O define a zone of Na-enrichment stratigraphy upward toward the red pyritic siltstone (Fig. 13A). This pattern continues in the immediate stratigraphic hanging wall to the Lovisa ore zone, where Na enrichment extends into the lower part of the hanging-wall rhyolitic pumice breccia. An identical pattern of Na enrichment in the ore-equivalent stratigraphic interval also occurs on the western limb of the Lovisa anticline. Thus, this alteration style is stratabound, restricted to the Lovisa ore zone, and must predate folding. In detail, the massive sulfide layers occur in discrete intervals of high K_2O/Na_2O, reflecting the presence of K-feldspar within this broader alkali-altered zone (Fig. 14A). Many of the samples of red pyritic rhyolitic ash-siltstone directly stratigraphically below the Lovisa Zn-Pb deposit have also been silicified, as evidenced by anomalously high SiO_2 contents (Fig. 13A; Table 1).

In the upper hanging-wall rhyolitic ash-siltstones, silicification is generally patchy in nature and commonly developed as bleached patches, locally containing a few garnet porphyroblasts. Similar to the deeper part of the stratigraphic footwall, many samples have anomalously high K_2O/Na_2O (Fig. 13B), yet here there is no obvious positive correlation between K_2O/Na_2O and SiO_2.

Chemostratigraphy

The hydrothermal alteration overprint of the rocks precludes using the contents of major oxides for further stratigraphic subdivision (e.g., Fig. 14A). Plotting ratios of the commonly immobile Zr, Al_2O, and TiO_2 across stratigraphy reveals that the mapped stratigraphic intervals contain distinct negative and positive excursions in these ratios (Fig. 14B-D). These distinct compositional breaks corroborate the stratigraphic division. The coarser-grained volcaniclastic units are compositionally homogeneous, which most likely reflects their origin as rapidly emplaced, syneruptive mass flow deposits of pyroclastic debris derived from discrete volcanic events. In binary plots of Zr, Al_2O_3, and TiO_2, samples of these coarse-grained units lie along linear arrays anchored at the origin (Fig. 15A-C). These arrays are "alteration lines" in the sense of Barrett and MacLean (1994, 1999), i.e., trends resulting because Zr, Al_2O_3, and TiO_2 were immobile during alteration
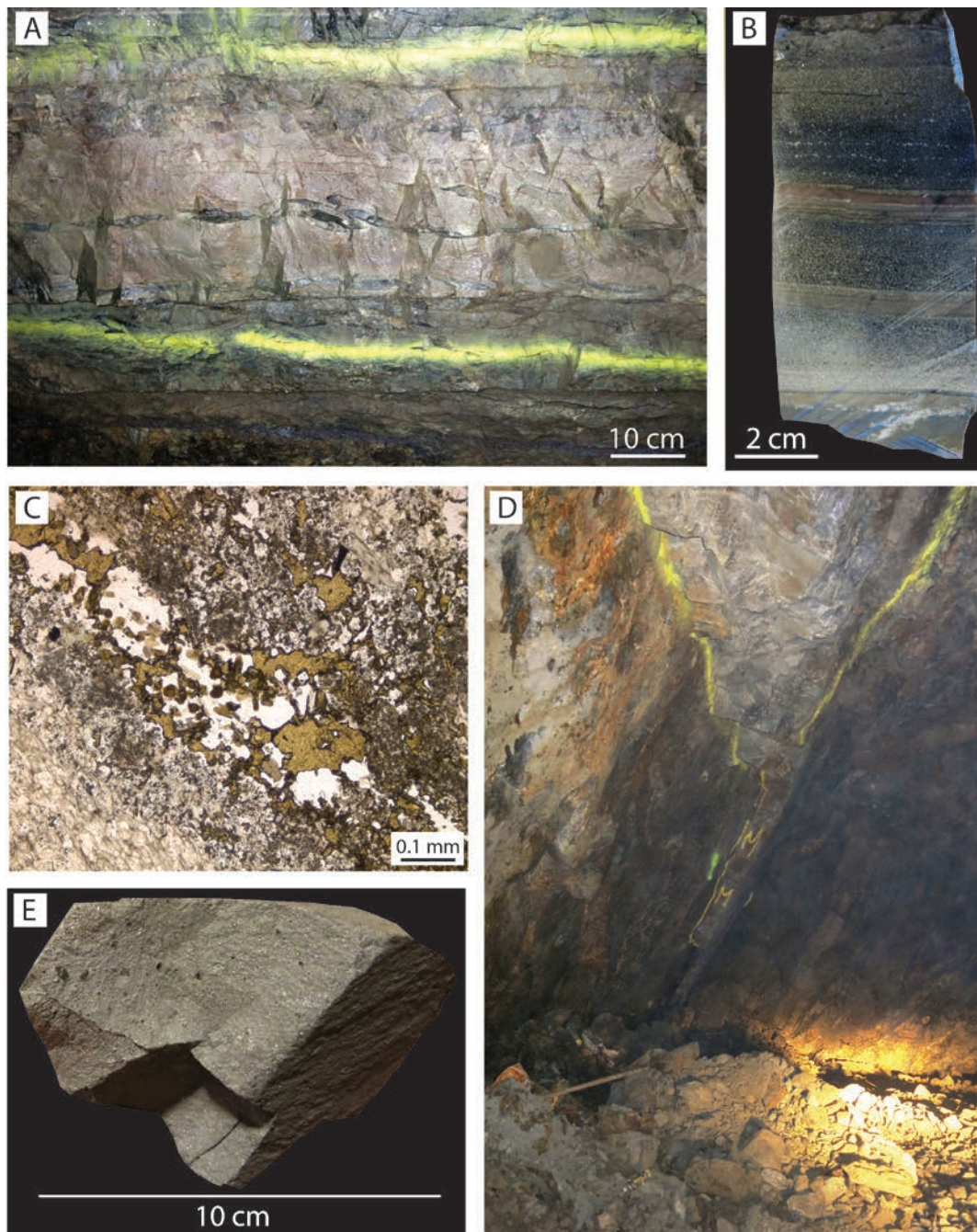
Fig. 11. Photographs and photomicrographs. A: The sphalerite ore, showing internal S folding of dark-gray interbeds of rhyo-litic ash-siltstone. Viewed upward at the 135-m level with contacts outlined with yellow spray paint. B: Pyrite-banded rhyolitic siltstone at the lower contact of the sphalerite ore. Sulfides are mainly hosted by the darker chloritic bands. C: Transmitted light photomicrograph, showing recrystallized sphalerite laminae with minute zoned crystals of tourmaline. D: The main ore, here ca. 0.4 m thick, viewed toward the south on the 135-m level; ore contacts outlined with yellow paint. Hammer lying in lower left part of image is 63 cm long. E: Main ore with durchbewegung texture, comprising small balls of gray quartz in a gray matrix of fine-grained sphalerite and galena. F: Example of a contact relationship of the main ore. The ore with durch-bewegung texture borders a zone of laminated yellow sphalerite. Both are crosscut by a chlorite-altered shear zone belonging to the central shear zone, which also crosscuts a gently dipping pegmatite crosscutting the main foliation. The displacement of pegmatite suggests a reverse sense of shear.

but decreased or increased in abundance due to a net mass gain or mass loss, respectively, of mobile components.

The narrow range in immobile element ratios indicates homogeneous original composition of the mass flow deposits.

The rhyolitic sandstone unit directly stratigraphically below the ore zone is similarly compositionally homogeneous. Based on this observation and textural evidence, it is likely that this unit is also associated with a discrete rhyolitic volcanic pulse

Fig. 11. *(Cont.)*

in the basin. Consequently, at least three compositionally distinct rhyolitic volcanic units are present. These three volcanic units have overlapping Al_2O_3/TiO_2 but can be distinguished based on Zr/Al_2O_3 and Zr/TiO_2. The volcanic unit directly underlying Lovisa has the highest Zr/TiO_2 and Zr/Al_2O_3.
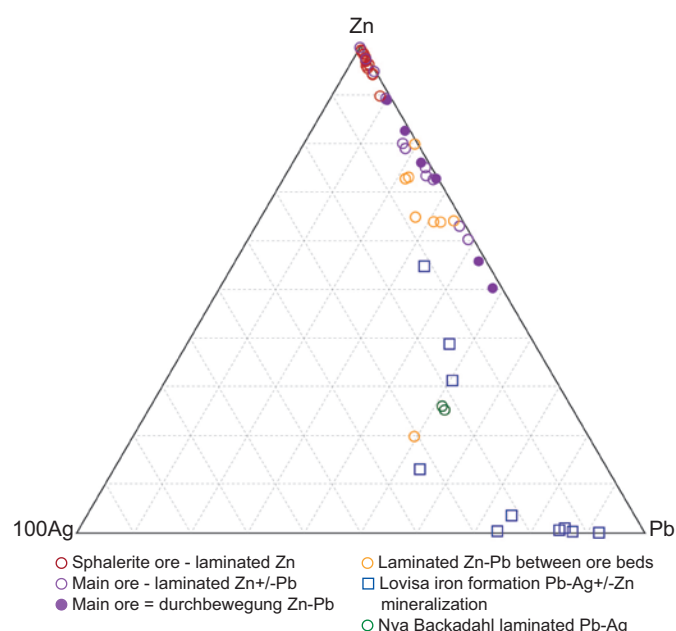
The immobile element ratios of the rhyolitic ash-siltstones are more compositionally heterogeneous and only partly overlap with those of the main volcanic units. The larger spread most likely reflects the more reworked character of these units and possibly indicates that they are composed of a distal ash component of variable provenance (cf. Allen et al., 1996).

Except for the Lovisa Fe formation, Zn contents are generally low (<100 ppm) below the massive rhyolitic sandstone of the stratigraphic footwall (Fig. 16A). The massive rhyolitic sandstone and the overlying pyritic red rhyolitic siltstone have slightly elevated Zn contents relative to other metavolcanic rocks in the succession. A sharp increase in Zn content is not encountered before the appearance of the sphalerite ore. Similar weak Zn anomalies extend up to the hanging-wall rhyolitic pumice breccia, above which Zn values return to <100 ppm levels, with the exception of a thin marble interbed below the hanging-wall BIF. The distribution of Pb and S follows a broadly similar pattern (Fig. 16B, C).

The Lovisa Zn-Pb deposit occurs in the only stratigraphic interval without carbonate, bedded calc-silicate rocks, or Fe oxide that shows positive Mn anomalies. However, the Fe formations, associated calc-silicate rocks, and limestone units display more pronounced positive anomalies (Fig. 16D). There are similarly discrete positive anomalies in P_2O_5 and V associated with the ore zone and the Fe formations (Fig. 16E, F).

Barium is generally <1,000 ppm except in the Lovisa Fe formation and in the immediate footwall of the ore zone (Fig. 16G). Sporadic B anomalies exist in the stratigraphic footwall up to the Lovisa Fe formation (Fig. 16H), but above this B is mostly below the 10-ppm lower limit of detection, despite the presence of trace tourmaline in the sphalerite ore.

Fig. 12. Ternary Zn-Pb-100Ag (wt %) plot showing the composition of the Lovisa sphalerite ore, different facies of the main ore, and the Lovisa Fe formation.

JANSSON ET AL.

Table 3. Weighted Geometric Mean,[1] Median, Mean Absolute Deviation (MAD), Quartiles, and
Compositional Range for Different Ore Types at Lovisagruvan (major elements in wt %, trace elements in ppm, except as noted)

	Mean	Median	MAD	Q1	Q3	Minimum	Maximum
				Main ore: Ball ore facies (*n* = 8)			
Si	13.82	15.00	2.54	10.77	15.65	6.59	21.51
Ti	0.10	0.10	0.02	0.08	0.12	0.05	0.14
Al	2.92	2.90	0.64	2.32	3.48	1.61	5.20
Fe	5.11	4.90	0.55	4.38	5.47	3.35	6.20
Mn	0.23	0.25	0.03	0.16	0.26	0.12	0.28
Mg	0.77	0.65	0.10	0.59	0.78	0.45	2.09
Ca	0.45	0.51	0.17	0.38	0.66	0.23	0.75
Na	0.10	0.09	0.07	0.04	0.27	0.02	0.56
K	1.35	1.54	0.13	1.28	1.65	0.36	2.96
P	0.04	0.04	0.01	0.03	0.04	0.02	0.05
Total C	0.21	0.21	0.04	0.19	0.25	0.15	0.26
Total S	15.55	16.52	1.19	16.06	18.48	8.62	19.72
LOI	8.73	9.22	0.41	8.88	9.52	5.71	10.67
Zr	67	61	19	44	74	37	211
Y	30	31	7	22	34	19	52
Nb	5	5	2	3	6	2	19
Co	6	7	1	6	7	5	8
Cr	27	26	4	22	31	21	35
Ni	6.0	5.9	0.6	5.2	6.2	5.0	7.7
Ba	220	222	109	133	311	72	475
Rb	68.7	76.1	17.8	48.8	87.5	19.4	188.2
Sr	5.3	6.0	2.7	3.6	9.0	3.1	13.0
Cu	51.1	71.3	34.1	36.5	98.1	26.8	125.8
Pb	70,852	75,757	40,389	51,885	149,825	32,414	242,750
Zn	265,532	283,400	21,475	273,088	304,725	147,500	333,800
As	17.5	16.2	2.0	14.4	17.2	13.6	22.6
Ag	39.75	48.13	20.34	32.90	73.25	16.93	96.00
Au (ppb)	<5	<5	<5	<5	9	<5	13
Bi	1.79	2.01	0.82	1.55	2.93	1.02	3.00
Cd	1,283.75	1,425.50	126.50	1,287.50	1,494.00	718.97	1,769.00
Cs	0.52	0.52	0.20	0.35	0.69	0.11	1.71
Ga	9.6	8.9	2.0	7.1	11.1	6.3	15.5
Hf	1.9	1.9	0.8	1.1	2.1	1.0	6.9
Hg	3.58	3.64	1.12	2.55	4.70	1.43	8.10
Mo	4.43	4.28	0.93	3.92	5.40	2.61	7.91
Sb	11.06	10.34	2.38	8.48	17.09	6.06	39.69
Se	0.7	0.7	0.1	0.6	0.8	0.6	1.2
Sn	5	6	<5	<5	14	<5	32
Ta	0.5	0.5	0.2	0.3	0.6	0.3	2.3
Tl	0.2	0.2	0.0	0.2	0.3	0.2	0.6
Th	5.70	5.62	1.70	3.90	6.84	2.59	14.32
U	2.08	1.95	0.57	1.36	2.39	1.13	5.34
V	21	21	3	19	25	14	28
W	0.9	1.3	0.8	0.5	2.0	0.5	3.0
La	40.6	41.9	6.4	35.3	45.5	27.4	53.2
Ce	72.7	73.2	10.2	63.1	80.8	49.9	101.7
Pr	8.34	8.37	1.13	7.07	9.33	5.71	11.82
Nd	31.4	31.9	5.3	26.1	35.3	21.0	45.2
Sm	6.45	6.40	1.05	5.64	7.13	4.35	9.20
Eu	1.68	1.66	0.15	1.54	1.93	1.06	2.65
Gd	6.62	6.57	1.18	5.73	7.54	4.50	9.33
Tb	1.00	1.01	0.22	0.81	1.18	0.65	1.50
Dy	5.57	5.57	1.23	4.42	6.65	3.48	8.86
Ho	1.04	1.06	0.22	0.79	1.21	0.65	1.81
Er	2.94	3.01	0.64	2.08	3.41	1.83	5.31
Tm	0.41	0.41	0.10	0.27	0.47	0.24	0.80
Yb	2.50	2.55	0.59	1.70	2.87	1.53	4.88
Lu	0.37	0.38	0.08	0.25	0.40	0.21	0.76

Table 3. *(Cont.)*

	Main ore: Laminated facies ($n = 3$)				Sphalerite ore: Laminated ($n = 7$)						
	Mean	Median	Minimum	Maximum	Mean	Median	MAD	Q1	Q3	Minimum	Maximum
Si	19.27	22.05	7.33	24.99	26.37	26.64	1.10	25.55	27.38	22.41	28.95
Ti	0.14	0.12	0.08	0.21	0.12	0.13	0.01	0.12	0.13	0.11	0.16
Al	5.50	5.51	5.26	5.59	5.06	5.10	0.40	4.85	5.38	4.20	5.85
Fe	4.37	4.71	2.75	11.17	3.60	3.56	0.34	3.38	4.02	3.23	4.16
Mn	0.20	0.18	0.15	0.48	0.29	0.27	0.02	0.25	0.34	0.20	0.44
Mg	1.09	0.87	0.75	4.58	0.92	0.80	0.07	0.78	1.23	0.74	1.39
Ca	0.50	0.54	0.21	0.65	1.50	1.48	0.36	1.18	1.83	0.39	2.28
Na	0.47	0.56	0.19	0.58	0.59	0.57	0.15	0.49	0.74	0.42	1.38
K	2.69	4.21	0.20	4.99	3.33	3.46	0.56	2.90	3.59	2.04	4.62
P	0.04	0.04	0.03	0.07	0.03	0.03	0.00	0.03	0.04	0.02	0.04
Total C	0.18	0.21	0.03	0.30	0.23	0.18	0.06	0.16	0.28	<0.02	0.46
Total S	8.34	8.08	6.59	16.06	7.50	7.50	0.42	7.32	8.29	6.27	8.66
LOI	5.50	4.82	4.52	12.31	4.89	5.05	0.17	4.88	5.22	4.37	5.60
Zr	143	155	91	158	135	136	11	127	147	125	175
Y	42	40	39	44	35	33	1	32	36	31	42
Nb	13	13	6	17	13	12	1	12	13	11	17
Co	5	8	3	9	4	4	1	4	5	3	5
Cr	42	32	19	74	34	33	4	30	36	28	84
Ni	8.5	11.4	5.0	15.3	4.9	5.0	0.2	4.9	5.2	4.3	5.5
Ba	467	660	19	1,219	410	406	43	385	461	271	1,100
Rb	107.5	174.4	8.2	190.3	123.5	116.6	8.4	111.8	124.7	89.0	163.4
Sr	10.2	11.3	3.3	14.7	13.2	13.6	2.1	12.2	14.6	11.1	19.8
Cu	108.1	206.7	23.7	366.2	25.2	25.0	5.3	21.5	29.7	17.0	108.0
Pb	26,356	15,505	15,183	55,969	2,970	3,138	757	2,279	3,816	1,004	3,916
Zn	135,067	137,200	97,603	290,200	128,088	125,900	3,600	124,150	137,900	106,550	151,600
As	8.3	9.2	6.0	14.2	10.1	8.2	4.0	6.6	17.2	4.2	43.3
Ag	14.82	16.01	9.02	16.79	6.23	5.97	1.13	5.40	7.45	3.52	9.91
Au (ppb)	<5	<5	<5	6	<5	<5	<5	<5	<5	<5	5
Bi	0.75	0.56	0.47	1.22	0.78	0.91	0.20	0.59	1.07	0.47	1.11
Cd	756.58	878.32	500.54	1,465.00	340.95	337.81	107.17	308.20	463.82	220.07	521.00
Cs	1.03	1.23	0.34	1.37	1.05	1.11	0.21	0.93	1.32	0.66	1.65
Ga	16.4	14.9	14.3	29.1	13.7	13.8	0.9	13.3	14.7	12.8	16.3
Hf	4.7	4.9	2.9	5.5	4.2	4.1	0.2	4.0	4.5	3.8	5.2
Hg	1.31	1.33	1.20	1.41	2.27	2.25	1.06	1.70	4.10	0.99	6.40
Mo	4.28	2.87	2.37	8.97	2.96	2.56	0.33	2.35	3.19	0.80	4.62
Sb	4.77	6.12	1.16	6.63	2.17	1.67	0.45	1.58	2.94	1.22	3.92
Se	0.6	0.6	0.6	0.8	0.7	0.7	0.1	0.6	0.7	0.6	4.8
Sn	10	10	<5	19	<5	<5	<5	<5	<5	<5	13
Ta	1.0	0.9	0.6	1.3	1.0	1.0	0.0	0.9	1.1	0.9	1.1
Tl	0.1	<0.1	<0.1	0.1	0.2	0.1	0.0	0.1	0.2	0.1	0.4
Th	13.04	11.79	11.53	15.43	10.47	10.90	0.43	10.44	11.18	8.48	13.13
U	4.72	4.30	4.17	5.58	5.31	3.66	0.36	3.43	4.56	3.21	25.02
V	43	39	29	64	24	25	1	24	26	21	27
W	2.1	2.0	0.5	4.0	0.7	0.5	0.0	0.5	0.6	0.5	3.0
La	45.5	56.9	32.9	59.3	34.7	36.0	1.6	34.5	37.5	29.3	47.3
Ce	86.1	106.3	64.1	107.1	68.2	68.5	3.5	66.3	71.4	60.2	93.8
Pr	9.84	12.07	7.37	12.31	8.15	8.25	0.40	8.05	8.57	7.16	11.24
Nd	37.1	45.1	28.3	45.4	30.2	30.8	1.4	29.9	31.7	26.5	41.1
Sm	7.32	8.63	5.76	8.73	5.98	6.23	0.24	5.92	6.38	5.23	7.70
Eu	1.73	1.84	1.26	2.33	0.91	0.97	0.12	0.85	0.99	0.82	1.14
Gd	7.61	8.75	6.14	9.22	5.91	6.01	0.32	5.81	6.20	5.30	7.38
Tb	1.19	1.36	0.99	1.37	0.94	0.95	0.00	0.94	0.95	0.83	1.15
Dy	7.26	7.57	6.47	8.03	5.68	5.60	0.18	5.47	5.86	5.18	6.76
Ho	1.44	1.45	1.33	1.56	1.16	1.15	0.05	1.11	1.21	1.06	1.39
Er	4.38	4.20	4.14	4.72	3.61	3.47	0.18	3.35	3.82	3.24	4.35
Tm	0.63	0.59	0.58	0.69	0.54	0.51	0.02	0.50	0.56	0.47	0.66
Yb	4.16	3.93	3.64	4.66	3.54	3.32	0.05	3.27	3.71	3.15	4.41
Lu	0.62	0.60	0.53	0.69	0.53	0.50	0.03	0.48	0.56	0.47	0.69

[1] Half of the lower detection limit was used during calculation weighted geometric mean, median, and MAD for cases where element contents were below detection limit
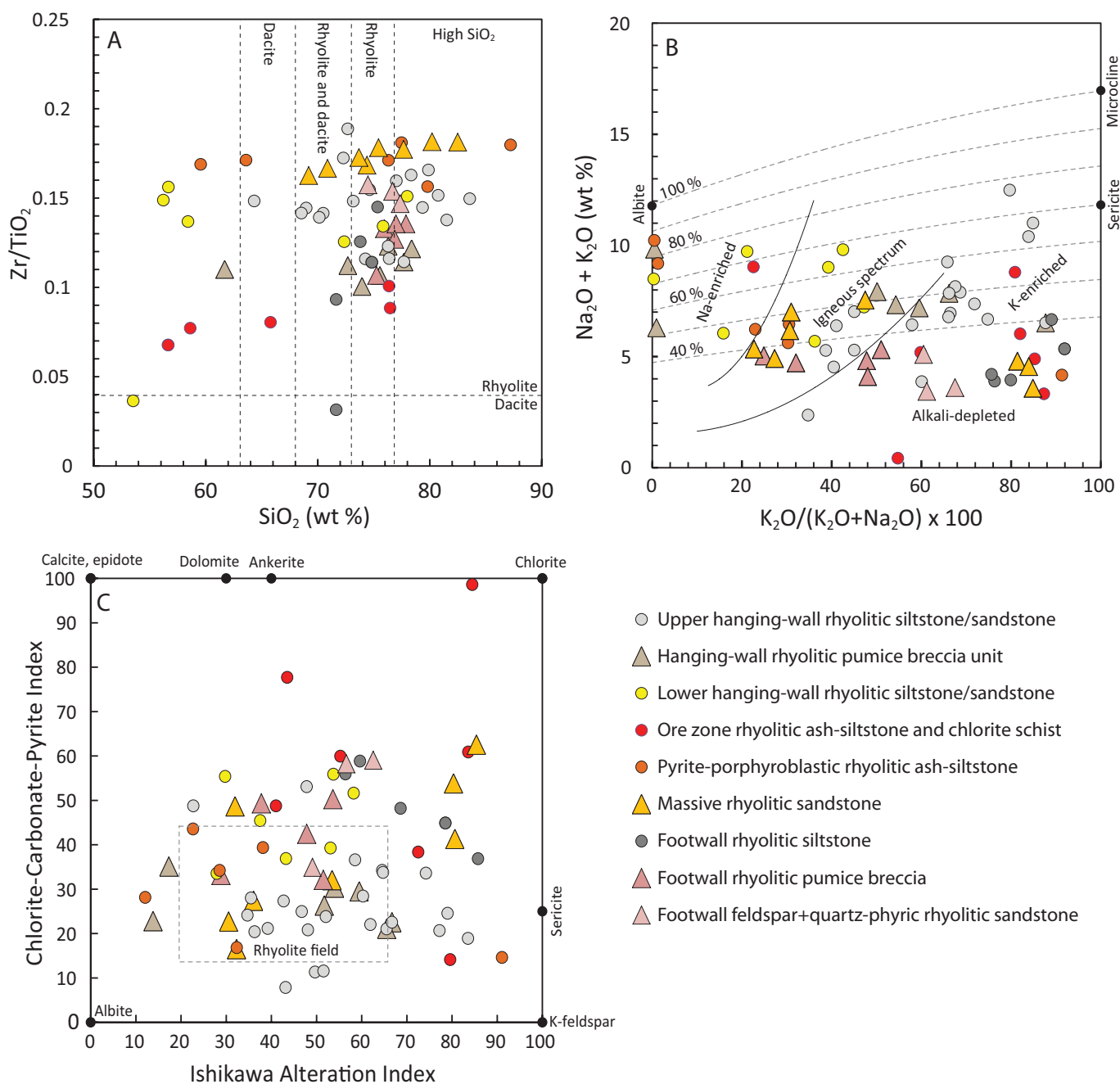
Fig. 13. A: Zr/TiO$_2$ vs. SiO$_2$ binary plot of volcaniclastic rocks from Lovisa. Compositional boundaries based on SiO$_2$ are from Le Bas et al. (1986). Rhyolite-dacite boundary based on Zr/TiO$_2$ is from Allen et al. (2003). Many samples have SiO$_2$ exceeding the 77 wt % maximum in Le Bas et al. (1986), reflecting silicification. B: Plot of K$_2$O + Na$_2$O vs. K$_2$O/(K$_2$O + Na$_2$O) of volcaniclastic rocks from Lovisa. The position of data points relative to the igneous spectrum of Hughes (1973) suggests substantial modifications of original alkali contents and ratios. Calculated theoretical lines for 40 to 100 wt % alkali feldspar are plotted for comparison. C: Alteration box plot of Large et al. (2001) showing Lovisa volcaniclastic rocks.

Sulfur isotopes

Sulfur isotope data from the Lovisa Fe formation and the Lovisa Zn-Pb deposit are shown in Table 4 and Figure 17. The lowest δ^{34}S values are for galena and sphalerite that occur disseminated in the Lovisa Fe formation (δ^{34}S = –6.1 to –1.9‰). Pyrite in a vein crosscutting a ductile fabric in semimassive magnetite gives a slightly higher value (δ^{34}S = 1.1).

Two analyses of pyrite porphyroblasts from the stratigraphic footwall of the Lovisa Zn-Pb deposit have higher δ^{34}S of 3.3 and 4.8‰. Pyrite from the sphalerite ore has similar values (δ^{34}S = 1.8–5.4‰), with the sphalerite having marginally higher δ^{34}S values than that in the Lovisa Fe formation (δ^{34}S = 1.4–4.7‰). Galena has the lowest δ^{34}S value (–0.9‰).

Fine-grained, yellow sphalerite in the laminated sphalerite facies of the main ore has lower δ^{34}S values of 1.0 to 1.5‰,
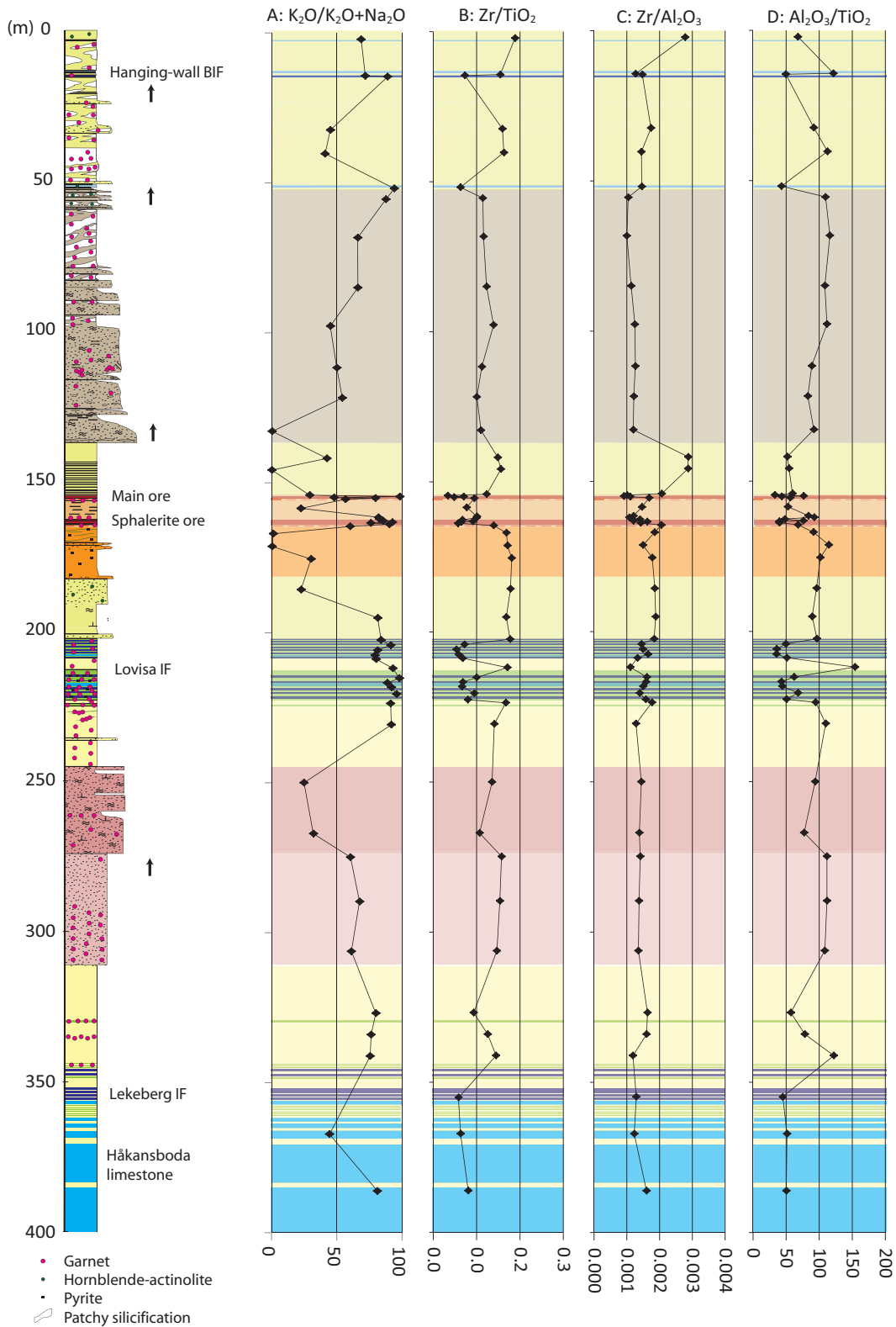
Fig. 14. Detailed chemostratigraphic column based mainly on Figure 6, with the same legend except for additional symbols explained at bottom. Ratios of alkali elements and immobile elements (Zr, Al_2O_3, TiO_2) plotted according to stratigraphic position, mainly utilizing data from drill holes 1501, 1502, and 1507. A: $K_2O/(K_2O + Na_2O)$. B: Zr/TiO_2. C: Zr/Al_2O_3. D: Al_2O_3/TiO_2. Note the marked variability of $K_2O/(K_2O + Na_2O)$ under constant immobile element ratios, the lesser immobile element variability in intervals of rhyolitic pumice breccia compared with rhyolitic ash-siltstone, and the generally lower Zr/TiO_2 and Al_2O_3/TiO_2 in intervals hosting limestone, magnetite, bedded calc-silicate rock, and sulfides. Abbreviations: BIF = banded iron formation, IF = iron formation.
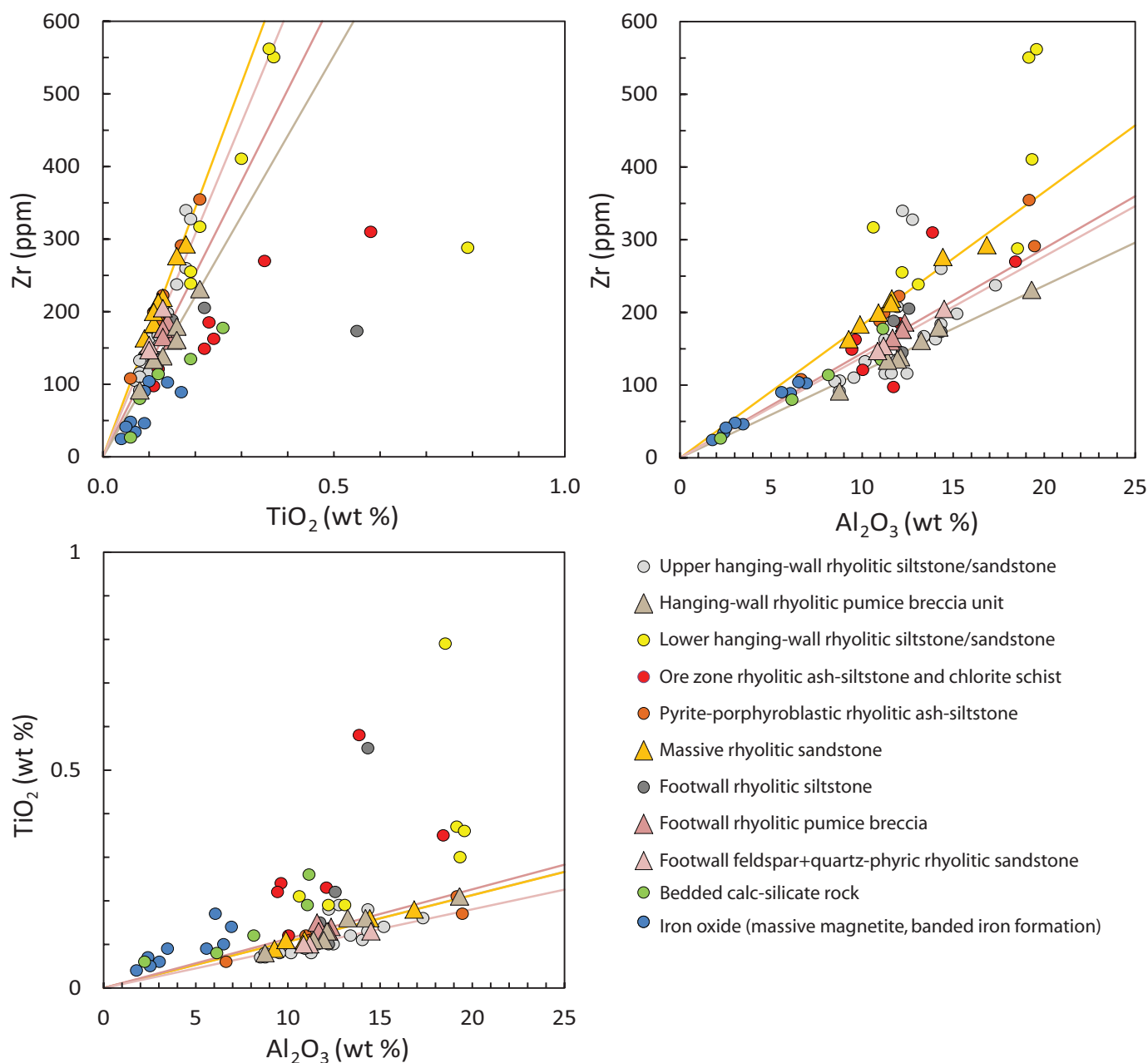
Fig. 15. Binary plots of A: Zr vs. TiO₂, B: Zr vs. Al₂O₃, and C: TiO₂ vs. Al₂O₃. Alteration lines are indicated for the units of rhyolitic pumice breccia and associated feldspar + quartzphyric rhyolitic sandstone. Most samples from the magnetite and Zn-Pb deposits are enriched in TiO₂ relative to Zr and Al₂O₃.

whereas coarser, paragenetically later red sphalerite has an even lower value of –0.2‰. The latter falls within the range of $\delta^{34}S$ values for sphalerite and galena from a directly adjacent vein (–1.3 to 0.5‰) and the ore with durchbewegung texture (–2.1 to 0.2‰).

A local zone of semimassive sphalerite and pyrite in the central shear on the western limb of the Lovisa anticline was sampled at the 73-m level of the mine and has $\delta^{34}S$ values of –2.8 and 0.0‰ respectively. Stratigraphic analysis suggests that this mineralization represents a highly sheared and attenuated equivalent of the ore zone on the eastern limb. Due to the high degree of deformation, this mineralization cannot be

placed into the detailed stratigraphic scheme of the eastern limb, so these data points are not shown in Figure 17.

In summary, the highest $\delta^{34}S$ values in the Lovisa deposit occur in the sphalerite ore. Slightly lower $\delta^{34}S$ values occur in the laminated sphalerite facies of the main ore, possibly indicating a general decrease in $\delta^{34}S$ stratigraphically upward in the Lovisa ore zone. Furthermore, isotopic compositions of sulfides from texturally and structurally late parts of the main ore (veins and ore with durchbewegung texture) have slightly lower $\delta^{34}S$, which also indicates a possible decrease in $\delta^{34}S$ with time, although the limited amount of samples and considerable overlap between them must be emphasized.

Table 4. Sulfur Isotope Analyses

Sample	Mineral	Setting	$\delta^{34}S$ (‰)
Main ore			
16061	Sphalerite	Coarse-grained sulfide vein	0.5
190 A SÖDER	Galena	Coarse-grained sulfide vein	–1.1
235 B NORR V	Galena	Coarse-grained sulfide vein	–1.3
LV 19	Galena	Coarse-grained sulfide vein	–1.0
LV 19	Sphalerite	Coarse-grained sulfide vein	0.3
16010	Galena-sphalerite	Fine-grained with durchbewegung texture	0.2
16079	Sphalerite	Fine-grained with durchbewegung texture	0.5
235 B NORR BO	Galena-sphalerite	Fine-grained with durchbewegung texture	–1.2
LKUL	Galena-sphalerite	Fine-grained with durchbewegung texture	–2.1
LKUL2	Galena-sphalerite	Fine-grained with durchbewegung texture	–2.0
16011	Sphalerite	Laminated sphalerite ore	1.0
235 B SY-red	Sphalerite	Laminated sphalerite ore	–0.2
235 B SY-yellow	Sphalerite	Laminated sphalerite ore	1.5
Sphalerite ore			
LV 11	Pyrite	Bedding-parallel trains in Fig. 11B	1.8
LV 2	Pyrite	Laminated sphalerite ore	5.4
LV 2	Sphalerite	Laminated sphalerite ore	4.7
16067	Sphalerite	Laminated sphalerite ore	2.8
16017	Pyrite	Laminated sphalerite ore	5.2
16017	Galena	Laminated sphalerite ore	–0.9
16017	Sphalerite	Laminated sphalerite ore	2.1
235 B NORR STRAT	Sphalerite	Laminated sphalerite ore	1.4
Pyrite-porphyroblastic red-pink rhyolitic siltstone-sandstone			
235 B NORR PY	Pyrite	Porphyroblastic	4.8
20150081	Pyrite	Porphyroblastic	3.3
Sheared ore zone equivalent on western limb of Lovisa antiform			
LV80N1	Pyrite	Semimassive pyrite	0.0
LV80N3	Sphalerite	Disseminated	–2.8
Lovisa iron formation (lower part)			
16090	Pyrite	Vein in magnetite	1.1
16089-90	Galena	Disseminated in massive magnetite	–1.9
16023	Sphalerite	Disseminated in massive magnetite	–4.9
16023	Galena	Disseminated in massive magnetite	–5.7
20160072	Galena	Disseminated in massive magnetite	–6.1

Lead isotopes

Six galena samples representing three different ore types were analyzed. Two samples from the Lovisa Fe formation and two from vein mineralization of the Lovisa main ore have Pb isotope compositions that are identical within analytical uncertainty; $^{206}Pb/^{204}Pb$ is between 15.738 and 17.742; $^{207}Pb/^{204}Pb$ = 15.364 to 15.368, and $^{208}Pb/^{204}Pb$ = 35.262 to 35.275 (Table 5). One of the samples of ore with durchbewegung texture (LKUL) shares this isotopic composition that is consistent with the uniform Pb isotope composition shown by most metallic 1.89 Ga mineral deposits in Bergslagen (e.g., Jonsson and Billström, 2009). However, another sample of ore with durchbewegung texture (235B KUL N) is slightly more radiogenic: $^{206}Pb/^{204}Pb$ = 15.798, $^{207}Pb/^{204}Pb$ = 15.369, and $^{208}Pb/^{204}Pb$ = 35.284. The Pb isotope values are virtually identical to the Pb isotope values reported by Romer and Wright (1993) for galena in the Guldsmedshyttan Pb-Ag deposit. However, Romer and Wright (1993) obtained considerably more heterogeneous values involving more radiogenic Pb from chalcopyrite, sphalerite, and glaucodot ([Co,Fe]AsS) from the Håkansboda Cu deposit northeast of Lovisa (Fig. 3).

Discussion

Structural evolution

The structural relationships at Lovisa are consistent with Carlon and Bleeker's (1988) model for an F_1-F_2 fold interference pattern. The pre-S_1 foliation defined by altered and compacted former pumice clasts is interpreted as a diagenetic compaction foliation, and no tectonic structures related to this foliation have been observed.

The Engvall fault crosscuts the F_1-F_2 fold interference pattern, so it is most likely a post-F_2 structure, despite being subparallel to the axial surface of the Guldsmedshyttan syncline. The dolerite dike at Lovisa shows no ductile fabric and cuts the Engvall fault at an oblique angle. Where the dike and fault intersect, the dike follows the fault trace for about 1 km, suggesting that the dike is younger and intruded along the fault. Clay gouge along the margins of the dike implies fault movement after dike emplacement at ca. 0.98 to 0.95 Ga, thus indicating multiple phases of movement.

The relict laminated sphalerite facies at the margins of the main ore suggests that the ore with durchbewegung texture
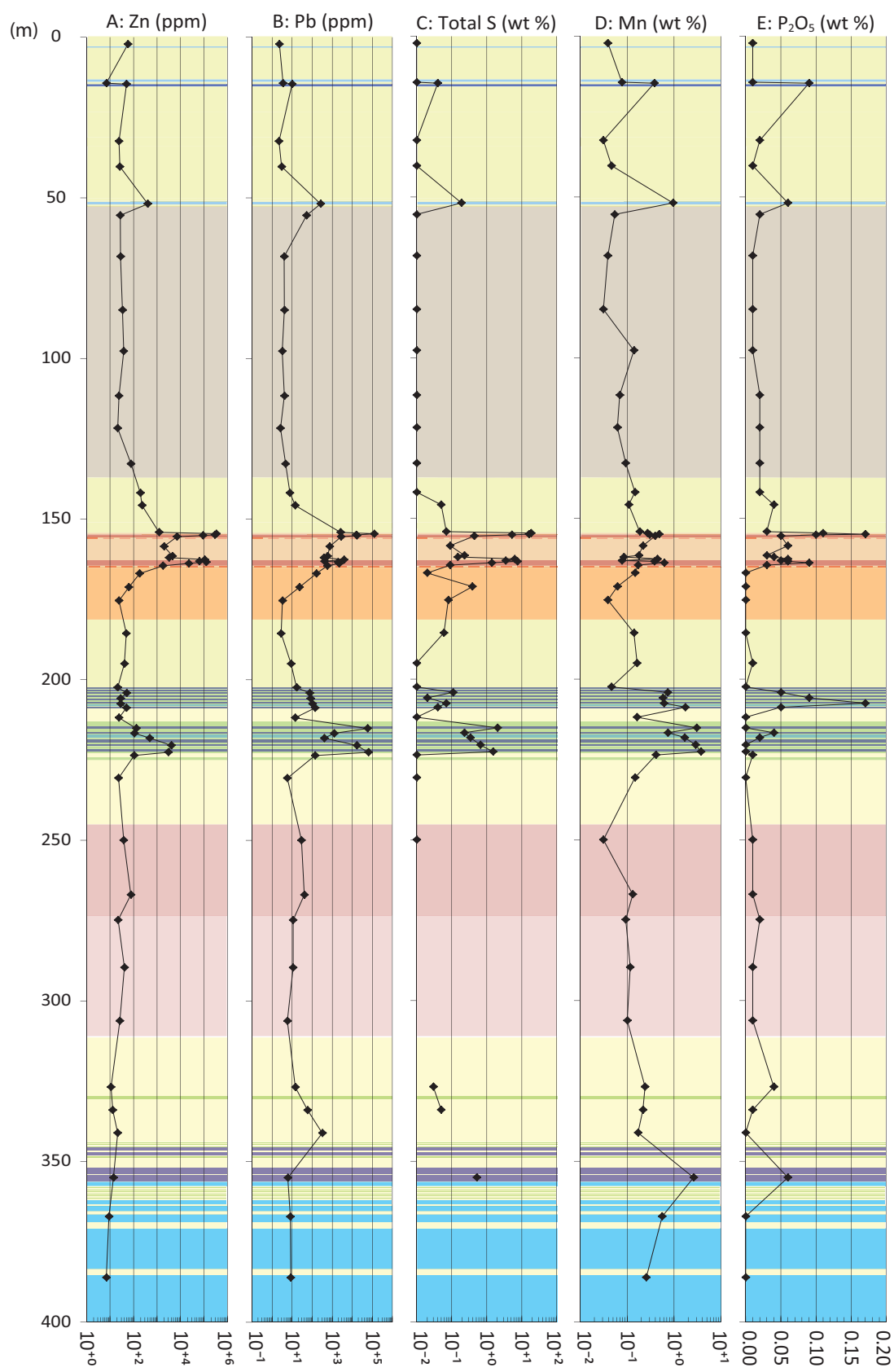
Fig. 16. Detailed chemostratigraphic column mainly based on Figure 6. Data mainly are from analyses of drill core samples. A: Zn. B: Pb. C: Total S. D: Mn. E: P_2O_5. F: V. G: Ba. H: B. I: Co. J: Cu. In C, total S has a 0.02 wt % detection limit plotted as 0.01 wt %. In H, B has a 10-ppm detection limit plotted as 5.
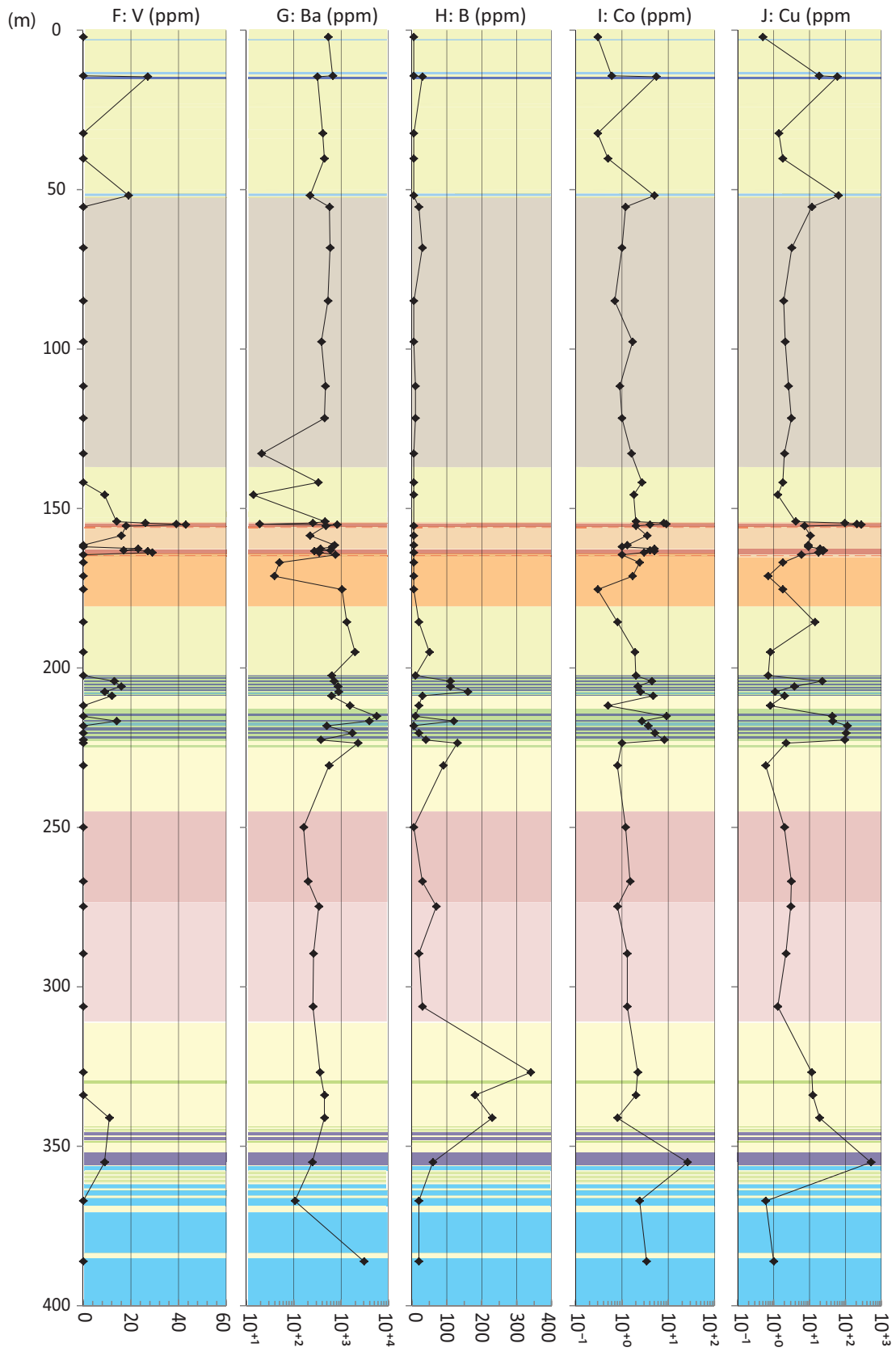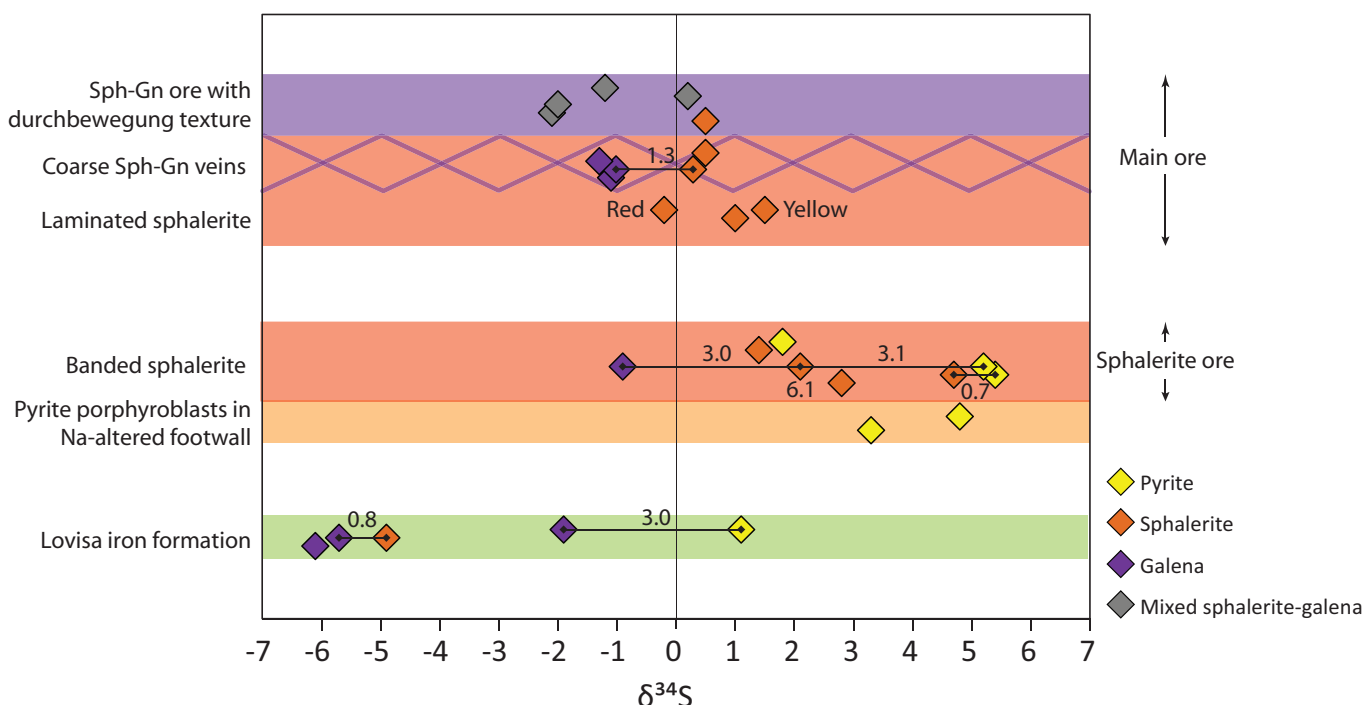
Fig. 16. *(Cont.)*

Fig. 17. $\delta^{34}S$ for sulfides from the eastern limb of the Lovisa antiform, grouped according to stratigraphic position (not to scale) and style of mineralization. Tie lines indicate sulfides from the same samples, with calculated Δ ($\delta^{34}S_a$-$\delta^{34}S_b$) shown. Note general increasing $\delta^{34}S$ in sulfides up to the position of the sphalerite ore, followed by a decrease to 0‰ in the main ore. Abbreviations: Gn = galena, Sph = sphalerite.

developed by deformation of a preexisting sulfide bed rather than by injection of sulfides remobilized from elsewhere. This is also consistent with the Pb isotope ratios that are similar to those of most 1.89 Ga sulfide deposits in the Bergslagen district (cf. Romer and Wright, 1993; Sundblad, 1994; Jonsson and Billström, 2009). However, the slightly more radiogenic sample 235B KUL N plots along the trend for more evolved Svecofennian Pb observed in western Bergslagen by Jonsson and Billström (2009) and may indicate an addition of secondary Pb in conjunction with formation of the durchbewegung texture.

A higher initial galena content in the main ore relative to the sphalerite ore could explain why the durchbewegung texture developed mainly in the former. This is due to the refractory strength of sphalerite and pyrite, which is higher than that of galena (e.g., Marshall and Gilligan, 1987), whereby an originally more galena-rich bed would have been more favorable for partitioning strain.

It is clear from crosscutting relationships that the durchbewegung texture developed prior to the last offsets along the central shear, the Lovisa fault, and the Engvall fault (Fig. 11F). This is exemplified by minor drag folding of the ore with durchbewegung texture against the central shear. Furthermore, there is no relationship between the intensity of strain in the main ore and proximity to the central shear, since the main ore and shear zones can be separated by relatively well preserved laminated sphalerite ore (Fig. 11F). A young age for the central shear is further suggested by the fact that it crosscuts shallow-dipping pegmatite veins, which cross S_1 at a high angle.

Thus, we interpret the durchbewegung texture to have formed along the eastern limb of the Lovisa anticline late during D_1 at ca. 1.87 to 1.85 Ga, when strain was partitioned to the most incompetent bed in the succession. The adjacent vein facies may have formed either as piercement veins peripheral to this bed in conjunction with shearing or by later remobilization at the transition to more brittle deformation. The observed offsets of the main ore across the central shear may have similarly resulted from later reactivation of the same structure under more brittle conditions.

Table 5. Lead Isotope Ratios

Sample	Mineral	Facies	Unit	$^{206}Pb/^{204}Pb$	$^{207}Pb/^{204}Pb$	$^{208}Pb/^{204}Pb$
LK20160072	Galena	Galena dissemination	Lovisa IF	15.742	15.366	35.268
16023	Galena	Galena dissemination	Lovisa IF	15.743	15.368	35.275
LV19 GN	Galena	Sphalerite-galena vein	Main ore	15.742	15.364	35.264
235TÄRN	Galena	Sphalerite-galena vein	Main ore	15.738	15.364	35.262
LKUL	Mixed sphalerite-galena	Sphalerite-galena ore with durchbewegung texture	Main ore	15.734	15.362	35.255
235B KUL N	Mixed sphalerite-galena	Sphalerite-galena ore with durchbewegung texture	Main ore	15.798	15.369	35.284

Abbreviations: IF = iron formation

Stratigraphic evolution

Deposition of massive to planar, stratified rhyolitic ash-siltstone followed formation of the Håkansboda limestone. Allen et al. (1996, 2003) interpreted the rhyolitic ash-silt-stone facies in Bergslagen to be reworked pyroclastic ash, deposited below storm wave-base by dilute turbidity currents and suspension settling, distal to the source volcanoes. The common planar stratification and normal grading at Lovisa are consistent with this interpretation. The presence of this facies indicates that broadly contemporaneous, explosive felsic volcanism occurred somewhere in the Bergslagen district (cf. Allen et al., 1996).

The Lovisa Fe formation and the Lovisa stratiform Zn-Pb ore are sandwiched between two compositionally distinct intervals of coarser-grained, rhyolitic, pyroclastic debris (Fig. 6). These deposits record discrete felsic volcanic events that punctuate the ambient sedimentation of rhyolitic ash-siltstone in the basin (cf. Allen et al., 1996).

The low Zr/TiO_2 and Al_2O_3/TiO_2 in the intervals hosting sulfide mineralization are anomalous relative to volcaniclastic rocks in the succession (Figs. 14, 15). The same geochemical anomalies in Zr/TiO_2 and Al_2O_3/TiO_2 are evident in the Fe formations and limestone, that is, in other units formed at times when the sedimentation rate of rhyolitic ash was low (Fig. 14).

The lower values of Zr/TiO_2 could be caused by the ash component attaining a more intermediate composition, cosettling of rhyolitic ash with mafic or intermediate ash, or cosettling of rhyolitic ash and marine clays. The Sc/Th ratio in the stratiform Zn-Pb mineralization is mostly consistent with a clay component (Fig. 18; cf. McLennan et al., 1993). This would imply that chemical, biogenic, and hydrothermal sediments, including sulfide mineralization, could only accumulate when the basin was relatively starved of volcaniclastic sedimentation, i.e., when the fine-grained detrital component became more enriched in Al and Ti (Fig. 18).

Based on the pattern in the Zr/TiO_2 vs. Sc/Th plot (Fig. 18), two samples of massive magnetite and associated bedded calc-silicate rock from the Lovisa Fe formation display Sc/Th greatly exceeding that which can be explained by cosettling with a normal clay component, thus indicating a possible presence of mafic to intermediate volcaniclastic material.

Genesis of the Fe formations

Except for the thin calcite BIF in the hanging wall of the Lovisa Zn-Pb deposit, all Fe formations above the Håkansboda lime-stone belong to the Mn-rich subtype of Fe oxide deposits in Bergslagen. On a plot of Fe/Ti vs. Al/(Al + Fe + Mn), samples define a trend between Fe oxide deposits and associated calc-silicate rocks on one end and the volcaniclastic rocks on the other end (Fig. 19A). This implies that the precursors of the bedded magnetite- and calc-silicate-rich rocks are mixtures of detrital volcaniclastic/sedimentary material and a hydrothermal Fe (and Mn) component and that increasing Al/(Al + Fe + Mn) suggests an increasing detrital component (cf. Peter et al., 2003). However, presence of a sedimentary carbonate component can also be inferred based on the calc-silicate
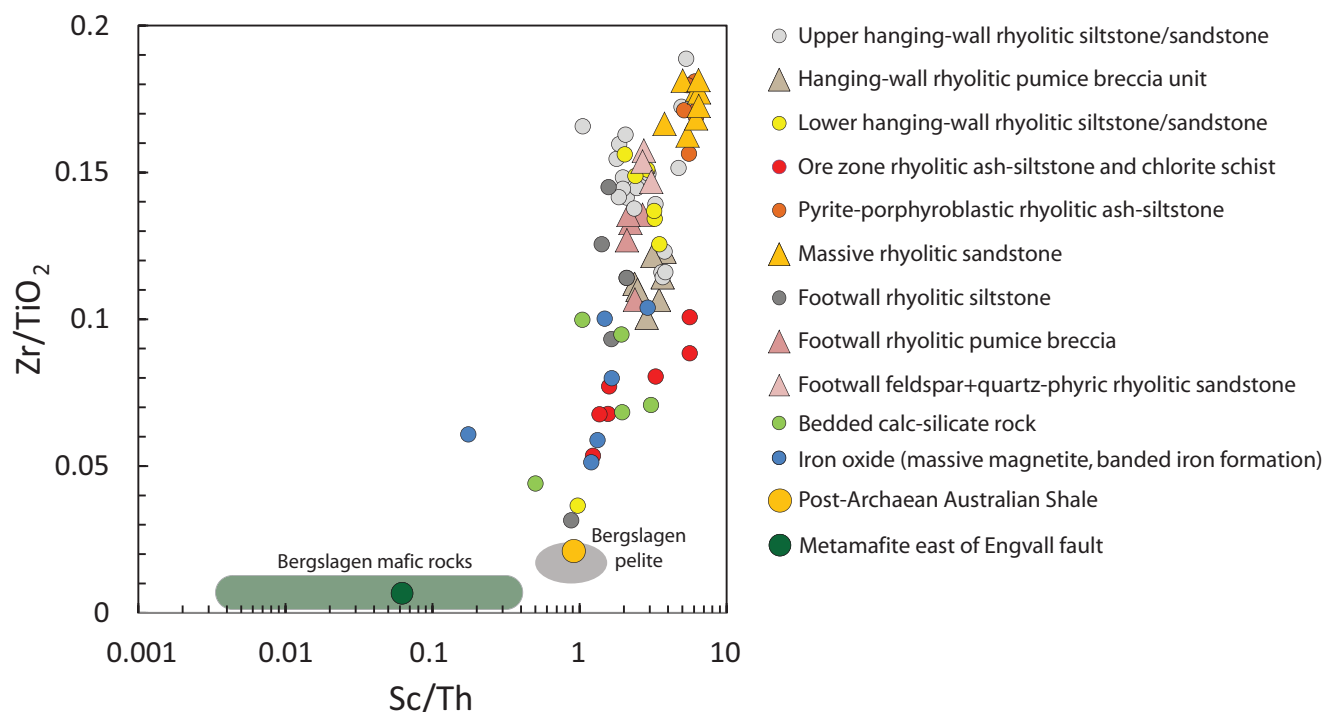
Fig. 18. Zr/TiO_2 vs. Sc/Th plot. Most samples from the stratiform Zn-Pb sulfide ore zone plot in the area between the Lovisa-agruvan volcaniclastic rocks and pelitic rocks. This is consistent with these rocks containing a mixture of rhyolitic ash and a terrigenous clay component, although a contribution from mafic volcaniclastic material cannot be ruled out. Two samples from the Lovisa Fe formation, however, have Sc/Th lower than normal pelitic rocks, implying a contribution from more mafic-intermediate volcaniclastic material. Bergslagen mafic rocks based on data in Johansson and Hålenius (2013), Bergslagen pelite based on data in Jansson et al. (2017), N. Jansson (unpub. data, 2017), and Post-Archean Australian Shale values from Taylor and MacLennan (1985).
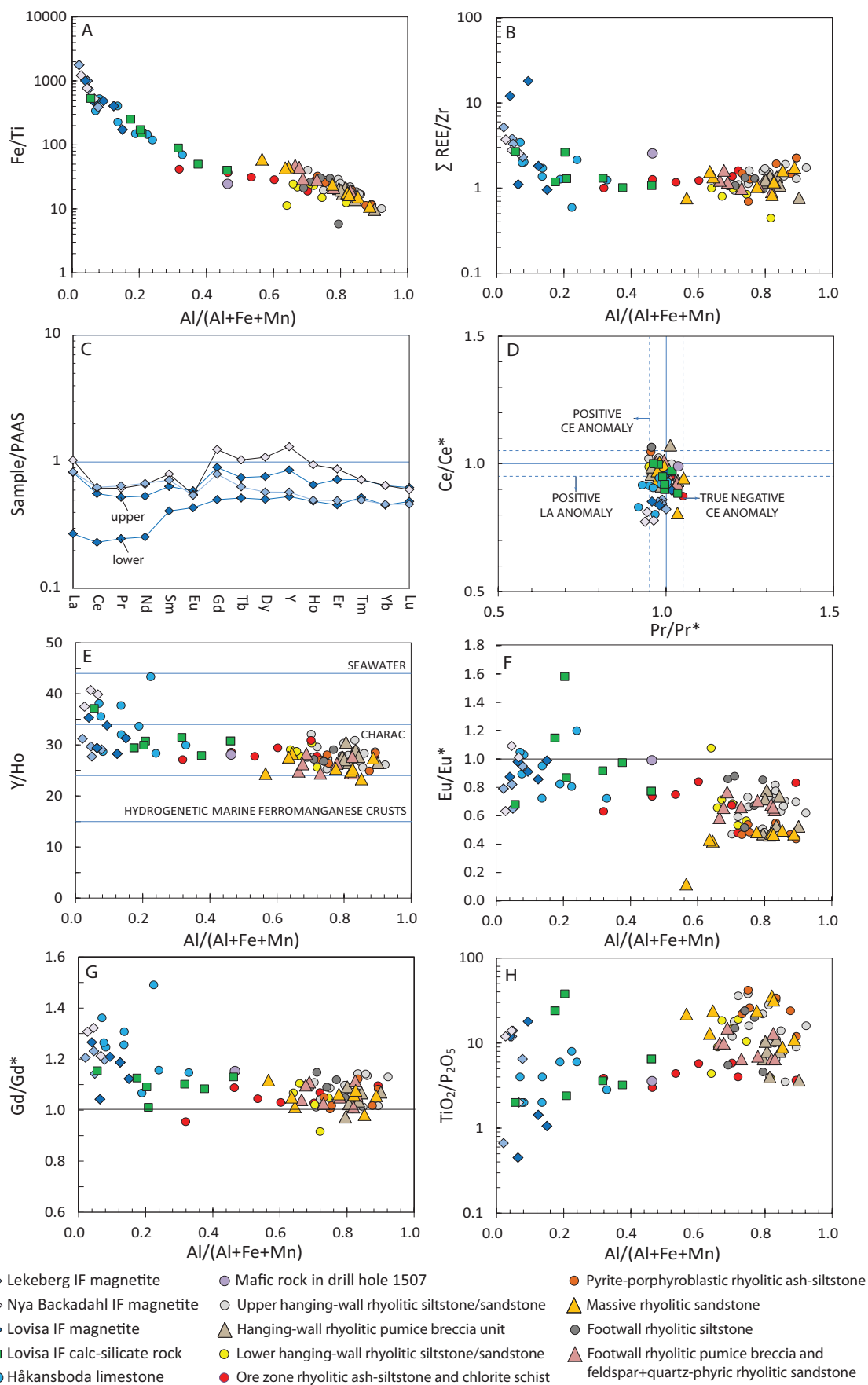
mineralogy and minor interbedded carbonate in, e.g., the Lovisa Fe formation. This complicates interpretation, since carbonates and Fe-bearing minerals cause similar shifts on the mixing line (Fig. 19A).

Shale-normalized rare earth element (REE) data can yield substantial information on the genesis of Fe formations. However, the REE pattern reflects a mixture of detrital and hydrothermal material in varying proportion, and the REE pattern of samples with a low hydrothermal component will be dominated by that of the detrital component (Peter et al., 2003; Bekker et al., 2010; Jansson and Allen, 2011). The Fe formations in the Lovisa area have Al_2O_3 contents of 2.34 to 6.94 wt %, whereby they invariably contain a detrital volcaniclastic or pelitic sedimentary component.

Exchanging Fe/Ti for $\Sigma REE/Zr$ shows that the hydrothermal component in the lower Lovisa Fe formation must contain REEs, since $\Sigma REE/Zr$ in the Lovisa Fe formation increases with decreasing Al/(Al + Fe + Mn) to levels that cannot be explained by admixture with carbonates (Fig. 19B). Sample LK20160072 has the lowest measured Al_2O_3 content (3.03 wt %) in the Lovisa Fe formation and should best reflect the REE signature of the hydrothermal end member. Normalization of data to Post-Archean Australian Shale (PAAS) yields an irregular pattern in which the main features are enrichment in La and Gd-Y, positive Gd and Y anomalies, and a negative Eu anomaly (Fig. 19C). Using the same approach, the Nya Backadahl Fe formation displays a broadly similar pattern, supporting the correlation (Fig. 19C). The Lekeberg sample is similar in behavior of La and Gd to that in the REE profile, yet differs in a less distinct positive Y anomaly (Fig. 19C). The discrimination of the positive La anomaly from a negative Ce anomaly is achieved by plotting the samples in the Ce/Ce* vs. Pr/Pr* plot of Bau and Dulski (1996), which suggests that no true Ce anomalies are present (Fig. 19D).

Even the samples with lowest Al/(Al + Fe + Mn) contain a detrital component, which impacts the pattern of the normalized REE data. A mass-balance calculation to isolate the hydrothermal component cannot be done, since it would require a homogeneous composition of the detrital component that is identical to that of adjacent detrital rocks. This is not supported by immobile element data (Fig. 14A-C). The nature of the hydrothermal component can, however, be further evaluated qualitatively by using the mixing relationship outlined in Figure 16A and B. This approach reveals that Y/Ho shifts from the charge and radius controlled (CHARAC) field toward suprachondritic values (Y/Ho > 27.7; Bau, 1996)

with decreasing Al/(Al + Fe + Mn), approaching the Y/Ho ratio of modern seawater (Fig. 19E). The Y/Ho values of the Fe formations are considerably higher than those of hydrogenetic marine ferromanganese crusts (cf. Bau, 1996). A similar, albeit more scattered, trend is observed for Eu/Eu*, yet the majority of the samples project toward Eu/Eu* between 0.8 ± 0.2 with decreasing Al/(Al + Fe + Mn). Thus, positive Eu anomalies are mainly lacking in the hydrothermal end-member component (Fig. 19F). A similar trend is observed for Gd/Gd*, with most Fe oxide samples projecting toward an end member Gd/Gd* =1.3 ± 0.1 (Fig. 19G). Samples of carbonate rock yield consistently higher Gd/Gd* for a given value of Al/(Al + Fe + Mn).

Given the elevated P content of the Fe formations and the Lovisa Zn-Pb deposit relative to adjacent rocks, it is likely that a considerable fraction of the REEs in these intervals are hosted by apatite. The high P in the Fe oxide deposits (up to 0.2 wt % P_2O_5) and the Lovisa Zn-Pb deposit (0.02–0.07 wt % P_2O_5) can be further evaluated by plotting TiO_2/P_2O_5 vs. Al/(Al + Fe + Mn). In the case where the elevated P content reflects presence of a mafic detrital component, the TiO_2/P_2O_5 should not be lower than that in an end-member mafic volcanic rock. This is the case for the Lovisa Zn-Pb deposit, whereas in the Lovisa Fe formation anomalously low TiO_2/P_2O_5 suggests that P_2O_5 must be derived from a nondetrital component (Fig. 19H). Phosphorous in seawater is typically scavenged by ferric oxyhydroxides suspended in the water column (e.g., Peter, 2003).

The stratiform Fe formations of the Lovisa area differ from other Mn-rich Fe formations with associated base metal sulfide mineralization in Bergslagen in the presence of positive Gd anomalies and the lack of positive Eu anomalies (cf. Jansson, 2011; Jansson et al., 2013). The fact that the Fe formations are otherwise compositionally similar and were analyzed by the same lab using the same methods argues against the REE anomalies at Lovisa being analytical artifacts.

Distinct positive Eu anomalies in the Stollberg ore field in Bergslagen (Fig. 1) were attributed to discharge into seawater of hot (>250°C) slightly to moderately acidic hydrothermal fluids carrying Eu^{2+} in solution (Jansson et al., 2013). The absence of positive Eu anomalies indicates the Lovisa Fe formations were precipitated from low-temperature (<250°C) fluids (e.g., Bau and Dulski, 1996; Peter, 2003). However, a hydrothermal origin is indicated by the positive Y anomalies, which, along with the absence of positive Ce anomalies, distinguish them from modern marine hydrogenetic

Fig. 19. Geochemical plots of Fe formations (IF) and associated calc-silicate rocks. A: Fe/Ti vs. Al/(Al + Fe + Mn) plot (Boström, 1973), with samples defining a mixing line between metavolcanic rocks and Fe oxide mineralization. Note that marble samples plot along the same line. B: $\Sigma REE/Zr$ vs. Al/(Al + Fe + Mn). C: REE data normalized to Post-Archean Australian Shale (PAAS) (Taylor and MacLennan, 1985) for the samples with lowest Al/(Al + Fe + Mn) from the Lekeberg, Nya Backadahl, and Lovisa Fe formations. The REE distribution differs somewhat in the lower and upper part of the Lovisa Fe formation, therefore two samples are shown. D: Plot of Ce/Ce*$_{PAAS}$ vs. Pr/Pr*$_{PAAS}$, illustrating absence of true negative Ce anomalies in Fe formations from the Lovisa area. The pattern is more consistent with positive La anomalies. Ce/Ce*$_{PAAS}$ = $Ce_N/(La_N \times Pr_N)^{0.5}$, Pr/Pr*$_{PAAS}$ = $Pr_N/(La_N \times Nd_N)^{0.5}$, modified after Bekker et al., 2010. E: Y/Ho vs. Al/(Al + Fe + Mn), illustrating that Y/Ho increases with decreasing volcaniclastic component. The ranges for seawater, change and radius controlled (CHARAC), and hydrogenetic marine ferromanganese crusts are from Bau (1996). F: Eu/Eu*$_{PAAS}$ vs. Al/(Al + Fe + Mn), illustrating the poor development of positive Eu anomalies, even in samples poor in detritus. Due to presence of Gd anomalies, Eu/Eu* was calculated as $Eu_N/(0.67Sm_N + 0.33Tb_N)$ (cf. Bau and Dulski, 1996). G: Gd/Gd*$_{PAAS}$ vs. Al/(Al + Fe + Mn), illustrating presence of positive Gd anomalies in the hydrothermal end member. Gd/Gd*$_{PAAS}$ = $Gd_N/(0.33Sm_N + 0.67Tb_N)$. H: TiO_2/P_2O_5 vs. Al/(Al + Fe + Mn).

ferromanganese crusts that form in oxidized sea floor environments (Fig. 19C) but are similar to hydrothermal ferromanganese precipitates (Bau and Dulski, 1996). Bau and Dulski (1996) argued that the negative Y anomaly in hydrogenetic marine ferromanganese crusts is due to slow growth rate, resulting in REEs and Y in equilibration with seawater. In contrast, rapidly precipitated hydrothermal ferromanganese precipitates indiscriminately scavenge REEs and Y from seawater too quickly to allow exchange equilibration between dissolved and adsorbed REEs and Y.

Positive La and Gd anomalies have been documented in modern seawater (De Baar et al., 1985; Bau and Dulski, 1996; Alibo and Nozaki, 1999), late Archean-early Proterozoic Fe formations (Bau and Dulski, 1996), phosphorites (Emsbo et al., 2015), and hydrogenous fluorapatite proximal to SEDEX Pb-Zn mineralization (Gadd et al., 2016). According to Bau (1999), fractionation of La, Gd, and Y is not redox controlled but related to the lanthanide tetrad effect. Experiments by Bau (1999) suggest that scavenging of La, Gd, and Y from a solution upon interaction with Fe oxyhydroxides is strongly pH dependent. At low pH, Y was found to become enriched in the solution, whereas at pH >5, fractionation was observed to also cause enrichment of La and Gd in the solution. Thus, the positive La, Gd, and Y anomalies in Fe formations in the Lovisa area could reflect deposition from a near-neutral hydrothermal fluid that had already interacted with Fe oxides along the fluid path (for example, hematite-quartz BIF in the stratigraphic footwall).

Ferric oxyhydroxides, ferrihydrite, green rust, Fe carbonates, and Fe silicates are recognized as likely precursors of magnetite and hematite in Precambrian Fe formations, depending on, e.g., the pH and f_{O_2} of the depositional environment (cf. Peter, 2003; Bekker et al., 2010; Halevy et al., 2017). Whereas hematite is commonly observed as the paragenetically oldest Fe mineral in BIFs stratigraphically beneath the Håkansboda limestone (e.g., Stråssa, Blanka, and Stripa; Geijer, 1927; Geijer and Magnusson, 1944), there is no evidence of former hematite in the Fe formations stratigraphically between the Håkansboda limestone and the Lovisa Zn-Pb deposit. The greater abundance of Fe^{2+}-bearing minerals in the latter group of Fe formations is attributed to primary differences and could reflect (1) presence of organic matter, which could drive diagenetic or metamorphic reduction of precursor ferric oxyhydroxides or ferrihydrite, (2) presence of both ferrous (e.g., siderite, silicates) and ferric precursor minerals, or (3) primary mixed Fe^{2+}-Fe^{3+} precursors, such as green rust.

The first alternative finds support from the local presence of accessory graphite in the magnetite Fe formations and interbedding with graphitic mudstone at Nya Backadahl. However, assuming graphite derivation from organic matter, oxygen-deficient conditions would have been necessary on the sea floor, since the low deposition rate of detrital sediment in these intervals would not be favorable for preservation of organic matter by burial. Occurrence of carbonates and Fe silicates is a more attractive alternative, since these could react with silicates to form calc-silicates during metamorphism (cf. Klein 1973; Jansson and Allen, 2011). French (1970) has furthermore shown that in the absence of quartz, siderite undergoes thermal decomposition to magnetite ±

graphite at temperatures exceeding 400° to 450°C, which is lower than the metamorphic grade at Lovisa. Green rust forms by reduction of ferrihydrite and can alter to magnetite, even when still suspended in an anoxic water column (Zegeye et al., 2012). Along with the absence of Ce anomalies, these considerations are most consistent with the precursors to the Fe formations having accumulated in a suboxic to anoxic depositional environment, more reducing than for the hematite-rich BIFs stratigraphically below.

Genesis of the sulfide deposits

We interpret the Lovisa Zn-Pb deposit to be a metamorphosed, stratiform syngenetic-exhalative deposit (laminated mineralization) that has been locally tectonically remobilized (ore with durchbewegung texture and veins). The calc-silicate–poor nature of the deposit contrasts with limestone- and skarn-hosted sulfide deposits in Bergslagen, where massive skarns are commonly abundant and where metasomatic skarn models have been discussed (e.g., Ryllshyttan; Jansson and Allen, 2015). Although garnet compositions in the Lovisa Zn-Pb deposit overlap with those of Zn skarns (cf. Meinert et al., 2005), we emphasize the highly subordinate calc-silicate content in the ore zone and the porphyroblastic texture of garnet, which is similar to that in metamorphic rocks. As in other stratiform deposits in Bergslagen (e.g., Zinkgruvan), we find that the mineralogy and textures can be explained by regional metamorphism of preexisting hybrid rock types containing a variable content of quartz, feldspars, phyllosilicates, Fe oxides, and carbonates (cf. Hedström et al., 1989; Jansson and Allen, 2011; Jansson et al., 2013, 2017).

No obvious feeder zone has been recognized near the Lovisa Zn-Pb deposit, which may indicate that it is distal to a hydrothermal vent. This is consistent with the conclusions of Carlon and Bleeker (1988), who suggested that the Håkansboda Cu-Co deposit ca. 1,500 m northeast of Lovisa (Fig. 3) formed in a vent to stratiform mineralization in the area.

A syngenetic-exhalative origin followed by regional metamorphism is likewise favored for the Pb-Ag mineralization in the Lovisa Fe formation based on (1) absence of Zn and Pb outside the Fe formation, (2) the affinity of the Pb-Ag mineralization to a specific Fe formation over a strike extent of several kilometers, (3) presence of sphalerite-galena laminae in graphitic mudstone at the correlative Nya Backadahl Fe formation, and (4) the asymmetric vertical zonation of Zn and Pb within this unit (e.g., Fig. 16A, B). The vertical zonation is consistent with the accumulation of base metal sulfides during the onset of Fe formation deposition but diminishing with time.

Source of Sulfur

Most studies of S isotope compositions of syngenetic, polymetallic sulfide deposits in Bergslagen have reported relatively narrow $\delta^{34}S$ ranges: for example, at Hällefors ($\delta^{34}S$ = –0.6 to 2.7‰; Wagner et al., 2005), Gruvåsen ($\delta^{34}S$ = –1.4 to 1.5‰; Hellingwerf and van Raaphorst, 1988), Falun ($\delta^{34}S$ = –2.3 to –0.2‰; Gavelin et al., 1960), and Svärdsjö ($\delta^{34}S$ = –4.0 to 3.0‰; Billström, 1991). These examples, along with average $\delta^{34}S$ values close to 0‰, led Wagner et al. (2005) to conclude that the majority of these deposits contain S leached from volcanic rocks with or without a direct magmatic-hydrothermal

input, whereas S sourced from reduction of seawater SO_4^{2-} was minor. By implication, isotopic fractionation during leaching, transport, and sulfide deposition was minimal.

Values of $\delta^{34}S$ for sulfides from Lovisa similarly cluster close to 0‰, yet the $\delta^{34}S$ range of the Lovisa Zn-Pb deposit ($\delta^{34}S$ = –2.8 to 5.4‰) is larger than the examples given above, particularly if the sulfides in the Lovisa Fe formation are included ($\delta^{34}S$ = –6.1 to 5.4‰). It is uncertain whether the sulfides in the Lovisa Fe formation are genetically related to the Lovisa Zn-Pb deposit. However, the stratigraphic proximity of these two deposits and the similar Pb isotope values support this interpretation. Nevertheless, the relatively wide range in $\delta^{34}S$ and the stratigraphic variations in $\delta^{34}S$ over short distances contraindicate the model of Wagner et al. (2005), which does not account for all aspects of the $\delta^{34}S$ patterns at Lovisa. Instead, mixing of S sourced from different reservoirs (e.g., leached from volcanic rocks and from seawater) or variable degrees of isotopic fractionation of S derived from a single volcanic or seawater S reservoir must be considered.

Billström (1991) reported $\delta^{34}S$ to range from –6.5 to 16.5‰ at the Zinkgruvan stratiform Zn-Pb-Ag deposit based on 260 separates of sphalerite, galena, and Fe sulfides. However, the data yield an average of 2.0‰, and 75% of the data yielded $\delta^{34}S$ between –3.0 and 3.0‰. Jansson et al. (2017) suggested that Zinkgruvan formed upon venting of oxidized (SO_4^{2-} > H_2S), metalliferous brines at a near-neutral pH into a reduced brine pool. The source of S at Zinkgruvan was interpreted as a mixture of S leached from volcanic rocks ($\delta^{34}S \approx 0$‰) and H_2S derived from abiotic or bacterial sulfate reduction of contemporaneous seawater SO_4^{2-} ($\delta^{34}S \approx 17$‰). This model for the source of S for the Zinkgruvan deposit is attractive for Lovisa, because in order for the ore-forming fluid to transport metals and H_2S together, the fluid must have been acidic to transport Zn and Pb in solution efficiently (cf. Cooke et al., 2000). It would then be difficult to explain how the ascending hydrothermal fluid could traverse the Håkansboda limestone without losing most of its base metal content upon neutralization (cf. Jansson et al., 2017). Neutralization of hot, acidic hydrothermal fluids carrying metals and H_2S together has been demonstrated as a highly efficient mechanism for forming massive, stratabound limestone-and skarn-hosted polymetallic sulfide deposits elsewhere in Bergslagen, such as at Stollberg (Jansson et al., 2013) and Falun (Kampmann et al., 2017).

Availability of Sulfur and Sources of Sulfur

Sulfide deposition from fluids or in an environment that was H_2S deficient is suggested by the generally Fe sulfide poor nature of stratiform sulfide mineralization at Lovisa, locally approaching monomineralic compositions (cf. Ohmoto and Goldhaber, 1997). A similar conclusion was made by Jansson et al. (2017) for the Zinkgruvan deposit. The bulk of the contained S in these deposits is hosted by Fe-poor sphalerite and galena, and consequently whole-rock total S is essentially a function of sphalerite and galena content (Fig. 20). In contrast, the Falun and Stollberg stratabound limestone- and skarn-hosted deposits contain significant pyrite (Falun) and/or pyrrhotite (Stollberg), such that these deposits are more S rich at a given base metal content (Fig. 20). Since a large part of the mineralization at Stollberg is hosted by Fe-rich rocks

including magnetite Fe formation (Jansson et al., 2013), these differences in the Fe sulfide/base metal sulfide content cannot be attributed to variable Fe contents in the deposits.

Under H_2S-deficient conditions, precipitation of galena or sphalerite may essentially buffer H_2S and redox to below levels needed to precipitate Fe sulfides, potentially forming monomineralic sulfide assemblages (Ohmoto and Goldhaber, 1997; Labrenz et al., 2000). Such processes may also fractionate $\delta^{34}S$ since, for example, Pb preferentially combines with ^{32}S (Ohmoto and Goldhaber, 1997; Seal II, 2006).

Thus, aside from differences in the characteristics of exhaled hydrothermal fluids (e.g., T, metal contents) at different times, some of the variation in metal ratios and $\delta^{34}S$ could reflect variations in H_2S availability during sulfide precipitation. Sulfide deposition under H_2S-deficient conditions could result if the metalliferous fluids were S poor and exhaled into environments where limited H_2S was available to form sulfides. Alternatively, it could have arisen if the hydrothermal fluids were oxidized and mainly carried S as SO_4^{2-}, and bacterial or thermochemical reduction to H_2S needed to form sulfides was kinetically too slow to build up sufficiently high H_2S concentrations to form polymetallic assemblages of galena, sphalerite, and Fe sulfides (Ohmoto and Goldhaber, 1997).

The H_2S, often with isotope values relatively close to zero, may have been derived from a number of processes, including bacteriogenic sulfate reduction (BSR) or thermochemical sulfate reduction (TSR) and partly also from leached volcanic S, as further discussed below. However, the limited amount of data and lack of absolute values, e.g., for depositional temperatures, hinders a quantification of their relative importance. As is common for regionally metamorphosed ore deposits, many of the sulfide pairs are out of equilibrium, and T calculations do not yield any consistent values.

Pb-Ag in the Lovisa Iron Formation

Deposition under H_2S-deficient conditions could explain the low $\delta^{34}S$ and low Zn/Pb of sulfide mineralization in the Lovisa Fe formation, assuming that the hydrothermal fluid transported Fe, Pb, and Zn. The gradational decrease in Zn and Pb and the disappearance of sulfides upward from the base of the Fe formation could be explained if H_2S became completely exhausted with time (Fig. 16A-C). The galena $\delta^{34}S$ is consistent with a low-T (in the 150°–100°C range) fractionation between galena and H_2S at around 0‰, suggesting a volcanic-magmatic source for the S, yet this alternative is not favored since is it more difficult to explain the isotopically light sphalerite (–4.9‰) by this mechanism. Furthermore, the combination of high Ba (Fig. 16G), the very high Fe content, and significant Pb and Zn contents necessitates efficient transport of these elements in solution. Barium is only very weakly soluble in the presence of SO_4^{2-}, which suggests that the fluid was SO_4^{2-} poor and not highly oxidized. The near-neutral pH in the hydrothermal fluid interpreted above indicates that the fluid could not transport significant amounts of Zn and Pb in the presence of H_2S (cf. Cooke et al., 2000). Thus, the most likely scenario is that the metalliferous fluid was S poor and mixed with H_2S sourced from seawater sulfate following exhalation.

The generally slightly negative $\delta^{34}S$ values in sulfides from the Lovisa Fe formation are consistent with BSR of Early
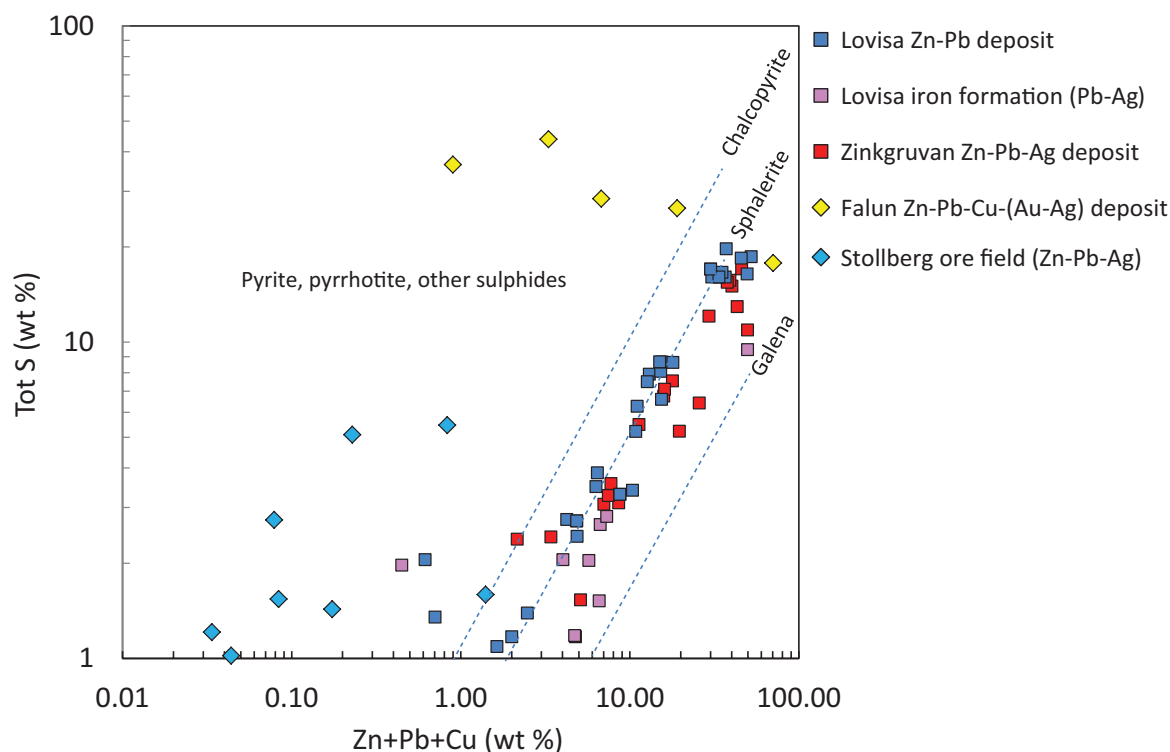
Fig. 20. Total S vs. Zn + Pb + Cu plot for the Lovisa Zn-Pb sulfide deposit and Pb-Ag mineralization in the Lovisa Fe formation. Ore zone analyses from the stratiform Zn-Pb-Ag ore at Zinkgruvan (N. Jansson, unpub. data, 2017) and stratabound limestone- and skarn-hosted polymetallic sulfide deposits at Stollberg (Jansson et al., 2013) and Falun (Kampmann et al., 2017) have been plotted for comparison. The theoretical mixing lines for monomineralic compositions chalcopyrite, sphalerite, and galena at different abundances are shown for reference. Whereas total S in rocks at Zinkgruvan and Lovisa seldom exceeds that which can be attributed to sphalerite and galena in the rocks, Stollberg and Falun samples nearly consistently plot to the left of the Lovisa samples, reflecting the presence of additional S in Fe sulfide. The Stollberg samples are from samples equally as magnetite rich as those from the Lovisa Fe formation.

Proterozoic seawater sulfate at $\delta^{34}S$ = 17‰ (Claypool et al., 1980) in a closed system (ΔH_2S-SO_4^{2-} is likely within the range 15–30‰; Ohmoto et al., 1990) where Rayleigh isotopic fractionation processes also might have played a role. The $\delta^{34}S$ values could also be explained by kinetic fractionation during TSR of seawater sulfate at ca. 100°C ($\Delta^{34}S_{SO_4\text{-}H_2S}$ = 20‰; Machel et al., 1995).

The Lovisa Zn-Pb Ore

The tectonic modification of the main ore makes it uncertain to what extent the decrease in Zn/Pb and $\delta^{34}S$ stratigraphically upward in the Lovisa Zn-Pb deposit is a primary stratigraphic feature or whether it could be related to postore modification. A primary origin for the variable Zn/Pb and $\delta^{34}S$ trend is supported by the fact that this pattern is observed in the most well-preserved, laminated sphalerite facies of both ore beds (Fig. 17). Wagner et al. (2005) showed that formation of synmetamorphic, Ag-rich sulfide-sulfosalt veins by remobilization of preexisting polymetallic sulfide mineralization at Hällefors produced insignificant $\delta^{34}S$ fractionation to slightly lower values. Thus, the $\delta^{34}S$ of sulfides in the main ore at Lovisa are likely inherited largely from the precursor sulfide mineralization.

The highest $\delta^{34}S$ values are in pyrite in and directly below the sphalerite ore (3.3–5.4‰), in the same stratigraphic interval in which sphalerite has the highest $\delta^{34}S$

values (1.4–4.7‰). These values are somewhat high to be accounted for by BSR of seawater sulfate, unless the $\delta^{34}S_{SO_4^{2-}}$ in the water column was higher than 17‰. They are, however, within the range of $\delta^{34}S$ values derived by kinetic fractionation during thermochemical reduction of seawater sulfate at ca. 150° to 200°C ($\Delta^{34}S_{SO_4\text{-}H_2S}$ = 10–15‰; Machel et al., 1995). The Fe-poor nature of sphalerite in the sphalerite ore is consistent with formation at relatively low temperatures, since the Fe content of sphalerite decreases with decreasing temperature and increasing a_{S_2} (e.g., Hannington and Scott, 1989). The paragenetically later red sphalerite in the laminated facies is presumably more Fe rich and likely crystallized at a higher temperature. The overlap in δ^{34} with coarse-grained sphalerite and galena in adjacent veins suggests that the red sphalerite may very well have crystallized in conjunction with local remobilization during vein formation.

The pyrite porphyroblasts in the red rhyolitic ash-siltstone below the sphalerite do not define any lamination, suggesting that they formed beneath the sea floor. The coexisting Ba-rich feldspars are texturally similar to complexly zoned hyalophane described in the Early Proterozoic Cuyuna Fe range by McSwiggen et al. (1994). As at Lovisa, textural evidence for replacement of earlier barite is lacking in this area, whereby McSwiggen et al. (1994) attributed the hyalophane to diagenetic or metamorphic dehydration of earlier authigenic Ba-Al

silicates formed in a SO_4^{2-}-depleted setting. The stratabound occurrence of pyrite and Ba feldspars in a relatively thin zone of commonly hematite stained volcaniclastic rocks stratigraphically below the sphalerite ore is consistent with pyrite formed when H_2S diffused down from the overlying water column and reacted with Fe oxides.

The slight decrease in $\delta^{34}S$ stratigraphically upward from the sphalerite ore to the main ore is opposite to the trend expected if the H_2S in the Lovisa Zn-Pb deposit was exclusively derived from BSR or TSR of seawater SO_4^{2-} undergoing Rayleigh isotopic fractionation in a closed system (cf. Ohmoto and Goldhaber, 1997; Seal II, 2006). Rather, the narrower $\delta^{34}S$ values close to 0‰ for the main ore could imply that leached volcanic S similar to other sulfide deposits in the Bergslagen district (cf. Wagner et al., 2005) became more important during this final stage of the mineralizing process.

Geochemical modeling by Cooke et al. (2000) suggests that Zn and Pb are equally soluble in the presence of H_2S in near-neutral fluids at ca. 225°C but that the Pb solubility decreases more rapidly than Zn with falling temperature. Consequently, the lower Zn/Pb ratio of the main ore compared with the sphalerite ore could imply that the latter formed from a fluid that vented at a lower temperature. However, assuming H_2S derivation from TSR, this is not supported by the lower $\delta^{34}S$ in the main ore, since $\Delta^{34}S_{SO_4-H_2S}$ increases with decreasing

temperature (Machel et al., 1995). However, the coupled high Zn/Pb and $\delta^{34}S$ in the sphalerite ore (Fig. 21) could be accounted for if the fluid pulse, which formed the sphalerite ore, had already deposited galena elsewhere in the system (e.g., more proximal to the vent); this would have caused an increase in both Zn/Pb and $\delta^{34}S_{TOT}$ in the fluid prior to forming the sphalerite ore. In this context, the lower Zn/Pb and $\delta^{34}S$ in the main ore could be explained if the fluid pulse, which formed the main ore, reached the sea floor less fractioned regarding Zn/Pb and $\delta^{34}S$.

The apparent vent-distal nature of the sulfide mineralization suggests that only a part of the Lovisa ore system has been discovered and/or preserved. In the absence of a larger study incorporating vent zones and possible source regions, it is difficult to assess fully the cause of the observed differences in metal ratios and $\delta^{34}S_{TOT}$ in the fluid en route to forming the studied sulfide beds. Nevertheless, our results indicate that during local basin evolution, syngenetic-exhalative sulfide deposits accumulated at various times under generally H_2S-deficient conditions. Although the S source cannot be uniquely constrained, the results are permissive of a setting in which early mineralizing phases mainly utilized H_2S derived from BSR and TSR of seawater sulfate, whereas leached volcanic S introduced by hydrothermal fluids became more important with time.
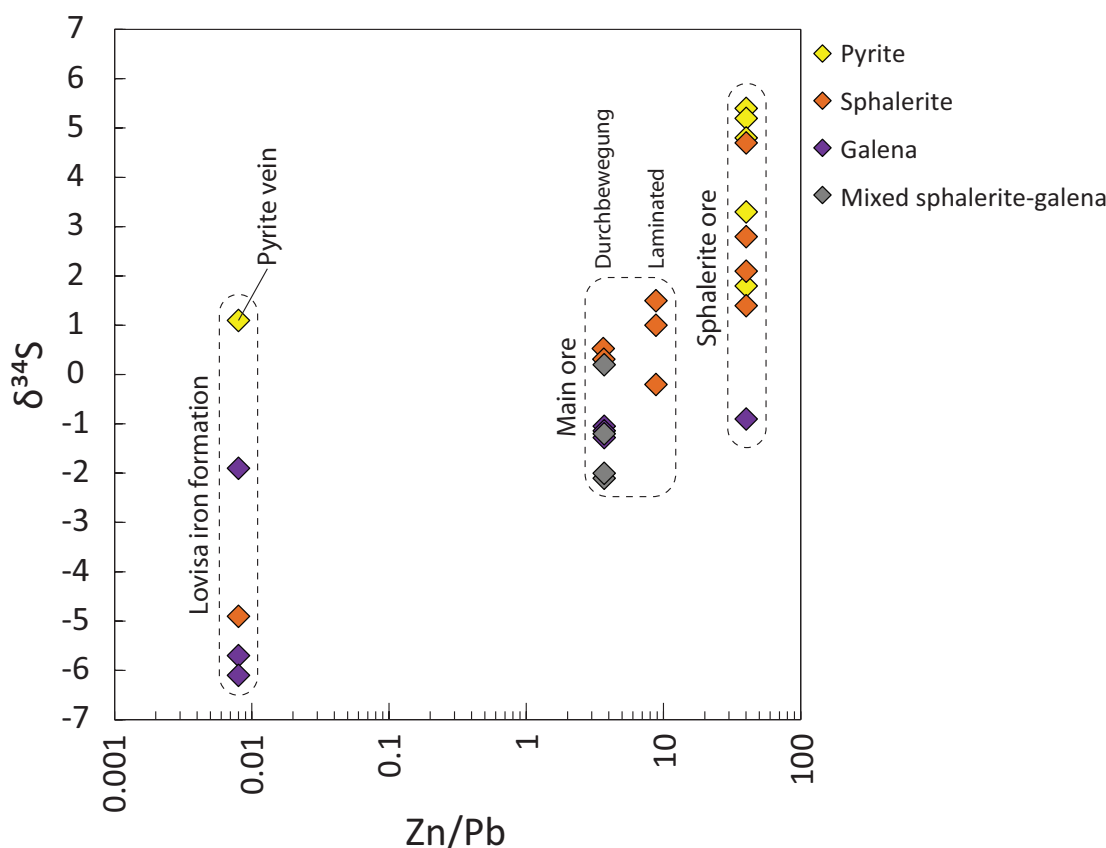

Fig. 21. $\delta^{34}S$ vs. Zn/Pb plot for sulfides. The $\delta^{34}S$ values have been grouped according to mineralization type as in Figure 17 and plotted against the average of Zn/Pb of the given mineralization type based on assay data. An average Zn/Pb cannot be provided for the veins in the main ore, which are here grouped with the ore with durchbewegung texture. Although there is a limited number of samples, there is a general trend to higher $\delta^{34}S$ in, e.g., sphalerite from mineralization types with higher Zn/Pb.

Evidence for saline fluids and/or brine pools

Although the metamorphic overprint precludes an estimate of the salinity of the exhaled fluids based on fluid inclusions, there are several indirect indications that the deposits formed from relative saline hydrothermal fluids or that they accumulated in brine pools. Oen and Lustenhouwer (1992) described Cl-rich biotites identical to those that occur in the Lovisa Fe formation from broadly stratigraphically equivalent metaexhalites in the Nora area farther south in the Guldsmedshyttan syncline. These authors attributed the high-Cl content to the passage of high-salinity brines derived from seawater and/or to the former presence of Cl-rich authigenic minerals (halite and sylvite). A high-Cl content in the fluids that formed the Lovisa Fe formation would facilitate the transport of Fe and base metals, even under the near-neutral pH conditions inferred from the REE patterns and limestone in the footwall (cf. Seward and Barnes, 1997; Cooke et al., 2000). Hellingwerf et al. (1994) suggested that high B contents such as those observed in the Lovisa stratigraphy might have been derived from hydrothermal brines sourced from Proterozoic seawater. Jansson et al. (2017) suggested that the brines that enriched the stratigraphic footwall of the Zinkgruvan deposit in K and B might have been derived from the evaporation of seawater.

The best evidence for former brine pools is the presence of concordant zones of anomalous $K_2O/(K_2O + Na_2O)$ in mainly albite-rich rocks that envelop the Lovisa Zn-Pb deposit. The halo-like distributions of zones with variable $K_2O/(K_2O + Na_2O)$ contrast with normal styles of alkali alteration in Bergslagen, wherein several 100-m-thick, extensive packages of K-feldspar–altered rocks are generally underlain by thick successions of albite-altered rocks (e.g., Lagerblad and Gorbatchev, 1985; Stephens et al., 2009; Jansson et al., 2013).

Concordant haloes of intense alkali enrichment have been described around vent-distal SEDEX deposits, such as the McArthur River deposit (Croxford, 1964; Lambert and Scott, 1973). Sangster (2002) attributed this alteration style to dense, alkali-rich brines that formed pools on the sea floor and sank into the underlying sediments. Alteration of volcanic glass and clays to sodic zeolites, analcime, and adularia has been described from saline-alkaline lakes (e.g., Parker and Surdam, 1971; Ratterman and Surdam, 1981; Remy and Ferrel, 1989). It is conceivable that similar processes could operate in and below brine pools and that medium-grade metamorphism would convert such authigenic minerals to feldspars. Thus, we interpret the Lovisa Zn-Pb deposit to have been deposited in an alkali-rich brine pool.

In detail, the Na-altered zone below the sphalerite ore is pink-red, hematite stained with porphyroblasts of pyrite and lesser magnetite. The alteration scheme of Remy and Ferrell (1989) describes Fe oxide or hydroxide as a byproduct of analcime formation upon interaction of oxidized, Na-rich brine with detrital phyllosilicates. In contrast, the Na-altered zone above the main ore is gray-white, pyrite poor, and devoid of Fe oxides. This may indicate that the brine pool was originally oxidizing but became more reducing with time.

During or shortly before formation of the Lovisa Zn-Pb deposit, a relatively oxidized, Na-rich brine pool may have formed by evaporation of seawater or exhalation of Na-rich brines and with time evolved toward more reducing conditions

favorable for sulfate reduction (cf. Sangster, 2002). However, all base metal sulfide-bearing intervals coincide with distinct peaks in high $K_2O/K_2O + Na_2O$ within the albite-altered intervals. This may imply a more complex brine pool history wherein the sulfide deposits formed in conjunction with distinct pulses of exhalation of K-rich fluids into the brine pool, causing perturbations in the brine pool chemistry. Such a scenario would be consistent with the episodic nature of sulfide ore formation as reflected by different sulfide beds with different Zn/Pb and $\delta^{34}S$ values. A K-rich composition for the metalliferous fluids has been invoked for Zinkgruvan, where the stratiform Zn-Pb-Ag ore is enveloped and underlain by intensely K-feldspar–altered rocks (Hedström et al., 1989; Jansson et al., 2017).

Comparison with Zinkgruvan, VMS deposits, and SEDEX deposits

The regional stratigraphic pattern at Lovisa follows a pattern broadly similar to that at Zinkgruvan (cf. Hedström et al., 1989; Allen et al., 1996; Kumpulainen et al., 1996, Jansson et al., 2017), wherein the stratiform Zn-Pb-Ag ore occurs in the upper part of a thick felsic volcaniclastic succession deposited at a time of waning volcanic activity close to the transition to an overlying, postvolcanic sedimentary sequence. Similar to Zinkgruvan, stratiform Zn-Pb ± Ag mineralization occurs in a stratigraphic interval in which both a felsic volcaniclastic component and a marine clay component can be identified and where interbedding with former limestone units is common. At Zinkgruvan, Jansson et al. (2017) argued that there is no strong evidence for contemporaneous volcanism and that the fine-grained volcaniclastic component may consist of reworked volcanic detritus. This, along with the earlier mentioned conclusions on fluid chemistry, led Jansson et al. (2017) to consider a SEDEX model for Zinkgruvan.

The Lovisa deposit shares many key features of the SEDEX genetic model, such as (1) the low aspect ratio of the stratiform sulfide mineralization, (2) variable $\delta^{34}S$ in sulfides, and (3) the inference of saline, alkali-rich, possibly oxidized ore-forming brines. Unlike at Zinkgruvan, however, the presence of coarse-grained, pumiceous mass flow deposits clearly indicates that the mineralization at Lovisa formed in an episodically volcanically active basin. In addition, feldspar-destructive alteration is absent at Zinkgruvan, whereas quartz-sericite-chlorite alteration has been documented in the stratigraphic footwall near Lovisa (e.g., east of Håkansboda; Fig. 3; Carlon and Bleeker, 1988). The Lovisa area furthermore differs from Zinkgruvan and SEDEX deposits in that the sulfide mineralizations occur in an area rich in stratiform Mn-rich Fe oxide deposits. Manganese-rich Fe oxide deposits are subordinate to Zn-Pb-Ag mineralization at Zinkgruvan, where they occur as discontinuous, stratabound zones in the stratigraphic footwall (Jansson et al., 2017).

The stratiform sulfide beds at Lovisa possess some features of both SEDEX and VMS deposits. As in VMS systems, thermal perturbations related to volcanism may have been important for driving hydrothermal fluid flow and for generation of thick succession of originally vitreous, pyroclastic debris that could be leached of metals and S. However, as in SEDEX systems, formation of the sulfide deposits appears to have been dependent on the generation and discharge of highly

saline brines into relatively deep marine environments favorable for sulfate reduction and accumulation and preservation of sulfides.

Such environments were rare in Bergslagen owing to the almost constant volcanism and resedimentation of volcaniclastic detritus, which generally kept pace with basin subsidence and thus maintained shallow marine environments (Allen et al., 1996, 2003). In this sense, the significantly higher tonnage and thickness of stratiform Zn-Pb ± Ag mineralization at Zinkgruvan likely reflects a more favorable depositional environment in part related to less volcanic input into the basin. Sulfides at Zinkgruvan accumulated during a postvolcanic stage and were overlain by a metamorphosed organic-rich mudstone facies (Jansson et al., 2017). These in turn grade stratigraphically upward into a thick succession of migmatized, graphite-bearing pelitic rocks, implying a long-lived, anoxic environment with low sedimentation rates. However, at Lovisa, stratiform mineralization is restricted to relatively thin stratigraphic intervals between beds of proximal-medial volcaniclastic rocks, and hematite-bearing BIF occurs in the stratigraphic hanging wall (Fig. 12C). Thus, formation of sulfide mineralization at Lovisa may be related to the coincidence of discharge of metal-bearing brines, relatively deep water environment, and brief periods of extremely low volcaniclastic sedimentation rate, during which the basin could evolve to more reducing conditions.

There are also differences in the style and scale of associated hydrothermal alteration. At Zinkgruvan, even at the vent-distal parts of the deposit, the mineralization is underlain by extensive volumes of homogeneous K-feldspar–altered rocks, whereas at Lovisa K alteration and other alteration types are less intense and more heterogeneously distributed. These differences may indicate that Zinkgruvan formed from a much larger hydrothermal system. It should, however, be emphasized here that the Zinkgruvan area is better explored.

Conclusions

Despite polyphase ductile deformation, amphibolite facies regional metamorphism, and subsequent brittle faulting, stratiform Zn-Pb ± Ag sulfide and Fe oxide deposits in the Lovisa area have retained evidence of a vent-distal exhalative origin. These deposits accumulated during periods of very low rates of volcaniclastic sedimentation between deposition of pumiceous, rhyolitic mass flow deposits in an actively subsiding basin. Deposition of the Lovisa Fe formation with subordinate Pb-Ag mineralization is attributed to discharge of an Fe-rich, S-poor brine at a near-neutral pH, which mixed with a preexisting H_2S reservoir above the sediment-water interface. The low Zn/Pb ratio and low Fe sulfide content is attributed to sulfide deposition under H_2S-deficient conditions.

The Lovisa Zn-Pb deposit is inferred to have formed at a later stage in an alkali-rich brine pool, which was periodically recharged with base metal-bearing hydrothermal fluids. The ore-forming system first deposited a nearly monomineralic sphalerite bed with positive $\delta^{34}S$ values (sphalerite ore) and subsequently a sphalerite + galena bed with $\delta^{34}S$ close to 0‰ (main ore). The upward decreasing $\delta^{34}S$ may reflect a decreasing importance of H_2S derived from TSR and/or BSR of seawater SO_4^{2-} relative to S sourced from leaching of volcanic rocks. The high content of galena in the main ore led

to partitioning of strain in this bed during subsequent ductile deformation, leading to the development of durchbewegung texture and remobilization of sphalerite and galena to veins. Remobilization appears to have only caused minor if any S isotope fractionation.

Our stratigraphic analysis shows that intervals of low sedimentation rate favorable for accumulation of hydrothermal sediments were established at several times during the stratigraphic evolution but that Mn-rich Fe oxide deposits mainly formed during such intervals. This may be because the vented fluids were mainly low-T fluids incapable of significant transport of base metals. However, results from Lovisa suggest that other reasons for the paucity of sulfide deposits in these intervals may have been a low H_2S content in the vented hydrothermal fluids and a general H_2S deficiency at the depositional sites. The latter may in turn be related to the mainly shallow marine environments due to infilling of the basin by volcaniclastic detritus. Long-lived, calm depositional environments rarely developed.

Whereas we infer that coeval volcanism was beneficial for driving hydrothermal fluid flow and for supplying a reservoir of metals and S that could be leached, we note that Zinkgruvan, which is the largest stratiform Zn-Pb ± Ag deposit in Bergslagen, formed at the stratigraphic boundary between an underlying volcanic and limestone succession and an overlying postvolcanic deep-water sedimentary succession recording long-lived anoxic conditions. Thus, we speculate that the generally high degree of volcaniclastic input and predominance of shallow marine environments in Bergslagen might have been a critical factor as to why large Zn-Pb ± Ag deposits are not more common.

REFERENCES

Alibo, D.S., and Nozaki, Y., 1999, Rare earth elements in seawater: Particle association, shale-normalization, Ce oxidation: Geochimica et Cosmochimica, v. 63, p. 363–372.

Allen, R.L., Lundström, I., Ripa, M., and Christofferson, H., 1996, Facies analysis of a 1.9 Ga, continental margin, back-arc, felsic caldera province with diverse Zn-Pb-Ag-(Cu-Au) sulfide and Fe oxide deposits, Bergslagen region, Sweden: Economic Geology, v. 91, p. 979–1008.

Allen, R.L., Bull, S., Ripa, M., and Jonsson, R., 2003, Regional stratigraphy, basin evolution, and the setting of stratabound Zn-Pb-Cu-Ag-Au deposits in Bergslagen, Sweden: Geological Survey of Sweden-Research and Development, report 03-1203/99, 80 p.

Barker, A.K., Troll, V.R., Carracedo, J.-C., and Nicholls, P.A., 2015, The magma plumbing system for the 1971 Tenguia eruption, La Palma, Canary Islands: Contributions to Mineralogy and Petrology, v. 170, no. 54, doi: 10.1007/s00410-015-1207-7.

Barrett, T.J., and MacLean, W.H., 1994, Chemostratigraphy and hydrothermal alteration in exploration for VHMS deposits in greenstones and younger volcanic rocks: Geological Association of Canada Short Course Notes, v. 11, p. 433–467.

——1999, Volcanic sequences, lithogeochemistry, and hydrothermal alteration in some bimodal volcanic-associated massive sulfide systems: Reviews in Economic Geology, v. 8, p. 101–131.

Bau, M., 1996, Controls on the fractionation of isovalent trace elements in magmatic and aqueous systems: Evidence from Y/Ho, Zr/Hf, and lanthanide tetrad effect: Contributions to Mineralogy and Petrology, v. 123, p. 323–333.

——1999, Scavenging of dissolved yttrium and rare earths by precipitating iron oxyhydroxide: Experimental evidence for Ce oxidation, Y-Ho fractionation, and lanthanide tetrad effect: Geochimica et Cosmochimica Acta, v. 63, p. 67–77.

Bau, M., and Dulski, P., 1996, Distribution of yttrium and rare earth elements in the Penge and Kuruman iron formations, Transvaal Supergroup, South Africa: Precambrian Research, v. 79, p. 37–55.

Beeson, R., 1990, Broken Hill-type lead-zinc deposits—an overview of their occurrence and geological setting: Transactions of the Institution of Mining and Metallurgy, v. 99, p. 163–175.

Bekker, A., Slack, J.F., Planavsky, N., Krapez, B., Hofmann, A., Konhauser, K.O., and Rouxel, O.J., 2010, Iron formation: The sedimentary product of a complex interplay among mantle, tectonic, oceanic, and biospheric processes: Economic Geology, v. 105, p. 467–508.

Beunk, F.F., and Kuipers, G., 2012, The Bergslagen ore province, Sweden: Review and update of an accreted orocline, 1.9–1.8 Ga BP: Precambrian Research, v. 216–219, p. 95–119.

Billström, K., 1991, Sulphur isotope compositions in the Åmmeberg Zn-Pb ore deposit, south-central Sweden: Genetic implications: Geologische Rundschau, v. 80, p. 717–727.

Bleeker, W., 1984, Geology of the Stråssa-Torrsjöboda area and the Håkansboda-Ingelshyttan area, map sheets 11F 4c, 11F 4d, 11F 4e: Unpublished exploration report for Luossavaara-Kirunavaara Aktiebolag (LKAB) and British Petroleum (BP) AB Joint Venture, B85-12, 97 p., www.resource.sgu.se/dokument/geodigitalia/rapporter/b_8512.pdf.

Boström, K., 1973, The origin and fate of ferromanganoan active ridge sediments: Stockholm Contributions in Geology, v. 27, 95 p.

Carlon, C.J., 1987, The Lovisa project 1985–1986: Unpublished exploration report for Luossavaara-Kirunavaara Aktiebolag (LKAB) and British Petroleum (BP) AB Joint Venture, B87-1, v. l, 127 p., available via the Geological Survey of Sweden, http://resource.sgu.se/dokument/geodigitalia/rapporter/b_8701.pdf.

Carlon, C.J., and Bleeker, W., 1988, The geology and structural setting of the Håkansboda Cu-Co-As-Sb-Bi-Au deposit and associated Pb-Zn-Cu-Ag-Sb mineralisation, Bergslagen, central Sweden: Geologie en Mijnbouw, v. 67, p. 272–292.

Claypool, G.E., Holser, W.T., Kaplan, I.R., Sakai, H., and Zak, I., 1980, The age curves of sulfur and oxygen isotopes in marine sulfate and their mutual interpretation: Chemical Geology, v. 28, p. 199–260.

Cooke, D.R., Bull, S.W., Large, R.R., and McGoldrick, P.J., 2000, The importance of oxidized brines for the formation of Australian Proterozoic stratiform sediment-hosted Pb-Zn (sedex) deposits: Economic Geology, v. 95, p. 1–18.

Croxford, N.J.W., 1964, Origin and significance of volcanic potash-rich rocks from Mount Isa: Transactions of the Institute of Mining and Metallurgy, v. 74, p. 33–43.

De Baar, H.J.W., Brewer, P.G., and Bacon, M.P., 1985, Anomalies in rare-earth distributions in seawater: Gd and Tb: Geochimica et Cosmochimica Acta, v. 49, p. 1961–1969.

Emsbo, P., McLaughlin, P.I., Breit, G.N., Bray, E.A.D., and Koenig, A.E., 2015, Rare earth elements in sedimentary phosphate deposits: Solution to the global REE crisis?: Gondwana Research, v. 27, p. 776–785.

Engvall, A., and Persson, H., 1985, The structural geology of the northern part of the Guldsmedshytte syncline: Unpublished exploration report for Luossavaara-Kirunavaara Aktiebolag (LKAB) and British Petroleum (BP) AB Joint Venture, B85-21, 14 p., www.resource.sgu.se/dokument/geodigitalia/rapporter/b_8521.pdf.

French, B.M., 1970, Stability relations of siderite (FeCO$_3$), determined in controlled-f_{O_2} atmospheres: NASA technical report NASA-TM-X-63895, X-644-70-102, 67 p., www.ntrs.nasa.gov/archive/nasa/casi.ntrs.nasa.gov/19700019391.pdf.

Gadd, M.G., Layton-Matthews, D., and Peter, J.M., 2016, Non-hydrothermal origin of apatite in SEDEX mineralization and host rocks of the Howard's Pass district, Yukon, Canada: Canadian Mineralogist, v. 101, p. 1061–1071.

Gavelin, S., Parwel, A., and Ryhage, R., 1960, Sulfur isotope fractionation in sulfide mineralization: Economic Geology, v. 55, p. 510–530.

Geijer, P., 1927, Stråssa och Blanka järnmalmsfält: Geological Survey of Sweden, Ca 20, 48 p. (in Swedish).

Geijer, P., and Magnusson, N.H., 1944, De mellansvenska järnmalmernas geologi: Geological Survey of Sweden, Ca 35, 654 p.

Halevy, I., Alesker, M., Schuster, E.M., Popovitz-Biro, R., and Feldman, Y., 2017, A key role for green rust in the Precambrian oceans and the genesis of iron formations: Nature Geoscience, v. 10, p. 135–139.

Hannington, M.D., and Scott, S.D., 1989, Sulfidation equilibria as guides to gold mineralization in volcanogenic massive sulfides; evidence from sulfide mineralogy and the composition of sphalerite: Economic Geology, v. 84, p. 1978–1995.

Hedström, P., Simeonov, A., and Malmström, L., 1989, The Zinkgruvan ore deposit, south-central Sweden: A Proterozoic, proximal Zn-Pb-Ag deposit in distal volcanic facies: Economic Geology, v. 84, p. 1235–1261.

Hellingwerf, R., 1996, Regional and local hydrothermal alteration of Proterozoic metavolcanic footwall rocks of the Zinkgruvan Zn-Pb-Ag ore deposit, central Sweden: Neues Jahrbuch für Mineralogie, Monatshefte 11, p. 491–518.

Hellingwerf, R.H., and van Raaphorst, J.G., 1988, Sulphur isotopes from the Gruvåsen sulphide skarn deposit, Bergslagen, Sweden: Mineralogy and Petrology, v. 38, p. 161–170.

Hellingwerf, R.H., Liljequist, R., and Ljung, S., 1988, Stratiform Zn-Pb-Fe-Mn mineralization in the Älvlången-Vikern area, Bergslagen, Sweden: Geologie en Mijnbouw, v. 67, p. 313–332.

Hellingwerf, R.H., Gatedal, K., Gallagher, V., and Baker, J.H., 1994, Tourmaline in the central Swedish ore district: Mineralium Deposita, v. 28, p. 189–205.

Hughes, C.J., 1973, Spilites, keratophyres, and the igneous spectrum: Geological Magazine, v. 109, p. 513–527.

Jansson, N.F., 2011, The origin of iron ores in Bergslagen, Sweden, and their relationships with polymetallic sulphide ores: Unpublished Ph.D. thesis, Luleå, Sweden, Luleå University of Technology, 73 p.

Jansson, N.F., and Allen, R.L., 2011, The origin of skarn beds, Ryllshyttan Zn-Pb-Ag + magnetite deposit, Bergslagen, Sweden: Mineralogy and Petrology, v. 103, p. 49–78.

——2015, Multistage ore formation at the Ryllshyttan marble and skarn-hosted Zn-Pb-Ag-(Cu) + magnetite deposit, Bergslagen, Sweden: Ore Geology Reviews, v. 69, p. 217–242.

Jansson, N.F., Erismann, F., Lundstam, E., and Allen, R.L., 2013, Evolution of the Palaeoproterozoic volcanic limestone-hydrothermal sediment succession and Zn-Pb-Ag and iron oxide deposits at Stollberg, Bergslagen region, Sweden: Economic Geology, v. 108, p. 309–335.

Jansson, N.F., Zetterqvist, A., Malmström, L., and Allen, R.L., 2017, Genesis of the Zinkgruvan stratiform Zn-Pb-Ag deposit and associated dolomite-hosted Cu ore, Bergslagen, Sweden: Ore Geology Reviews, v. 82, p. 285–308.

Johansson, Å., and Hålenius, U., 2013, Palaeoproterozoic mafic intrusions along the Avesta-Östhammar belt, east-central Sweden: Mineralogy, geochemistry, and magmatic evolution: International Geology Review, v. 55, p. 131–157.

Johansson, Å., and Stephens, M.B., 2017, Timing of magmatism and migmatization in the 2.0–1.8 Ga accretionary Svecokarelian orogeny, south-central Sweden: International Journal of Earth Sciences, v. 106, p. 782–810.

Jonsson, E., and Billström, K., 2009, Lead isotope systematics in the Långban deposit and adjacent sulphide mineralisations in western Bergslagen, Sweden: GFF, v. 131, p. 215–227.

Kampmann, T.C., Jansson, N.F., Stephens, M.B., Majka, J., and Lasskogen, J., 2017, Systematics of hydrothermal alteration at the Falun base metal sulfide deposit and implications for ore genesis and exploration, Bergslagen ore district, Fennoscandian Shield, Sweden: Economic Geology, v. 112, p. 1111–1152.

Klein, C., 1973, Changes in mineral assemblages with metamorphism of some banded Precambrian iron-formations: Economic Geology, v. 68, p. 1075–1088.

Kumpulainen, R.A., Mansfeld, J., Sundblad, K., Neymark, L., and Bergman, T., 1996, Stratigraphy, age, and Sm-Nd isotope systematics of the country rocks to Zn-Pb sulfide deposits: Economic Geology, v. 91, p. 1009–1021.

Labrenz, M., Druschel, G.M., Thomsen-Ebert, T., Gilbert, B., Welch, S.S., Kemner, K.M., Logan, G.A., Summons, R.E., De Stasio, G., Bond, P.L., Lai, B., Kelly, S.D., and Banfield, J.L., 2000, Formation of sphalerite (ZnS) deposits in natural biofilms of sulfate-reducing bacteria: Science, v. 290, p. 1744–1747.

Lagerblad, B., and Gorbatschev, R., 1985, Hydrothermal alteration as a control of regional geochemistry and ore formation in the central Baltic Shield: Geologische Rundschau, v. 74, p. 33–49.

Lambert, I.B., and Scott, K.M., 1973, Implications of geochemical investigations of sedimentary rocks within and around the zinc-lead-silver deposit, Northern Territory, Australia: Journal of Geochemical Exploration, v. 2, p. 307–330.

Large, R.R., Gemmell, B.J., Paulick, H., and Huston, D.L., 2001, The alteration box plot: A simple approach to understanding the relationship between alteration mineralogy and lithogeochemistry associated with volcanic-hosted massive sulfide deposits: Economic Geology, v. 96, p. 957–971.

Le Bas, M.J., Le Maitre, R.W., Streckeisen, A., and Zanettin, B., 1986, A chemical classification of volcanic rocks based on the total alkali-silica diagram: Journal of Petrology, v. 27, p. 745–750.

Lundström, I., 1983, Beskrivning till Berggrundskartan. Lindesberg SV: Geological Survey of Sweden, Af 126, 140 p. (in Swedish).

Machel, H., Krouse, H., and Sassen, R., 1995, Products and distinguishing criteria of bacterial and thermochemical sulfate reduction: Applied Geochemistry, v. 10, p. 373–389.

Marshall, B., and Gilligan, L.B., 1987, An introduction to remobilization: Information from orebody geometry and experimental considerations: Ore Geology Reviews, v. 2, p. 87–131.

McLennan, S.M., Hemming, S., McDanniel, D.K., and Hanson, G.N., 1993, Geochemical approaches to sedimentation, provenance, and tectonics: Geological Society of America, Special Paper 285, p. 21–40.

McSwiggen, P.L., Morey, G.B., and Cleland, J.M., 1994, Occurrence and genetic implications of hyalophane in manganese-rich iron-formation, Cuyuna iron range, Minnesota, USA: Mineralogical Magazine, v. 58, p. 387–399.

Meinert, L.D., Dipple, G.M., and Nicolescu, S., 2005, World skarn deposits: Economic Geology 100th Anniversary Volume, p. 299–336.

Oen, I.S., and Lustenhouwer, W.J., 1992, Cl-rich biotite, Cl-K hornblende, and Cl-rich scapolite in metaexhalites; Nora, Bergslagen, Sweden: Economic Geology, v. 87, p. 1638–1648.

Ohmoto, H., and Goldhaber, M.B., 1997, Sulfur and carbon isotopes, *in* Barnes, H.L., ed., Geochemistry of hydrothermal ore deposits, 3rd ed.: New York, Wiley, p. 517–611.

Ohmoto, H., Kaiser, C.J., and Geer, K.A., 1990, Systematics of sulphur isotopes in recent marine sediments and ancient sediment-hosted base metal deposits, *in* Herbert, H.K., and Ho, S.E., eds., Stable isotopes and fluid processes in mineralization: Perth, University of Western Australia, p. 70–120.

Parker, R.B., and Surdam, R.C., 1971, A summary of authigenic silicates in the tuffaceous rocks of the Green River Formation: Rocky Mountain Geology, v. 10, p. 69–72.

Peter, J.M., 2003, Ancient iron formations: Their genesis and use in the exploration for stratiform base metal sulphide deposits, with examples from the Bathurst mining camp: Geological Association of Canada, GeoText 4, p. 145–176.

Peter, J.M., Goodfellow, W.D., and Doherty, W., 2003, Hydrothermal sedimentary rocks of the Heath Steele belt, Bathurst mining camp, New Brunswick: Part 2. Bulk and rare earth element geochemistry and implications for origin: Economic Geology Monograph 11, p. 391–415.

Ratterman, N.G., and Surdam, R.C., 1981, Zeolite mineral reactions in a tuff in the laney member of the Green River Formation, Wyoming: Clays and Clay Minerals, v. 29, p. 365–377.

Remy, R.R., and Ferrell, R.E., 1989, Distribution and origin of analcime marginal lacustrine mudstones of the Green River Formation, Utah: Clays and Clay Mineral, v. 37, p. 419–432.

Robinson, B.W., and Kusakabe, M., 1975, Quantitative preparation of SO_2 for $^{34}S/^{32}S$ analysis from sulfides by combustion with cuprous oxide: Analytical Chemistry, v. 47, v. 1179–1181.

Romer, R.L., and Wright, J.E., 1993, Lead mobilization during tectonic reactivation of the western Baltic Shield: Geochimica et Cosmochimica Acta, v. 57, v. 2555–2570.

Sangster, D.F., 2002, The role of dense brines in the formation of vent-distal sedimentary-exhalative (SEDEX) lead-zinc deposits: Field and laboratory evidence: Mineralium Deposita, v. 37, p. 149–157.

Seal II, R.R., 2006, Sulfur isotope geochemistry of sulfide minerals: Reviews in Mineralogy and Geochemistry, v. 61, p. 633–677.

Seward, T.M., and Barnes, H.L., 1997, Metal transport by hydrothermal ore fluids, *in* Barnes, H.L., ed., Geochemistry of hydrothermal ore deposits, 3rd ed.: New York, Wiley, p. 435–486.

Söderlund, U., Isachsen, C., Bylund, G., Heaman, L., Patchett, P.J., Vervoort, J.D., and Andersson, U.B., 2005, U-Pb baddeleyite ages and Hf, Nd isotope chemistry constraining repeated mafic magmatism in the Fennoscandian Shield from 1.6 to 0.9 Ga: Contributions to Mineralogy and Petrology, v. 150, p. 174–194.

Stephens, M.B., 1998, Bedrock map 10E Karlskoga NO: Geological Survey of Sweden, Af 184, scale 1:50,000, 1 p.

Stephens, M.B., and Andersson, J., 2015, Migmatization related to mafic underplating and intra- or back-arc spreading above a subduction boundary in a 2.0–1.8 Ga accretionary orogen, Sweden: Precambrian Research, v. 264, p. 235–257.

Stephens, M.B., Ripa, M., Lundström, I., Persson, L., Bergman, T., Ahl, M., Wahlgren, C.H., Persson, P.H., and Wickström, L., 2009, Synthesis of the bedrock geology in the Bergslagen region, Fennoscandian Shield, south-central Sweden: Geological Survey of Sweden, Ba 58, 259 p.

Sundblad, K., 1994, A genetic reinterpretation of the Falun and Åmmeberg types, Bergslagen, Sweden: Mineralium Deposita, v. 29, p. 170–179.

Taylor, S.R., and Maclennan, S.M., 1985, The continental crust: Its composition and evolution—an examination of the geochemical records preserved in sedimentary rocks: Blackwell, Oxford, 312 p.

Tegengren, F.R., 1924, Sveriges ädlare malmer och bergverk: Geological Survey of Sweden, Ca 17, 406 p.

Todt, W., Cliff, R.A., Hanser, A., and Hofmann, A.W., 1993, Recalibration of NBS lead standard using a $^{202}Pb + ^{205}Pb$ double spike: Terra Abstracts, v. 5, p. 396.

Törnebohm, A.E., 1875, Geognostisk beskrifning öfver Persbergets grufvefält: Geological Survey of Sweden, C 14, 21 p.

Wagner, T., Jonsson, E., and Boyce, A.J., 2005, Metamorphic ore remobilization in the Hällefors district, Bergslagen, Sweden: Constraints from mineralogical and small-scale sulphur isotope studies: Mineralium Deposita, v. 40, p. 100–114.

Walters, S.J., 1996, An overview of Broken Hill type deposits: Centre for Excellence in Ore Deposit and Earth Sciences (CODES) Special Publication 1, p. 1–10.

Zegeye, A., Bonneville, S., Benning, L.G., Sturm, A., Fowle, D.A., Jones, C, Canfield, D.E., Ruby, C., MacLean, L.C., Nomosatryo, S., Crowe, S.A., and Poulton, S.W., 2012, Green rust formation controls nutrient availability in a ferruginous water column: Geology, v. 40, p. 599–602.
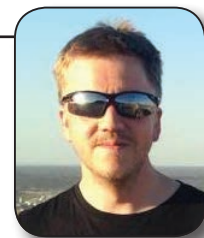
Nils Jansson received his Ph.D. degree from Luleå University of Technology (LTU), Sweden, in 2011 with a thesis entitled "The origin of iron ores and their relationship with polymetallic sulfide ores, Bergslagen, Sweden," supervised by Professor Rodney Allen. Nils was engaged in exploration for volcanogenic massive sulfide deposits in Sweden for Boliden Mineral during 2011–2014 and has been employed as a researcher at LTU since 2014. His main research interest lies in integrating structural, stratigraphic, geochemical, and mineralogical data for unraveling the genesis of complex, metamorphosed, Proterozoic iron oxide and sulfide deposits. He received the Geological Society of Sweden's Young Scientist Award in 2017.